CONTROLLED TRANSFER OF MACROSCOPICALLY ORGANIZED NANOSCOPICALLY PATTERNED SUB–10 NM FEATURES ONTO 2D CRYSTALLINE AND AMORPHOUS MATERIALS

by

Tyson Clinton Davis

A Dissertation

Submitted to the Faculty of Purdue University

In Partial Fulfillment of the Requirements for the degree of

Doctor of Philosophy

Department of Chemistry

West Lafayette, Indiana

August 2020

THE PURDUE UNIVERSITY GRADUATE SCHOOL
STATEMENT OF COMMITTEE APPROVAL

Dr. Shelley A. Claridge, Chair
Department of Chemistry &
Weldon School of Biomedical Engineering

Dr. Bryan W. Boudouris
Davidson School of Chemical Engineering &
Department of Chemistry

Dr. Christina W. Li
Department of Chemistry

Dr. Mary J. Wirth
Department of Chemistry

Approved by:
Dr. Christine Hrycyna

Dedicated to Nicole, without whom this would not have been possible.

ACKNOWLEDGMENTS

Broadly speaking, the mentoring and support of many people made my journey through graduate school successful. With apologies to anyone I fail to mention, I will acknowledge a few of those people here.

My most influential mentor is Professor Shelley Claridge. I am forever grateful to her for always being kind, thoughtful and encouraging. She taught me through her example the tenacity, bold leadership, and drive for excellence needed for success. She made me a better scientist and helped me become an independent researcher. I will always appreciate her taking me into her lab and advising me. Her husband, Dave McMillan, also deserves a large measure of thanks for his help in keeping the lab and instruments running and always being available for great conversations at Claridge group parties.

My undergraduate research advisor at the University of Utah, Professor Joel Harris, always kept in touch, was available at conferences to discuss my research, and was always willing to provide great letter of recommendation. For all this I am extremely grateful.

A special thanks to Professor Boudouris, Professor Wirth, and Professor Li for being on my committee and being available for discussions and support. Thanks also to the front office, the graduate student advisory board, Professor Hrycyna, Dr. Hoffman, and Professor Bart for their commitment to graduate students' success.

A special thanks goes to Professor Sarah Calve and Alita Miller for their help with the cell growth project.

Dr. Gilpin, Bob, and Laurie of the Purdue electron microscopy facility have my appreciation for their assistance with my research. Likewise, Dr. Pat Bishop in the Purdue Research Instrumentation Center, and everyone in the Amy Facility deserves a great deal of thanks for all the training, troubleshooting, and encouragement.

Thanks to Dr. Andy Schaber for the many hours spent getting the spectral analyzer to work for my samples.

My co-workers became a second family to me. I was able to rely on them for support and ideas. In particular, my fellow members of the trilayers, Jae Jin Bang and Tyler Hayes, were always available for lively discussion and endless laughs. When the stress was overwhelming, they helped me press forward. Conversations with Shane Russell were always entertaining and thought

provoking. Jeremiah (Jeb, Jethro, Jerome, etc.) Bechtold became a good friend with whom I could confide. Thanks also go to Anamika, Erin, and Anni for their synthetic insights. Thanks to Laura, Matt, and Juan who were always available for discussion.

My family has been one of my greatest supports. I appreciate my parents, Bill and LeeAnn, and my sister, Dallas, for their continual support and interest in my endeavors. They pushed me to take the journey into knowledge and education that they could not take themselves. I am also thankful for my in-laws, Jennie and Ross, who were always supportive and encouraging.

Along my journey, my wife, Nicole has been my greatest strength. Nicole and our sons, Ezra and Edison, filled me with drive and inspiration. I am thankful to Nicole for constantly stepping up to take care of the kids when I was out of town, letting me sleep in when I had to work late, and being genuinely interested in my research.

TABLE OF CONTENTS

LIST OF FIGURES

ABSTRACT

Surface level molecules act as an interface that mediates between the surface and the environment. In this way, interfacial molecules are responsible for conferring characteristics of relevance to many modern material science problems, such as electrical conductivity and wettability. For many applications, such as organic photovoltaics and nanoelectronics, macroscopic placement of chemical patterns at the sub-10 nm must be achieved to advance next generation device applications.

In the work presented here, we show that sub-10 nm orthogonal features can be prepared by translating the building principles of the lipid bilayer into striped phase lipids on 2D materials (*e.g.* highly ordered pyrolytic graphite (HOPG), MoS_2). Macroscopic patterning of these nanoscopic elements is achieved via Langmuir Schafer deposition of polymerizable diyne amphiphiles. On the Langmuir trough, amphiphiles at the air water interface are ordered into features that can be observed on the macroscale using Brewster angle microscopy. Upon contact of the 2D material with the air-water interface the macroscopic pattern on the trough is transferred to the 2D material creating a macroscopic pattern consisting of sub-10 nm orthogonal chemistries. We also show here how hierarchical ordering can be accomplished via noncovalent microcontact printing of amphiphiles onto 2D materials. Microcontact printing allows a greater measure of control over the placement and clustering of interfacial molecules.

The alkyl chain/surface enthalpy has a great deal of influence over the ordering of amphiphiles at the sub-nm scale. Here, we examine this influence by depositing diyne amphiphiles onto MoS_2 which has a weaker alkyl adsorption enthalpy compared to HOPG. We found that dual-chain amphiphiles deposited on MoS_2 adopt a geometry that maximized the molecule-molecule interaction compared to the geometry adopted on HOPG.

Finally, we show how the hierarchical pattern of diyne amphiphiles can be transferred off of the 2D material onto an amorphous material. This is done by reacting the amorphous material with the conjugated backbone of the diyne moiety through a hydrosilylation reaction to exfoliate the film from the 2D crystalline material. The resulting polymer ‘skin’ has many applications were controlling interfacial properties of an amorphous material is important.

CHAPTER 1. INTRODUCTION

A ubiquitous challenge in developing next-generation devices (*e.g.* devices used for energy conversion,[1] biosensing, and nanoelectronics)[2, 3] is the need for interfaces with precise control over chemical patterning at the nanometer scale while simultaneously controlling the macroscopic placement of those patterns. The cell membrane contains amphiphiles that assemble into macroscopically organized nanoscopic patterns at the sub-10 nm scale (*i.e.* hydrophobic tails with hydrophilic heads). Sub-10 nm patterning can be achieved at the surface by translating the building principles of the cell membrane into laying-down lamellae of amphiphiles on 2D materials (*e.g.* highly ordered pyrolytic graphite (HOPG), MoS_2).[4, 5] Here, we show how macroscopic patterning of the sub-10 nm orthogonal patterns can be achieved using Langmuir-Schafer conversion and noncovalent microcontact printing. We further show how the alkyl-chain/surface enthalpy can influence the assembly of the nanoscopic pattern. Finally, we show how the hierarchical patterns can be transferred from the 2D material to an amorphous material to create a sub-nm skin that can be used for several applications including the directed growth and differentiation of cells.

For many applications, surpassing current manufacturing nodes at scales substantially less than 10 nm, in conjunction with conferring long range patterning over an entire device is highly desirable.[3] Photolithography is the current industry standard for long-range nanoscopic patterning of (semi)conductors and insulators across the surface. While photolithography can routinely produce patterns in the 14 nm range, patterning in the sub-10 nm regime becomes costly and results in poor line fidelity, leading to defects and line roughness.[6, 7] Soft lithographic approaches,[8, 9] such as dip-pen nanolithography,[10] have been attractive alternatives due to their cost effectiveness. While these techniques can create high fidelity patterns at sub-micrometer scales, they have issues with scalability.

In nature, the cell membrane often patterns functionally orthogonal chemistries at the sub-10-nm scale while conferring hierarchical ordering across the membrane through thousands of different lipids that perform varying functions. By translating the patterning principles of the cell membrane into lying-down lamellar phases on 2D materials both the hydrophobic tail and hydrophilic head are exposed to the environment. Long chain alkanes and aromatic molecules (*e.g.* porphyrins, and phthalocyanines) can self-assemble into a lying-down morphology on 2D materials due to the epitaxial match between the alkyl zig-zag and the hexagonal lattice of the

highly crystalline material or through π-π interaction in the case of aromatic self-assembly.[11, 12] Noncovalent self-assembly presents a route whereby the unique electronic and physical properties of the 2D material are conserved while modifying its interfacial chemistry with technologically relevant high-resolution patterning.[11, 13]

Herein, amphiphiles used for noncovalent functionalization almost exclusively contain diacetylene functional groups. The addition of diacetylene functional groups in the alkyl tails enables photopolymerization to produce a conductive ene-yne polymer chain. This topochemical polymerization has been most extensively studied in 2D assemblies of 10,12-pentacosadiynoic acid (PCDA) for use as a molecular wire.[14-17] For purposes of hierarchical patterning, the Claridge group has shown that the polydiacetylene (PDA) also stabilizes the monolayer to subsequent solution processing used in device manufacturing by making desorption more difficult.[18] PCDA assembles into rows due to interchain van der Waals interactions and dimerization of the carboxylic acid headgroups.[14, 19, 20] This results in the PCDA lying flat on the surface giving a <0.5 nm film height and lamellar patterns with a 6 nm periodicity.

Diyne phospholipids can also be used for noncovalent patterning of surfaces. Phospholipids are the main constituents of the cell membrane and undergo hierarchical self-assembly in the lipid bilayer. Diyne phospholipids, such as 1,2-bis(10,12-tricosadiynoyl)-sn-glycero-3-phosphoethanolamine (diyne PE), exhibit distinct characteristics that provide unique advantages as templates for directing further assembly compared to fatty acids. Striped phases of phospholipids adopt a 'sitting' orientation in which the headgroup protrudes a few Ångströms from the interface allowing greater participation with the environment.[19] The protruding amine in diyne PE, for example, has a $pK_{1/2}$ on the surface as measured by contact angle titrations that is equal to its solution phase pK_a. This would be consistent with the dielectric environment around the sitting phase amine being similar to what it would experience in solution.[19] Thus, the sitting phase orientation of diyne PE allows for the amine to interact with the environment to control wetting, undergo further modification, and control other interfacial properties.[21-23]

Drop-casting has been useful for preparing noncovalent assembly of materials in studies addressing patterning in the nanometer range.[24-26] Herein is given two methods achieving hierarchical ordering from the nanometer to the millimeter scale. First, Chapter 2 discusses the ability to hierarchically pattern striped phase lipid monolayers using controlled Langmuir–Schaefer (LS) conversion from the nanometer to the millimeter scale. The Langmuir-Schaefer

technique organizes submillimeter patterns at the air-water interface, which can be observed through Brewster angle microscopy, and transfers them to the substrate upon horizontal dipping at the interface. The result is visualized using atomic force microscopy (AFM), showing striped patterns at the nanometer scale. Somewhat remarkably, we found that scanning electron microscopy (SEM) can resolve not only noncovalent lying-down domain structures at length scales up to 1 mm, comparable to those probed optically in Langmuir films, but also at scales as small as ~10 nm, typically accessed by AFM. Using SEM to bridge the scale disparities, we studied several dipping conditions to tailor the coverage and size of domains on the surface. This shows to the ability to create technologically useful microscopically organized nanostructural elements.

Second, Chapter 3 shows an advance in controlling *macroscopic* placement of nanoscopically patterned molecules on the surface. One application that would benefit from hierarchical molecular-scale and microscale interfacial clustering of striped phase amphiphiles is the controlled display of complex biomolecules for high-throughput screening of biomolecular interactions.[27] Complex biomolecules adopt controlled orientations, with both nanoscale and microscale spatial ordering in biological systems.[28, 29] Therefore, in order to mimic elements of these biological environments, it would be necessary to not only position functional groups on the surface, but also to control their orientation, clustering, and placement relative to other functional groups.

We have found that noncovalent microcontact printing of striped phases combines the microscopic geometric control over surface chemistry with molecular-scale control over ligand presentation needed to work towards controlled display of biomolecules, mimicking their biological environment. Utilizing both diyne amphiphiles (*e.g.* diynoic acids, diyne phospholipids) and a saturated phosphoinositol, we demonstrated that it is not only feasible to use microcontact printing to create microscale striped patterns of amphiphiles on HOPG, but that it can be done with control over factors such as fidelity of transfer and orientation of domains.[30]

Chapter 4 focuses on the importance on the molecule-substrate interaction in both directing assembly and promoting molecular geometries by investigating the assembly of amphiphiles on MoS_2. Transition metal dichalcogenides (TMDs) (*e.g.* MoS_2, WSe_2) have interesting electronic properties but a weaker alkyl adsorption enthalpy compared to HOPG. Here is shown that effective noncovalent functionalization and patterning can be achieved using two-chain diyne phospholipids such as diyne PE. Instead of the sitting phase geometry adopted on HOPG, diyne PE adopts an

edge-on orientation which promotes stability by increasing molecule–molecule interactions and allowing twice as many molecules to be adsorbed to the substrate. This finding provides a design principle for stabilizing noncovalent monolayers on weakly epitaxial substrates.

Through Langmuir-Schaefer conversion and noncovalent microcontact printing, we have established diverse methods of patterning amphiphiles from the molecular to the microscopic scale on substrates with ordered lattices such as HOPG and MoS_2.[30-32] These patterns have enabled modulation of surface wetting and allowed for the assembly of inorganic wires and controlled display of molecules.[19, 22, 30, 33] While patterning and controlling surface chemistry on conducting and semiconducting substrates has been widely studied by our group and others, an analogous method for controlling surface chemistry and wettability on amorphous substrates would represent a considerable advance. Achieving microscopic arrays of sub-10 nm orthogonal patterns on an amorphous substrate would allow for not only controlled wettability and surface chemistry similar to results obtained on HOPG but would also allow for more diverse applications such as colorimetric sensors and wearable electronics.

PDMS is an elastomeric material widely used in biological and medical microchips, microelectromechanical systems (MEMS), and microfluidic devices due to its ease of fabrication, biocompatibility, low cost, and optical transparency.[8, 34] PDMS has also been used as an insulating layer and as a substrate for colorimetric sensors.[35] A current challenge in utilizing PDMS for flexible electronics is the lack of an easy way to direct patterning on the surface due to the amorphous nature of the material. The achievement of sub-10 nm orthogonal patterns on PDMS via a molecular (<0.5 nm thick) film, analogous to the sub-10 nm patterning accomplished on HOPG, would function as a 'skin' on PDMS. As with striped phases of molecules on HOPG, the molecular skin on PDMS would provide and interface for subsequent templating and control of surface wetting.

In Chapter 5, we have demonstrated that it is possible to transfer the nanoscopically ordered patterns of polymerizable amphiphiles from highly oriented crystalline substrates (*e.g.* HOPG, MoS_2) with PDMS using a hydrosilylation reaction. When PDMS is cured, the methylhydrosiloxane moiety in the cure reacts with the vinyl groups in the base in a hydrosilylation reactio to create an interconnected polymer network.[36] When the mixture of the base and cure is poured onto a HOPG surface containing a polymerized amphiphile, the alkyne undergoes a hydrosilylation with the methylhydrosiloxane in the cure to convert regions of the ene-yne polymer

backbone to an ene-ene polymer. The ene-ene backbone maintains electron delocalization along the polymer allowing the polymerized amphiphiles to undergo radiative decay through fluorescence, enabling spectroscopic characterization.

CHAPTER 2. HIERARCHICALLY PATTERNED NONCOVANLENT FUNCTIONALIZATION OF 2D MATERIALS BY CONTROLLED LANGMUIR-SCHAEFER CONVERSION

A version of this chapter has been published in *Langmuir*
DOI: 10.1021/acs.langmuir.7b03845

2.1 Introduction

As 2D materials (e.g., graphene, MoS2) are integrated more widely into hybrid materials and devices, rigorous control over both global and local surface chemistry becomes increasingly important.[11, 13] Microscopic and nanoscopic patterning methods have been developed for monolayer chemistries including alkanethiols on the coinage metals, and have found remarkably broad use.[8, 37-39] However, patterning monolayers on 2D materials raises additional challenges because such materials are often functionalized noncovalently (e.g., with lying-down phases of functional alkanes or polycyclic aromatic compounds).[13, 40-42] While this strategy avoids disrupting extended electronic conjugation within the 2D layer, it also reduces monolayer stability, with potential impacts to both pattern fidelity and characterization.[21, 43] Thus, patterning and characterization strategies that are effective for covalent monolayers are not necessarily equally useful for noncovalently functionalized 2D materials, suggesting utility to the development of methods relevant to such interfaces.

Lying-down phases of diynoic acids such as 10,12-pentacosadiynoic acid (PCDA, Figure 2.1a) have been extensively investigated in the context of noncovalent functionalization of 2D materials.[14-16, 24, 38, 44] When drop-cast from organic solvents such as CHCl3 or assembled at a liquid–solid interface from low-vapor-pressure solvents such as octadecene, these molecules form lying-down lamellar striped phases (Figure 2.1c–e). In the lamellae, the zigzag carbon skeleton of each alkyl chain aligns along the ⟨1120⟩ direction of the hexagonal highly oriented pyrolytic graphite (HOPG) lattice (Figure 2.1c), and pairs of headgroups form hydrogen-bonded carboxylic acid dimers that further stabilize the lamellar structure. The paired headgroup structure results in a lamellar width ∼6 nm (approximately twice the chain length), comprising predominantly exposed alkyl chains with rows of polar headgroups ∼1 nm wide.

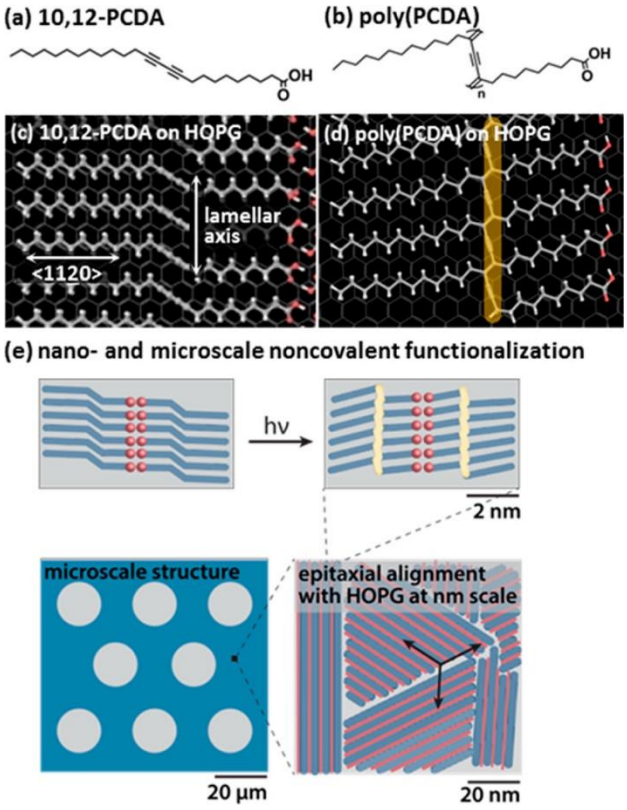

Figure 2.1. Structures of 10,12-PCDA (a) before and (b) after photopolymerization. Molecular models of (c) pre- and (d) postpolymerization lying-down phases epitaxially assembled on HOPG. (e) Schematic of targeted hierarchical nano- and microscale noncovalent functionalization of 2D material.

The lamellar monolayer architecture also aligns the internal diynes for topochemical photopolymerization (Figure 2.1b,d) when the surface is exposed to UV irradiation.[44, 45] The conjugated ene–yne polymer backbone formed by irradiation can be utilized as a molecular wire,[44] suggesting the possibility of nanoscopic circuit design. Polymerization also stabilizes the monolayer toward removal of the deposition solvent and/or addition of other solvents.[19, 46] A growing literature has begun to elucidate the consequences of the 1 nm wide stripes of functional headgroups and the noncovalently adsorbed ligand architecture (both PCDA and other polymerized diynes) in controlling interfacial wettability and other properties relevant to device design utilizing noncovalently functionalized 2D materials.[18, 19, 22, 46-48]

As this type of self-assembly has become more widely utilized to control the surface chemistry of 2D materials, governing not only nanoscopic but also microscopic ordering becomes desirable. Assembly from solution at the solid–liquid interface can create stable nanoscopic

domain structures and molecular-scale patterns,[11, 41, 47] although microscale patterning is less straightforward.

In contrast, Langmuir–Schaefer (LS) transfer[49] provides significant potential advantages for patterning noncovalent 2D interface chemistry at the microscale by modulating local molecular adsorption across the substrate. A rich literature on molecular assembly, phase transitions, and phase segregation in Langmuir films has shown that it is possible to assemble diverse molecular patterns in monolayers on an aqueous subphase.[50-55] These molecular patterns can be transferred to solid supports through either vertical dipping (Langmuir–Blodgett, LB, transfer)[56, 57] or horizontal dipping (LS transfer).[49, 58]

Although both methods are classically used to transfer standing phases, a few reports have indicated that the LS approach can be used to create noncovalent lying-down monolayers of molecules such as PCDA on HOPG by deliberately converting the standing phase on the aqueous subphase into a well-ordered lying-down striped phase on the 2D material.[14, 59, 60] Previous reports of LS conversion of this type have been aimed at understanding molecular scale ordering and the formation of ene–yne molecular wires[15, 16, 61, 62] relevant to nanoscopic circuit design.[42, 44] Thus, they have used scanning tunneling microscopy (STM) and atomic force microscopy (AFM) to examine transferred molecular domains on scales typically <1 μm. More recently, we have found that it is possible to assemble much larger domains (>10 μm) through LS conversion at elevated temperatures (50–70 °C) and that long-range order confers additional stability during vigorous solvent washing,[18] relevant to solution processing for some device preparation protocols.[18, 19, 22, 46, 48]

Broadly, we aim to develop a foundation for using LS conversion to create spatially controlled microscopic patterns exhibiting the characteristic nanoscopic ordering (i.e., striped molecular rows) that has led to sustained long-term interest in noncovalent functionalization with diynes. Several questions arise: What structural factors in Langmuir films promote molecular transfer to the 2D material? Can transfer be prevented in specified areas of the film, analogous to resists used in other forms of patterning? What factors increase or decrease local ordering as transferred molecules assemble into domains on the 2D material?

Mechanistically, LS conversion of standing phases to form lying-down phases represents a fundamental departure from classical LS transfer of standing phases. In the classical LS transfer, domains of tightly packed molecules are lifted from the subphase in their original orientations.

Conversely, in LS conversion of standing phases to form lying-down phases, each molecule must not only desorb from the aqueous subphase but also reorient substantially to lie horizontal on the substrate (Figure 2.2). Thus, experimental parameters (e.g., temperature, mean molecular area, pH or ionic strength of subphase)[63-65] that produce high transfer ratios[66, 67] for LS transfer of standing phases are not necessarily optimal for LS conversion to form lying-down phases.

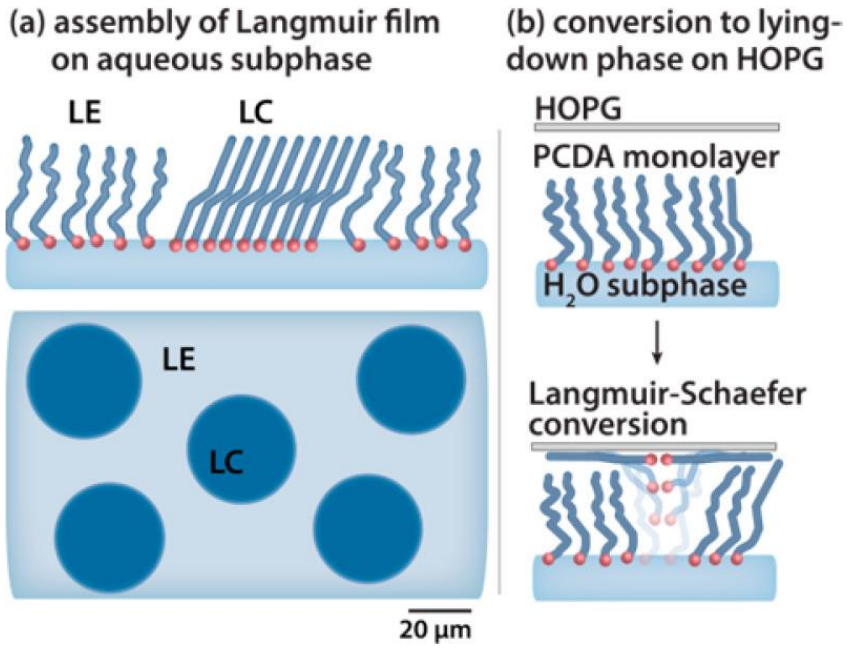

Figure 2.2. (a) Schematic showing molecular assembly of Langmuir film on aqueous subphase with microscale patterns in ordering. (b) Schematic of conversion of molecules from the standing phase Langmuir film into a lying-down phase on HOPG.

Here, we examine the relationship between molecular transfer and expanded or condensed phase regions on the aqueous subphase, by controlling temperature, mean molecular area, substrate dipping rate, and contact time. On the basis of the required reorientation during transfer, we reasoned that LS conversion was likely to be more efficient from expanded phases than from condensed phases in the source Langmuir film; this would be consistent with relatively low surface pressures indicated for previous transfers (e.g., <10 mN/m for conversion to lying-down phases on HOPG[15, 16] vs 20–30 mN/m for standing phase LS transfer to substrates such as mica).[68, 69] However, forming a complete lying-down monolayer requires only a small fraction of the molecules available in a standing phases Langmuir film. Because of this difference from standing phase transfer, we examined a broad range of transfer conditions.

2.2 Results and Discussion

2.2.1 SEM characterization of domain structure and ordering in lying-down monolayers on HOPG

A significant challenge in developing practical control over LS conversion relates to characterization of the transferred film. Lamellar features (~6 nm periodicity) within ordered domains (typically 100–1000 nm) are straightforward to visualize by AFM, and higher-resolution imaging of lamellar substructure can be performed by STM.[44] However, Langmuir films frequently exhibit domain structures on much longer scales (up to 1 mm).[51, 52] Thus, in relating post-transfer domain structures to Langmuir film ordering (Figure 2.3), it would be useful to visualize transferred monolayer structures across the entire range of scales relevant to ordering. Despite the local flatness of HOPG, monolayer structure (film thickness <0.5 nm) becomes difficult to visualize by AFM at larger scales (>10 μm), as contributions from HOPG step edges (0.34 nm/step) and other features begin to dominate image contrast.

Somewhat remarkably, we find that scanning electron microscopy (SEM) can resolve not only noncovalent lying-down domain structures at length scales up to 1 mm comparable to those probed optically in Langmuir films (Figure 2.4a), but also at scales as small as ~10 nm, typically accessed by AFM (Figure 2.4b). SEM has been used previously to image standing phase domains (typical thicknesses ≥2 nm) of alkanethiols on gold[70-72] and phospholipids[73] on SiO2; however, contrast is typically dominated by ordered standing phases. Here, we resolve not only domain morphologies but also molecular row orientation in much thinner (<0.5 nm) lying-down organic monolayers on HOPG.

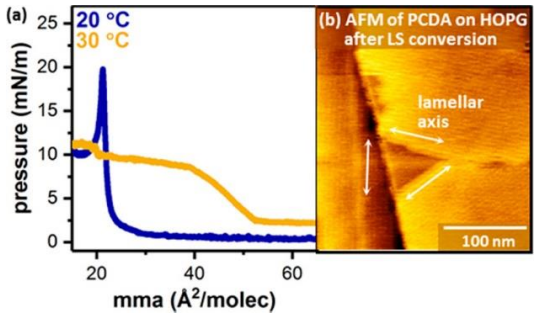

Figure 2.3. (a) Pressure–area isotherms for Langmuir films of PCDA on pure water at 20 °C (blue) and 30 °C (orange). (b) AFM image of typical nanoscopic ordering observed when lamellar phases are assembled on HOPG through LS transfer. White arrows highlight lamellar alignment in epitaxy with HOPG; the feature running from top left to bottom center is a step edge in the HOPG substrate.

2.2.2 Comparison of transfer from liquid expanded and condensed phases in langmuir films

Here, we compare transfer across a range of mean molecular areas from 100 to 20 $Å^2$/molecule, at temperatures of 20 °C (at which there is a collapse point in the isotherm) and at 30 °C (at which the collapse point disappears and there is a rise in surface pressure at much larger mean molecular areas). Figure 2.3a illustrates differences in the isotherms collected at 20 and 30 °C. When molecules are transferred from Langmuir films at both temperatures and a range of mean molecular areas, using LS transfer protocols, nanoscopic regions of molecular ordering are observed by AFM, similar to the image shown in Figure 2.3b. In such areas, lamellar axes align in epitaxy with the hexagonal graphite lattice as shown by the white arrows; the linear feature running from top left to center bottom is a step edge in the HOPG substrate.

At microscopic scales, we find correlations between areas of high and low extents of molecular transfer and factors such as local degree of condensation in the Langmuir film. Transfer under conditions corresponding to the LE–LC coexistence segment of the isotherm at 30 °C (Figure 2.3a, yellow trace) enables us to compare molecular transfer from expanded and condensed domains (Figure 2.4). Arrays of circular features with diameters of ∼30–50 μm are visible in the transferred film (Figure 2.4a); interpreted in line with previous fluorescence studies of Langmuir films of long-chain amphiphiles in the LE–LC coexistence,[50, 74] circular features would represent condensed phase domains and the surrounding areas expanded phase. Here, higher-resolution SEM imaging at the boundary of one of the circles (Figure 2.4b) reveals that the dark circular areas are predominantly vacant, with small areas of lacy, amorphous film structure and occasional lamellar domains. In contrast, regions transferred from the LE phase (areas around the circles) contain tightly packed, well-ordered lamellar domains. Greater transfer from the expanded phase than from the condensed phase would be consistent with stronger chain–chain interactions in the condensed phase stabilizing the source monolayer and reducing transfer.

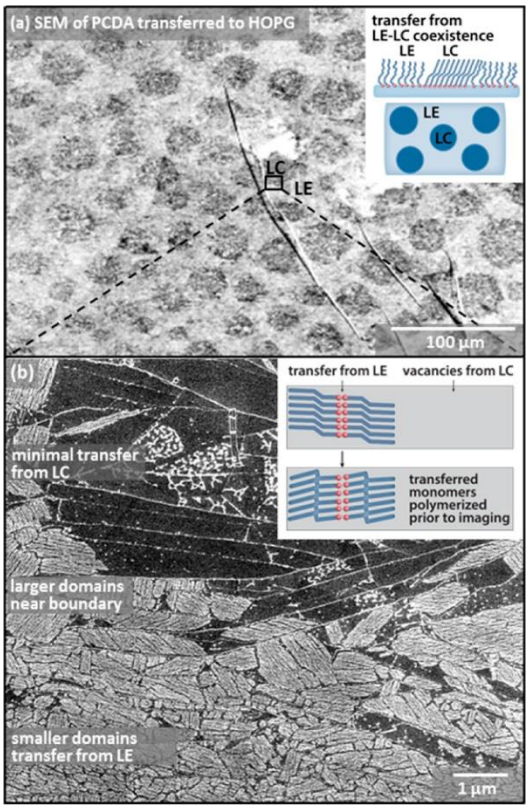

Figure 2.4. SEM images of PCDA film transferred at 30 °C, 30 Å^2/molecule and photopolymerized after transfer but prior to SEM imaging. Scale bars represent (a) 100 µm and (b) 1 µm. Image in (b) is acquired from the highlighted region in (a).

In Figure 2.4b, there is a noticeable increase in the average domain size adjacent to the LC vacancy (middle), in comparison with the smaller domains transferred further into the LE phase (bottom). Previous work in submonolayer island nucleation and growth[75] as indicated that the number density of domains, N, varies with both molecular adsorption rate (F) and the rate of molecular diffusion across the substrate (D) with

$$N \propto \left(\frac{F}{4D}\right)^{1/3}$$

If the difference in domain size is interpreted in this light, a 4-fold difference in number density could suggest as much as a 64-fold difference in molecular transfer rate from the bulk LE phase in comparison with the LE–LC boundary, if diffusion rates in the two regions after transfer are similar. We do not observe this distinction in all cases at LE–LC boundaries. However, we frequently observe microscale transitions in average domain size, pointing to the capability to create local

differences in transfer rate, and thus domain structure, based on local differences in molecular stability on the subphase at the time of transfer.

Because previous studies on Langmuir–Blodgett transfer of standing phase films have indicated that molecule–substrate interactions can be used to modulate assembled film structures,[57, 76-78] we also examined this possibility. Frequently in such studies, the relatively strong interactions between a polar or ionic headgroup and an ionic surface such as mica can restructure molecular lattices in comparison with molecular ordering on the aqueous subphase.[78, 79] In the case of the films described here, the π–alkyl interactions that stabilize the lying-down phase are responsible for the most central type of restructuring (creating the striped phase), but we also wondered whether the macroscopic interaction between the descending HOPG and the molecular film on the substrate could be used to modulate local molecular condensation in the Langmuir film. Experimentally, we tested dipping rates from 1 to 300 mm/min (Figure 2.5), measuring at least three areas on at least three different substrates per dipping speed, and find circle diameters of 140 ± 40 μm at 1 mm/min (Figure 2.5a), 40 ± 10 μm at 10 mm/min (Figure 2.5b), and 6.4 ± 2.6 μm at 50 mm/min (Figure 2.5c). Average circle diameters (μm) decrease exponentially with the logarithm of the dipping speed (mm/min) as

$$diameter\ (\mu m) = 144e^{-\log(dip\ speed)/0.89} - 6.8$$

with R^2 = 0.92. Together, these results suggest the capability to pattern transfer using a combination of assembly on the aqueous subphase and factors that controllably modulate assembly during transfer.

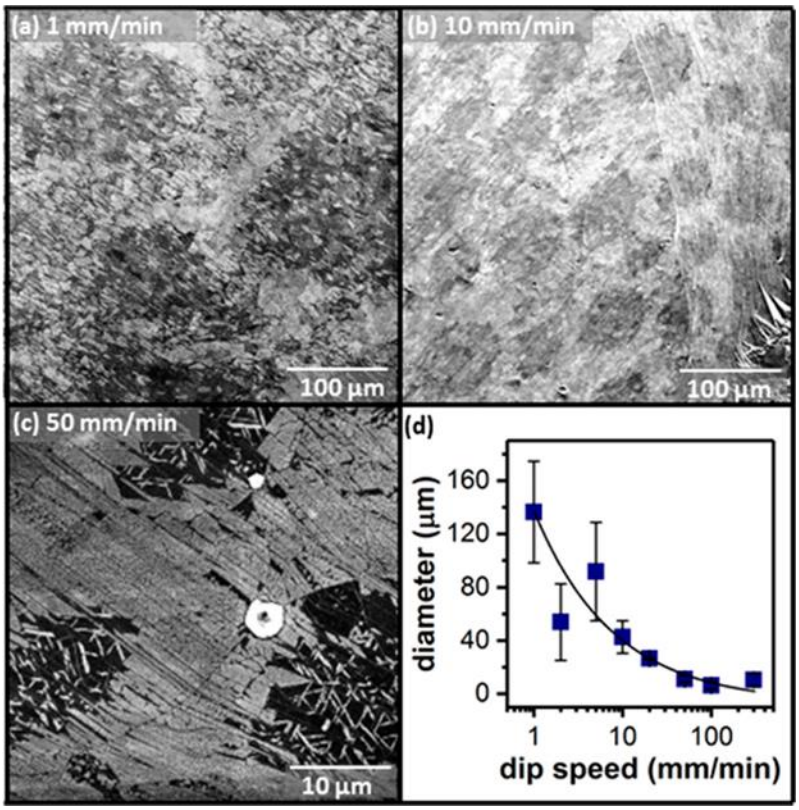

Figure 2.5. SEM images of PCDA film transferred with the substrate lowered onto subphase at (a) 1, (b) 10, and (c) 50 mm/min. (d) Average circle diameters vs dipping speed.

2.2.3 Polymerization-induced cracking reveals lamellar directionality

A key element of the capability to achieve high-resolution SEM images of these sub-nanometer thick lying-down monolayers relates to the topochemical polymerization process and thus illuminates the propensity for polymerization of each domain. Previous literature on the topochemical polymerization of diacetylenes indicates that polymerization requires a high degree of order in the diynes.[80-82] As mentioned above, the polymerization process can be used either to generate molecular wires in the monolayer[44] or to stabilize it for further processing[47] and thus is a useful property to probe in the context of noncovalent 2D material functionalization.

In SEM images acquired at the smallest scales probed (500 nm scale bar, Figure 2.6b) cracking defects are observed within ordered domains, revealing the directionality of the lamellar assemblies. These features are not typically evident in PCDA monolayers imaged by AFM (Figure 2.6a), although we have observed similar features in AFM images of large domains of diynoic phospholipids,[18] which have lower surface mobility than PCDA. Such features appear to arise from

slight narrowing of ordered lying-down lamellae as the diyne rehybridizes to form the ene–yne during polymerization (Figure 2.6c); such conformational changes are known to occur during polymerization of diynoic acids in the solid state.[83, 84] For the experiments here, we have polymerized the PCDA films for 1 h under an 8 W UV lamp, similar to previous descriptions of such processes in the literature;[17, 42] the appearance of additional cracking defects under the SEM electron beam would be consistent with additional polymerization events, plausible given the propensity of such molecules to polymerize under both beams of tunneling electrons in an STM[14, 42] and X-ray irradiation.[85]

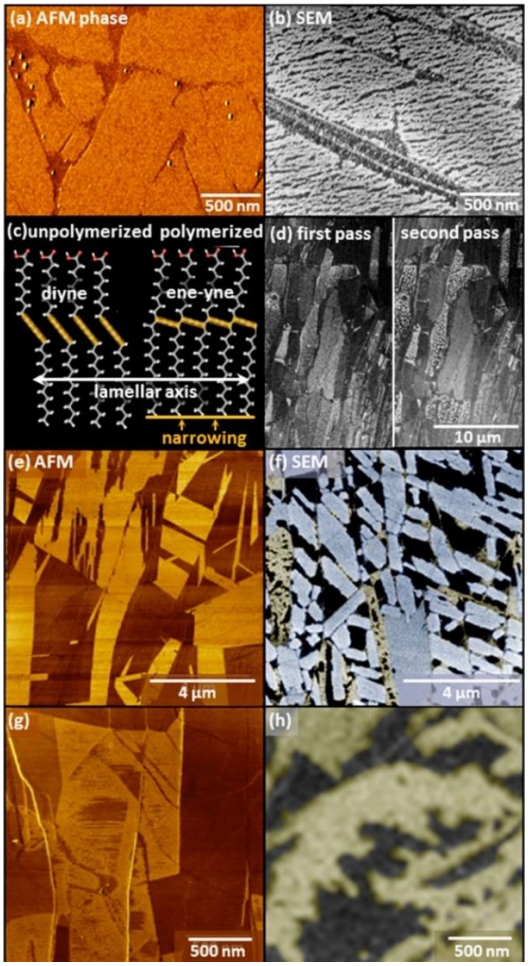

Figure 2.6. (a) AFM and (b) SEM images showing domain structure of PCDA transferred to HOPG and then photopolymerized; cracking defects visible in SEM image. (c) Minimized molecular models showing polymerization-induced lamellar narrowing that leads to cracking in (b). (d) Images illustrating beam-induced formation of dendritic phases in nonpolymerizable domains. (e, f) AFM and SEM images of large-scale domain morphology. (g, h) Comparison of AFM and SEM images of disordered amorphous domains.

Some domains (particularly in films transferred from Langmuir films with large mean molecular areas) do not evolve cracking defects and instead re-form into amorphous (globular, dendritic, or porous) structures during imaging. In Figure 2.6d, repeated imaging of the same area reveals that some domains have re-formed into globular structures, while others have developed cracking defects similar to Figure 2.6b. Overall, our experience suggests that ordered domains have similar gross morphologies in AFM (Figure 2.6e) and SEM (Figure 2.6f), while dendritic or other amorphous structures in SEM images (Figure 2.6h, and light regions in Figure 2.6f) are correlated with areas of the substrate that appear streaky in AFM images (Figure 2.6g). Presumably these areas lack the high degree of molecular ordering required for topochemical polymerization. We note that in some molecular systems examined previously by others (e.g., standing phases of long-chain phosphonic acids on mica),[86] diffusion of molecules along the substrate following transfer can lead to dendritic domains structures similar to Figure 2.6h directly.

When we have performed SEM imaging of non-diyne fatty acids that have been transferred under conditions similar to those that lead to the circular vacancies shown in Figure 2.4, we observe qualitatively similar features in SEM images (see Appendix A); areas of the film that appear to be monolayer exhibit nonlinear defects but do not rapidly evolve into dendritic domains of the type shown in Figure 2.6h. Although further experiments would be necessary to fully establish the behavior of nonpolymerizable films, this suggests that they can be transferred and characterized using techniques similar to those described here.

2.2.4 Correlation of large-scale features in langmuir films undergoing collapse and transferred film structures on HOPG

Although LC regions in the source monolayer undergo limited transfer in the LE–LC plateau, tighter molecular packing at or near the Langmuir film collapse point can result in the transfer of many small domains (suggesting rapid transfer) and/or standing phase or multilayer regions. Figure 2.7 compares a Brewster angle microscopy (BAM) image of a Langmuir film at 20 °C and 20 $Å^2$/molecule (Figure 2.7a) with SEM images of a film on HOPG transferred under the same conditions (Figure 2.7b, c). In Figure 2.7a, the monolayer has undergone collapse, forming multilayer structures that appear as bright features in the BAM image, due to the large differences in local refractive index they create at the interface. Large-scale SEM images of films transferred under these conditions (Figure 2.7b) reveal bright features similar in terms of geometry

and size to islands observed in the BAM image. High-resolution SEM images acquired at the periphery of one of the bright areas (Figure 2.7c) reveal bright rodlike features with characteristic lengths 100–1000 nm and widths 50–500 nm, which, based on increased topographic protrusions in AFM images (see Appendix A), appear to be multilayers and standing phase transferred from the collapsed source film. The surrounding surface is occupied by lower contrast lying-down domains. When transfer is carried out at elevated surface pressures just prior to the collapse point (i.e., at conditions similar to those that would typically be used to transfer standing phases to other types of substrates), regions of both standing phase and lying-down phases are transferred (see Appendix A). These findings point to the utility of transfer from less densely packed films when the aim is to establish lying-down phase domains rather than standing phases on the HOPG substrate.

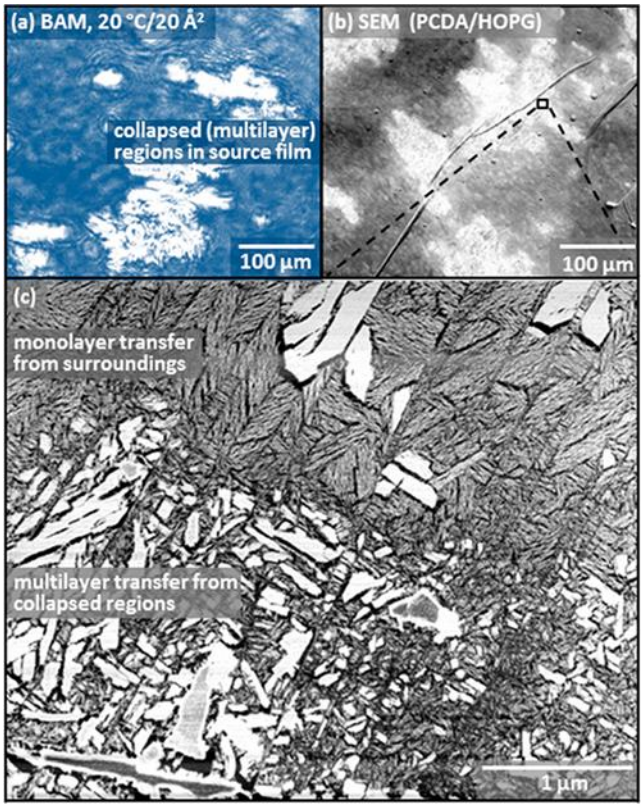

Figure 2.7. (a) BAM image of a Langmuir film of PCDA at 20 °C and 20 $Å^2$/molecule. (b, c) SEM images of PCDA films transferred to HOPG under the conditions illustrated in (a) and then photopolymerized. (c) A high-resolution SEM image of the small area of (b) highlighted with a black box.

2.2.5 Nanoscopic features in transferred films

For many applications (e.g., electronics), it is important not only to control surface chemistry at nanoscopic or microscopic scales but also to create microscopically organized nanostructural elements. Nanoscopic domain structures are not readily imaged using the optical techniques commonly used to illuminate ordering in Langmuir films. However, Langmuir–Blodgett transfer of standing phase lipid rafts with diameters <100 nm onto mica has been demonstrated previously,[87, 88] suggesting the feasibility of LS conversion onto materials such as HOPG.

Figure 2.8a illustrates a PCDA film transferred onto HOPG under conditions that produced large-scale Langmuir film structures visible in the BAM image in Figure 2.8b. In the AFM image, hierarchically ordered nanoscopic molecular domains with dimensions 500 nm or less and interdomain spacings of 1–2 μm are arranged at approximately right angles (axes highlighted with white arrows in Figure 2.8a, example domains highlighted with boxes near center), congruent with the larger dendritic features visible in the BAM images (Figure 2.8b). Overall, these microscopically linked nanoscopic structural elements suggest a first step toward more arbitrary molecular pattern transfer, using molecular assembly and phase segregation within Langmuir films, which may be further modulated by the substrate during transfer as shown in Figure 2.5.

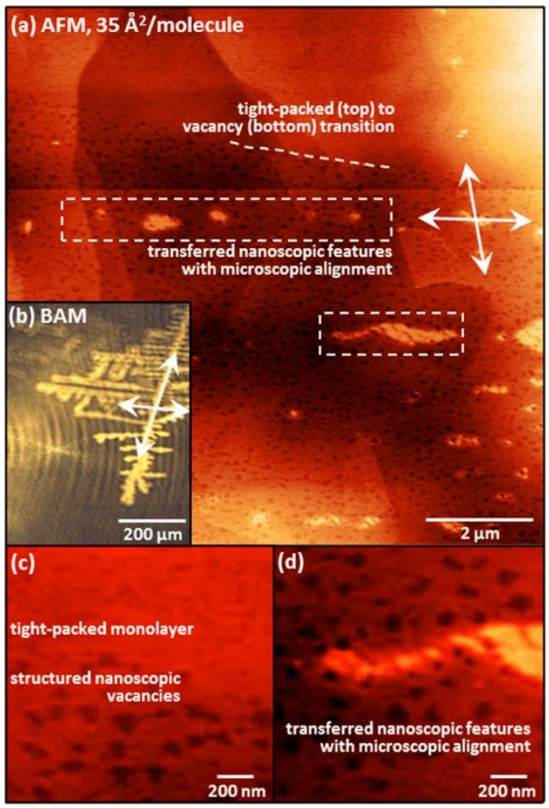

Figure 2.8. (a) AFM images of PCDA transferred to HOPG at 30 °C, 35 $Å^2$/molecule and then photopolymerized. Crossed arrow pattern indicates axes of crosshatched pattern of nanoscale domains. White boxes highlight transition from full to monolayer coverage to nanoscopic vacancies (upper left), a representative transferred nanoscopic molecular area (lower right). (b) BAM image of PCDA on aqueous subphase acquired at 35 and 30 $Å^2$/molecule, showing larger-scale dendritic pattern. (c) Enlargement of tight-packed/nanoscopic-vacancy boundary. (d) Enlargement of lower transferred nanoscopic feature highlighted in (a).

Near the top of the image (highlighted by dashed line), the background monolayer structure transitions from complete coverage (top) to a structure with many small (50–100 nm) rounded vacancies. This transition is not correlated with obvious substrate topographical features or the hexagonal symmetry of the HOPG lattice, suggesting the likelihood that the nanoscopic vacancies also arise due to a change in source film packing in the areas above and below the line.

2.2.6 Identification of transfer parameters leading to high degrees of ordered domain coverage and/or large domain sizes

Next, we examined criteria for transferring high surface coverage monolayers with large ordered domains. Transfer of standing phases utilizes relatively high dipping surface pressures (ca. 30 mN/m for saturated fatty acids)[68, 69, 89] to ensure in-place transfer of a tightly packed, well-ordered film with few defects.[67] In contrast, lying-down phases have typically been transferred at lower pressures[14, 16, 59] consistent with the need for molecules to reorient during transfer. Because of the need for reorientation, temperature also represents a potentially useful parameter for controlling transfer.

Here, we examined the impacts of both mean molecular area and temperature on transfer. Figure 2.9 compares representative SEM images of molecular transfer at 20 and 30 °C from source films with mean molecular areas of 20–40 $Å^2$/molecule. In general, we observe greater transfer efficiency at 30 °C, resulting in large homogeneously functionalized areas of the substrate (Figure 2.9b–d, right).

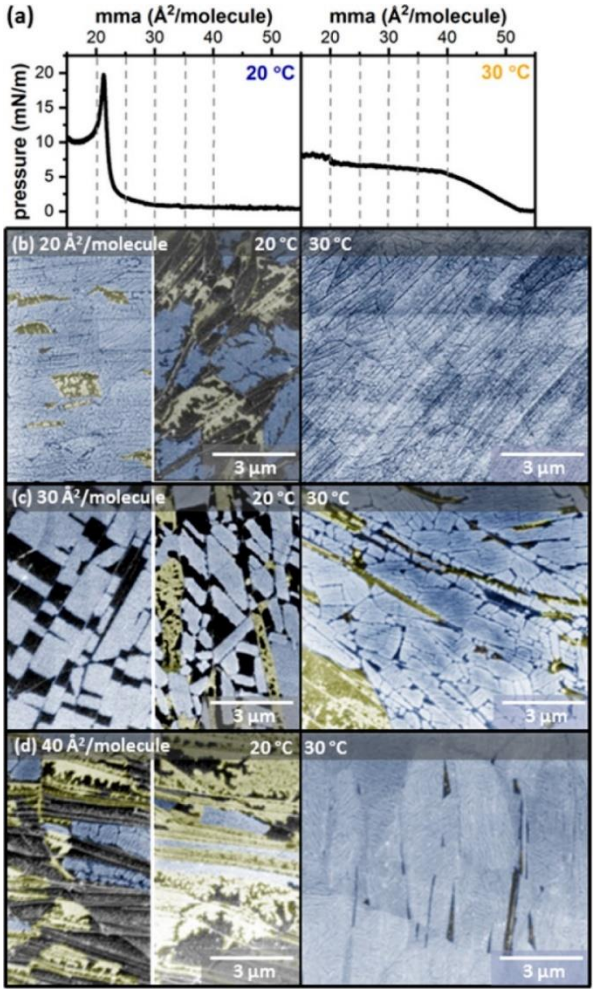

Figure 2.9. (a) Pressure–area isotherms for PCDA transferred from subphases at temperatures of 20 °C (left) and 30 °C (right). (b–d) SEM images of typical PCDA films transferred to HOPG at 20 °C (left) and 30 °C (right), at mean molecular areas of (b) 20, (c) 30, and (d) 40 Å^2/molecule. Films were photopolymerized after transfer but prior to SEM imaging.

Figure 2.10 quantifies molecular transfer to HOPG from Langmuir films with mean molecular areas from 20–100 Å^2/molecule. The transfer ratio—the ratio of molecules transferred vs those present in the Langmuir film—is commonly used to assess the efficiency LS transfer. Here, we quantify transfer ratios by measuring the HOPG fractional surface coverage of lamellar, amorphous, and standing or multilayer phases of PCDA in SEM images of transferred films and estimating molecular footprints for each type of coverage (see Experimental Methods and Appendix A for more detail).

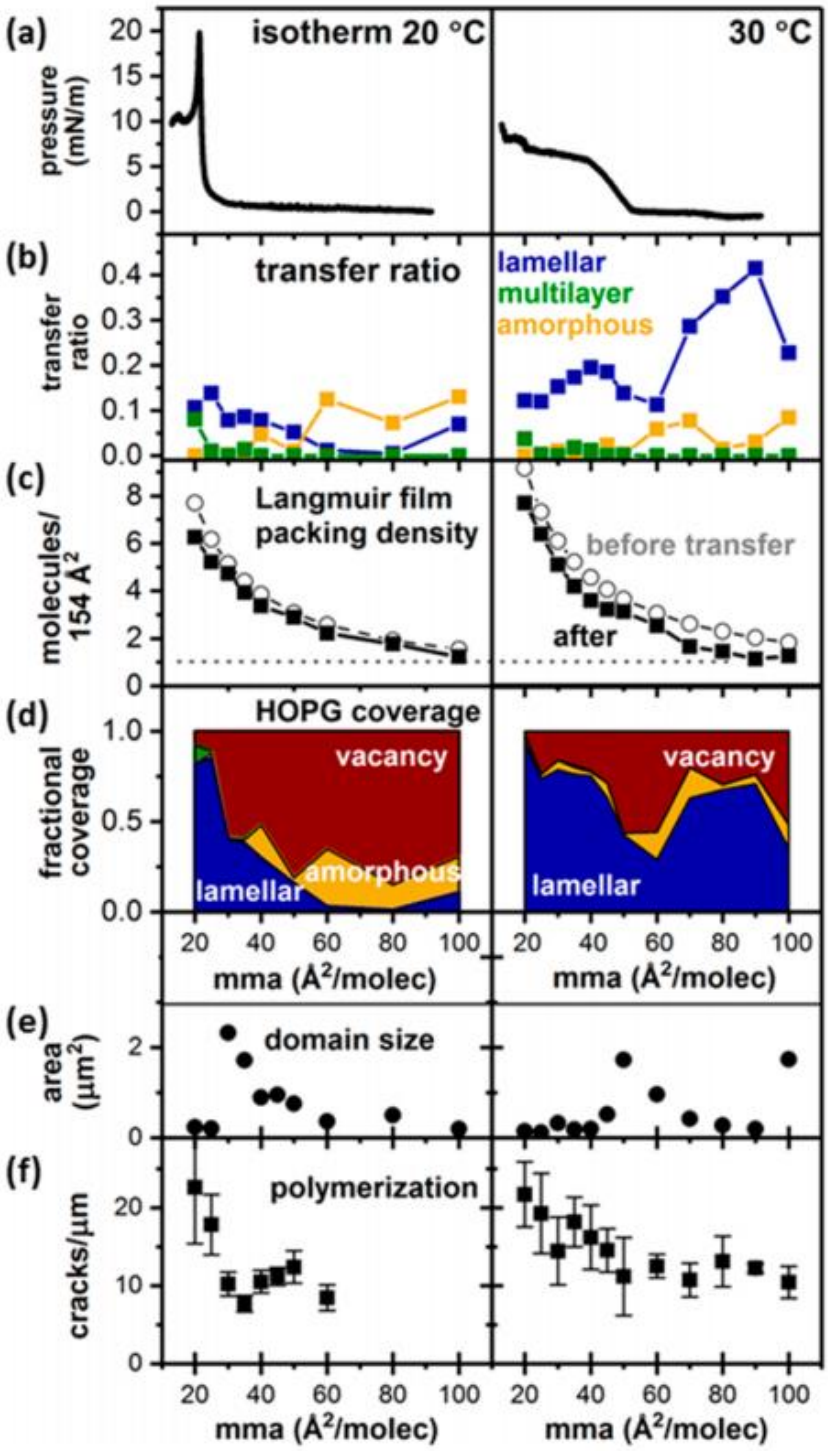

Figure 2.10. Analysis of film transfer at points along isotherms at 20 and 30 °C. (a) Isotherms, (b) transfer ratios, and (c) Langmuir film packing densities (expressed relative to ideal lying-down phase packing densities). (d) HOPG coverage after transfer, expressed as fractional coverage of lamellar (blue), amorphous (gold), and standing or multilayer (green) domain structure, with amount of vacant surface shown in red. (e) Average domain sizes for monolayers on HOPG and (f) polymerization-induced crack densities for monolayers on HOPG, expressed in cracks/μm.

At both 20 and 30 °C, transfer ratios are fairly low (Figure 2.10b), with values >0.2 observed only for expanded films (>60 $Å^2$/molecule) at 30 °C. Such behavior is not necessarily surprising or undesirable, for two reasons. Only the first lying-down layer of PCDA molecules on HOPG experiences the relatively strong π–alkyl interactions that occur between PCDA alkyl chains and the HOPG basal plane. Thus, there is substantially less energetic driving force for the formation of second (or subsequent) molecular layers during transfer.

Additionally, forming a lying-down monolayer requires very few molecules (1 PCDA/154 $Å^2$) in comparison with a standing phase (here, molecular densities as great as 1 PCDA/20 $Å^2$). Figure 2.10c illustrates the ratio of molecules available in the source film to those required for a lying-down monolayer (gray traces). At mma = 20 $Å^2$/molecule in the Langmuir film, there are ~7.7 as many PCDA molecules available as would be required to form a lying-down layer. Even at 100 $Å^2$/molecule, there are 1.54 times as many molecules as required.

We quantify molecules remaining on the subphase after transfer (Figure 2.10c, black lines) by subtracting the total molecular transfer in Figure 2.10d (both structured and amorphous) from the initial average packing density (Figure 2.10c, gray lines). For all transfers tested, approximately 1 full lying-down monolayer of molecules remains on the aqueous subphase (dotted line on graph), which is reasonable given the high surface tension of water.

Because the goal of this type of transfer is typically to create an ordered molecular layer on HOPG, we next illustrate the fractional surface coverage of ordered, disordered, and standing or multilayer regions on the HOPG (Figure 2.10d). Blue regions in the graphs in Figure 2.10d represent ordered lamellar surface coverage, which is typically the type desired. Ordered coverage decreases rapidly for transfers at 20 °C (left) but remains high for subphase temperatures of 30 °C (right) across much of the range of mean molecular areas tested.

Mean lamellar domain sizes vary with mma at transfer (Figure 2.10e), with maxima at 30 $Å^2$/molecule at 20 °C and 50 $Å^2$/molecule at 30 °C. However, as illustrated in earlier figures, local mean domain sizes can vary substantially across the substrate in areas that contacted condensed or expanded phases in the Langmuir film, meaning that large domains may still be observed under transfer conditions with low mean values.

The ability to polymerize PCDA monolayers is often a significant consideration in promoting stability or achieving desired electronic properties. Thus, we also examined the density of polymerization-induced cracking in SEM images of large lamellar domains as a metric of

ordering. Cracking decreases from ~20 cracks/μm for densely packed films to ~10 cracks/μm for transfers at larger mma values (Figure 2.10f), suggesting a somewhat lower degree of molecular ordering in such films.

Temperature control can also be leveraged *after* transfer to modulate molecular ordering. Transfer at slightly elevated temperatures (30 °C) produces higher coverage but can also result in smaller domain sizes due to more rapid transfer. Domain sizes in high-coverage transferred films can be further increased by thermal annealing; Figure 2.11 shows the impacts of post-transfer heating for 1 h at 50 °C. For larger amphiphiles that are less amenable to post-transfer thermal annealing, we have also found that it is possible to perform *in situ* annealing during transfer to rapidly increase domain sizes.[18] Together, these two strategies provide a means to create large homogeneous domains with high coverage, for applications that benefit from low defect densities.

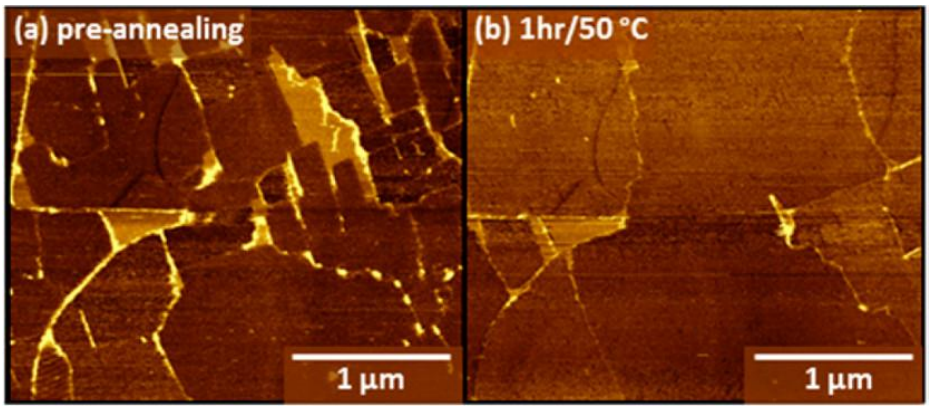

Figure 2.11. AFM images of PCDA film transferred at 20 °C and 35 $Å^2$/molecule: (a) as-transferred film structure and (b) same area of film after annealing for 1 h at 50 °C.

2.3 Conclusions

Using LS conversion, we achieve hierarchical noncovalent patterning on 2D materials, controlling surface functionality on length scales from mm to <10 nm. Molecular ordering in the Langmuir film influences long-range structure (e.g., circular microscale vacancies or right-angle arrays of nanoscopic domains), while epitaxial assembly on the hexagonal HOPG lattice during LS conversion creates linear functional patterns with sub-10 nm pitch. SEM imaging illuminates not only details of lamellar orientation down to the few-nanometer scale but also differences between domains that are capable of polymerization and those that are not; this capability enables

us to probe properties of the interface relevant to structured functionalization and stability at sub-10 nm scales. Polymerizable molecular domains can be assembled with both very high coverage and control over domain size, by controlling subphase temperature, source film packing density, and dipping rate, or by applying post-transfer thermal annealing. Taken together, these capabilities suggest a route for assembling molecular patterns on an aqueous subphase and converting them into striped lying down phases to modulate interactions between a 2D material and its environment. While levying additional requirements in regards to sample preparation, in relationship to other methods for molecular self-assembly on 2D materials, LS conversion provides an additional level of control for applications in which microscale modulation of assembled structure across the entire substrate is desirable.

2.4 Experimental Methods

2.4.1 Materials

10,12-Pentacosadiynoic acid (PCDA, ≥97.0% purity) was purchased from Sigma-Aldrich (St. Louis, MO) and used as received. Chloroform (ChromAR grade) was purchased from Macron Fine Chemicals (Center Valley, PA) and used as received. Self-assembled monolayers of diynoic acids were deposited on 1 cm × 1 cm highly oriented pyrolytic graphite (HOPG, SPI Supplies, West Chester, PA) substrates, which were freshly cleaved immediately prior to sample deposition. All initial steps in the deposition process were carried out under UV-filtered light to prevent polymerization in solution. PELCO conductive liquid silver paint, standard SEM pin stub mounts, and double-coated carbon conductive tape were purchased from Ted Pella, Inc. (Redding, CA).

2.4.2 Langmuir–Schaefer Conversion

LS conversion was performed using a KSV-NIMA Langmuir–Blodgett trough (Biolin Scientific, Stockholm, Sweden). For the deposition of PCDA, 12 μL of a 0.75 mg/mL solution of PCDA in chloroform was deposited on a subphase of deionized water (~18 MΩ cm). After the small amount of chloroform used for amphiphile transfer was allowed to evaporate (typical equilibration time 15 min), trough barriers were slowly moved inward (3 mm/min barrier motion, corresponding to a 0.05 cm^2/s reduction in the 98 cm^2 trough area) to increase film uniformity across the trough surface. All steps in the assembly and transfer were carried out under UV-filtered

light to prevent polymerization on the trough. Similar considerations have typically precluded GIXD studies of unpolymerized Langmuir films of diynoic acid monolayers,[85] since the films polymerize under the X-ray beam.

At the target average molecular area (e.g., 25 $Å^2$/molecule), the HOPG substrate was slowly (2 mm/min, unless otherwise stated in the paper) lowered onto the subphase with the cleaved surface facing down, nearly parallel to the liquid interface, using an automated dipper that suspends the sample on a hanging wire, in order to maximize stability of the HOPG–subphase contact. After 4 min in contact with the liquid interface, the HOPG was gently lifted out of contact with the liquid using the automated dipper. We note that it is also possible to perform transfer for a shorter period of time; see Appendix A for similar transfer results after 30 s in contact with the subphase.

Diacetylene-functionalized amphiphile monolayers prepared using the described procedure were photopolymerized prior to imaging in order to improve monolayer stability. Photopolymerization was performed by 60 min of irradiation under a 254 nm 8 W UV lamp with approximately 4 cm between the lamp and the sample surface.

2.4.3 Brewster Angle Microscopy (BAM)

The laser assembly of the custom-built Brewster angle microscope utilized here incorporates a 635 nm diode laser with variable power (4.5 mW maximum) as a light source. The beam passes through a spot focusing lens aligned along its elliptical axis with a Glan-Taylor polarizer (1000:1 extinction ratio) which passes p-polarized light. The laser assembly is fixed to a tip turn mount for fine X–Y translation of the spot into the optical imaging area; the assembly also incorporates a variable angle fine adjustment to optimize the incident angle of the beam. The entire laser arm is rigidly mounted to the optical imaging arm using a narrow metal beam, minimizing the footprint of the microscope above the trough. The optical imaging arm consists of a long-working-distance objective with a nominal 10× magnification and an infinity-correcting element that produces a collimated exiting beam. The collimated beam then passes through an extension tube and a linear film polarizer in a rotational mount. Additional extension tubes and/or lenses may be placed in the beam path to increase the magnification. Image data are collected using a Point Gray Grasshopper 3 CMOS camera with 2448 × 2048 pixel resolution.

2.4.4 SEM Imaging

All SEM images were obtained on a FEI NOVA NanoSEM field emission SEM. Microscopy was performed at 5 keV accelerating energy at an ~3 mm working distance, with an aperture of 30 μm for a current of ~56 pA. The substrates were mounted onto a standard 12.7 mm × 8 mm SEM pin stub mount with carbon tape. The substrate was then painted on three edges with silver paint to increase conductivity from the face of the HOPG to the mount. All images acquired with a magnification <8500× utilized an Everhart–Thornley detector, and those with a magnification ≥8500× utilized a through-the-lens detector (TLD) with an immersion lens.

2.4.5 AFM Imaging

All AFM measurements were performed under ambient conditions in air using a Bruker (Bruker Instruments, Billerica, MA) MultiMode AFM equipped with an E scanner or Asylum Cypher ES in tapping mode with Mikromasch (Sofia, Bulgaria) HQ:NSC18/AL BS tips (nominal force constant 2.8 N/m and radius of curvature <10 nm). The cantilever oscillation phase shift was carefully monitored to ensure the tip was engaged in the attractive mode to improve imaging of lamellar structures within domains. The set point ratio was typically maintained between 0.4 and 0.7 and was rarely decreased below 0.4 to avoid tip sweeping effects.

2.4.6 Image Analysis

Images were processed using Gwyddion scanning probe microscopy data visualization and analysis software[90] and ImageJ analysis software[91] to perform median line corrections, plane flattening, scar artifact removal, and contrast adjustment. For large images (e.g., 60 μm × 70 μm SEM images), local variations in contrast across the image area were often large enough to complicate automated segmentation and were not feasible to remove using polynomial background correction; in these cases, local brightness and contrast correction were applied in Photoshop using guided region selection with automatic edge selection to flatten the background.

2.4.7 Energy Minimization

Software packages Maestro and Macromodel (Schrödinger, Cambridge, MA) were used respectively to visualize molecular structures and to perform force field minimizations.

Models were minimized using the OPLS_2005 force field, with normal cutoffs for van der Waals, electrostatic, and hydrogen-bonding interactions. Minimizations were performed using the Polak–Ribiere conjugate gradient (PRCG) algorithm and gradient method with 50 000 runs and a convergence threshold of 0.05.

CHAPTER 3. HIERARCHICALLY PATTERNED STRIPED PHASES OF POLYMERIZED LIPIDS: TOWARD CONTROLLED CARBOHYDRATE PRESENTATION AT INTERFACES

A version of this chapter has been published in *Faraday Discussions*
DOI: 10.1039/C9FD00022D

3.1 Introduction

Interfaces with precisely constructed chemical environments at the micrometer and nanometer scales are required for applications ranging from the design of electronic devices to the controlled display of complex biomolecules.[27] Increasingly, the goals of controlling interfacial structure may include not only positioning functional groups on the surface, but also controlling their orientation, clustering, or placement relative to other functional groups, mimicking complex structures such as those in cell membranes.

Monolayers of molecules such as alkanethiols have been broadly utilized to structure interfacial chemistry, particularly on coinage metals.[37] In alkanethiol monolayers, ordered lattices of alkyl chains position terminal functional groups with nearest-neighbor distances ~0.5 nm, tilted at angles influenced by the bond between the thiol and the substrate.[37] Lattices displaying simple functional groups (*e.g.* carboxylic acids) influence further assembly at the interface (*e.g.* selecting for specific crystal facets of calcite); microcontact printing enables geometrically patterned assembly over microscopic (or large nanoscopic) areas.[92-94]

Controlling presentation of more complex, biologically relevant functionalities raises new challenges. In biological environments, polysaccharides, peptides, and other entities are presented in controlled orientations, with both nanoscale and microscale spatial ordering. To mimic elements of these environments for applications such as high-throughput screening of biomolecular interactions,[28, 29] it would be useful to present microstructured areas of surface containing nanostructured clusters of specific ligand chemistries, enabling multivalent binding similar to molecular recognition events in the glycocalyx.[95-103]

However, even monosaccharides occupy interfacial footprints substantially greater than that of an alkyl chain in an alkanethiol monolayer (~0.25 nm^2). Thus, creating simple lattices of these larger moieties becomes less straightforward. Designing complex clusters of functional groups at

biologically relevant scales—with linear dimensions large relative to alkyl chain nearest neighbor distances in standing phases (>0.5 nm) but small relative to those typically achieved through microcontact printing (significantly <100 nm)—becomes especially challenging.

One complementary strategy for clustering structures with larger footprints arises from a transformation to the monolayer structure.[27] Since at least the 1960s, it has been known that long-chain alkanes can adopt lying down orientations on graphite and other layered materials such as MoS_2 and WS_2.[104, 105] More recently, the surface chemistry of 2D materials (particularly graphite and graphene) has been regulated using striped phases of functional alkanes,[14, 15, 40, 104-106] in which the alkyl chains extend horizontally across the substrate. Scanning probe microscopy studies[14, 15, 40, 104-106] have shown that this arrangement produces nm-wide stripes of headgroups with 0.5 or 1 nm lateral periodicity along the row (for single-chain and dual-chain amphiphiles, respectively), separated by wider (~5 nm, dependent on chain length) stripes of exposed alkyl chains. Assembly of functional alkanes containing an internal diyne allows the monolayer to be photopolymerized, creating a conjugated ene–yne polymer backbone that has been studied extensively in the context of molecular electronics.[14, 15, 44] Polymerization also stabilizes the noncovalently adsorbed monolayer, increasing potential utility of patterns of functional groups displayed at the interface.[18, 19, 46]

Just as clustering of functional groups at biological active sites creates unique chemical environments to promote specific interactions, precise positioning of functional groups in striped phases also creates unique chemical environments (Figure. 3.1). We have observed that striped phases of diyne phospholipids[19] exhibit distinct characteristics in comparison with striped phases composed of other amphiphiles.[48] Phospholipids can adopt a 'sitting' orientation in which the terminal amine in the headgroup protrudes a few Ångströms from the interface.[19] The phosphate and ester functional groups create a tailored chemical environment around the amine. Both head and chain structures influence nano- and micro-scale assembly of striped phases,[18, 32, 107] and chain elements including the position of the polymer backbone can be used to modulate solvent availability of the polar headgroups.[48] Flexible 1D zwitterionic arrays formed by the striped phase also impact further assembly of inorganic and organic nanostructures at the interface.[22, 23] More broadly, the striped phospholipid polymer architecture represents a potential means for flexible yet controlled presentation of ligands at the interface.

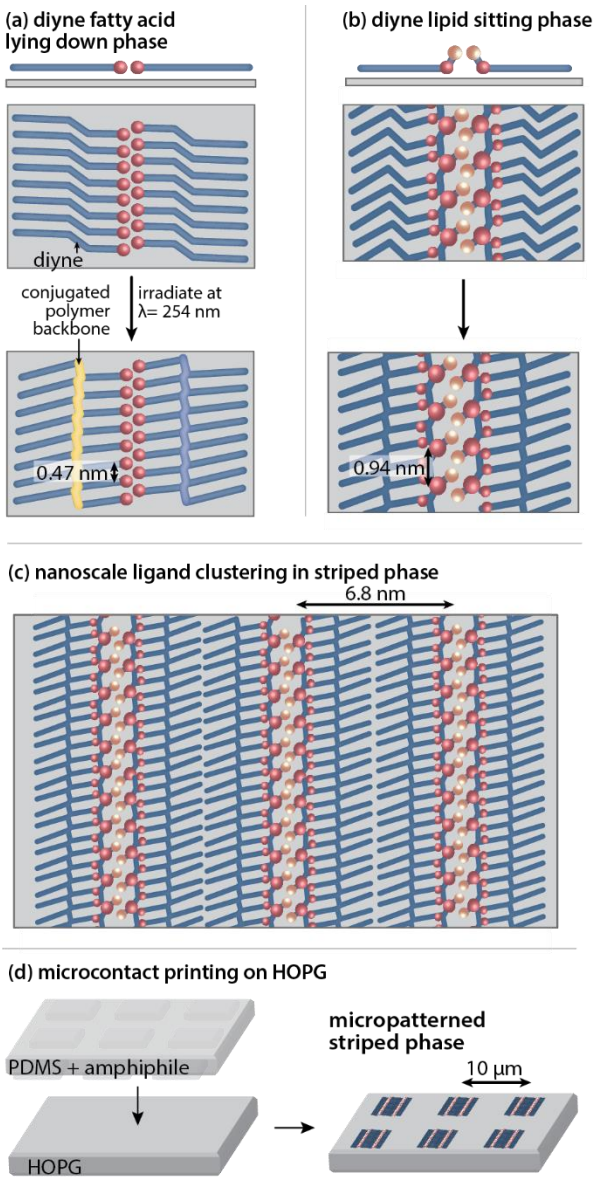

Figure 3.1. Illustrations of: (a) striped phase of diynoic acids on HOPG, showing a 0.47 nm distance between functional groups along the stripe direction; (b) striped phase of diyne phospholipids, showing a 0.94 nm distance between functional groups along the row; (c) multiple rows of the striped phase, showing lamellar periodicity, a route to nanoscale ordering of complex functional groups; and (d) illustration of poly(dimethylsiloxane) (PDMS) transfer of amphiphiles to HOPG to form striped phases.

Microcontact printing of striped phases (Figure 3.1d) has the potential to combine microscopic geometric control over surface chemistry with molecular-scale control over ligand presentation, a capability of potential use in glycobiology. However, the strong focus on molecular-scale structure in noncovalent striped-phase monolayers on highly oriented pyrolytic

graphite (HOPG) has meant that such monolayers are typically ordered and characterized at length scales < 100 nm.[108-110] Recently, we have shown that some amphiphiles order into striped phases with edge lengths > 10 μm,[18] scales relevant to controlling interactions with biological entities, and that monolayer ordering can be characterized by scanning electron microscopy (SEM), making it possible to characterize surface functionalization up to mm scales.[32, 107, 111] Some noncovalent monolayers can also be robust enough to survive vigorous solution processing and other environmental interactions.[18, 22]

Here, we demonstrate microcontact printing of striped phases of amphiphiles on HOPG, utilizing both diyne amphiphiles (*e.g.* diynoic acids, diyne phospholipids) and a saturated phosphoinositol. This approach generates hierarchical molecular-scale and microscale interfacial clustering of functional ligands, including carbohydrates, prototyping a strategy of potential relevance for controlled presentation of carbohydrates at interfaces.

3.2 Results and Discussion

3.2.1 Preparation of striped monolayers on HOPG

Striped monolayers of both single-chain amphiphiles (*e.g.* 10,12-pentacosadiynoic acid (PCDA), Figure 3.2a and b) and dual-chain amphiphiles (*e.g.* 1,2-bis(10,12-tricosadiynoyl)-*sn*-*glycero*-3-phosphocholine (diyne PC), Figure 3.2a and c) are typically prepared *via* drop-casting or Langmuir–Schaefer (LS) conversion,[14, 17-19, 22, 59] then polymerized *via* UV irradiation and characterized by atomic force microscopy (AFM) (Figure 3.2d and e). In AFM images, striped lamellar patterns are oriented at 120° angles, in epitaxy with the HOPG lattice; each stripe represents a row of lying-down molecules. SEM images of striped phases (Figure 3.2f–i) typically exhibit brighter areas representing the molecular domains, against a darker background of HOPG. Long linear features along the image diagonals in Figure 3.2f and g represent step edges in the HOPG substrates. Higher-resolution SEM images (Figure 3.2h and i) reveal linear defects within the ordered molecular domains, highlighting the directionality of the molecular rows.[32] Use of this combination of techniques enables us to characterize both microscopic and nanoscopic ordering in striped phases, including those with carbohydrate headgroups (*vide infra*).

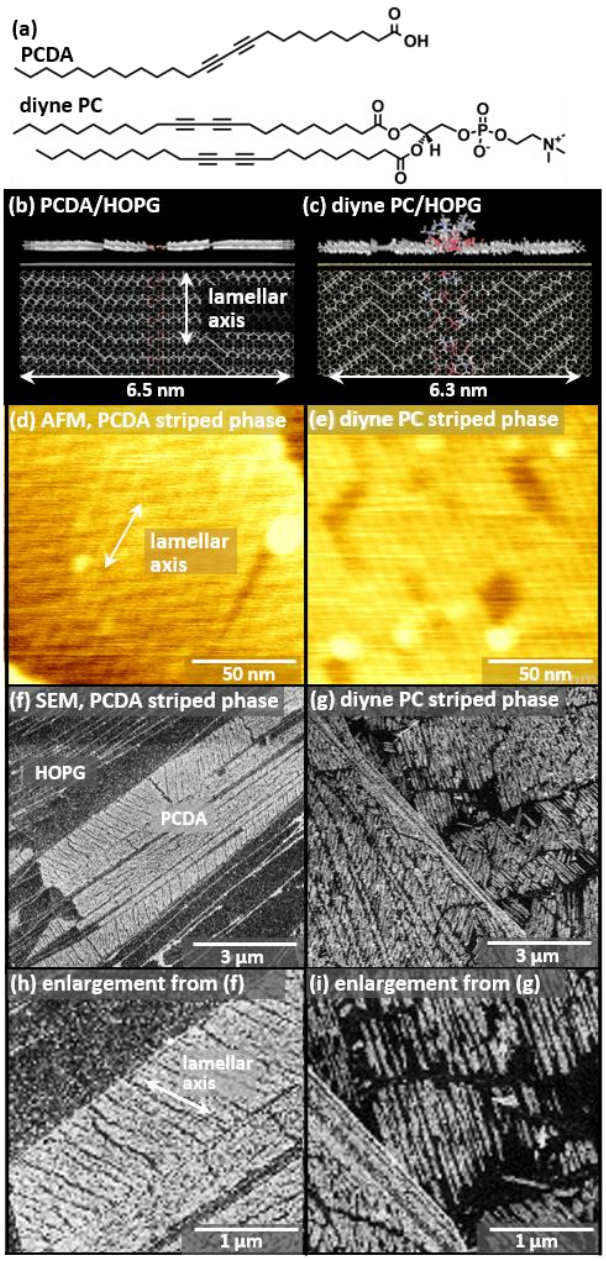

Figure 3.2. (a) Structures of PCDA and diyne PC. (b, c) Molecular models of striped phases of (b) PCDA and (c) diyne PC on HOPG. (d, e) AFM images of striped phases of (d) PCDA and (e) diyne PC, illustrating the lamellar pattern. (f–i) SEM images of striped phases of (f, h) PCDA and (g, i) diyne PC, illustrating long-range ordering.

3.2.2 Preparation of patterned striped monolayers on HOPG by microcontact printing

Microscopic patterns of striped phase monolayers were prepared on HOPG by microcontact printing,[8] as shown in Figure 3.3. Stamps used for microcontact printing of alkanethiols on gold are commonly prepared with a 10 : 1 ratio of elastomer base to crosslinker,

resulting in a nominal elastic modulus of ~2.6 ± 0.02 MPa at commonly used curing conditions (65 °C, 1 h).[112] For transfer to HOPG, which has relatively low local surface roughness, we often found that stamps prepared with a 10 : 2 ratio of base to crosslinker (nominal elastic modulus 3.6 ± 0.1 MPa)[112] improved transfer fidelity, while still enabling conformal contact.

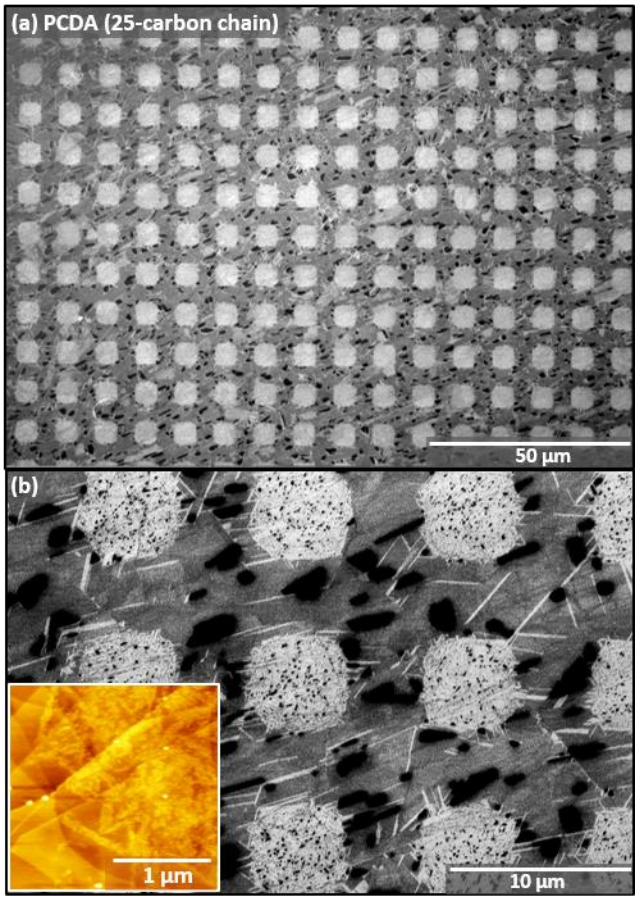

Figure 3.3. (a) SEM image of microscopic areas of PCDA striped phases assembled on HOPG by microcontact printing. (b) Higher-resolution SEM image illustrating coverage in the square interior and the small fractional coverage of molecular domains assembled outside the stamp contact area. An AFM image (inset in (b)) shows the striped phase structure.

A number of studies have previously examined factors relating to ink delivery to the substrate, with the goals of limiting diffusion of the ink outside the stamp contact area,[113-115] and limiting delivery of impurities from the PDMS stamp.[114, 116] Delivering a controlled amount of diyne amphiphile to the substrate is especially important in assembling noncovalent monolayers; screening several possible methods for controlling diyne amphiphile delivery, we found that

immersing the stamp in a solution of amphiphile in carrier solvent (1.1 mM for PCDA and single-chain amphiphiles, 0.55 mM for diyne PC and dual chain amphiphiles, maintaining the concentration of alkyl chains) generally maximized coverage of striped phase inside the contact area while minimizing coverage outside the contact area.

Ink concentrations used here are similar to those typically utilized for assembly of standing phases of alkanethiols on Au (1–10 mM),[37] although fewer molecules are required to fill a given area of the surface: the molecular footprint of an alkyl chain in a lying-down phase (1.5 nm^2 for PCDA) is much larger than for a standing phase (~0.25 nm^2). Figure 3.3a and b show SEM images of a pattern of squares transferred to HOPG using the stamp preparation and inking conditions described above. Figure 3.3b shows a higher-resolution image of the square pattern. High coverage is observed within the squares; AFM is used to verify that molecular coverage is comprised of striped domains (Figure 3.3b, inset, and Appendix B). Areas between the square stamp contact areas (channel regions) contain low number-densities of long, narrow molecular domains characteristic of submonolayer island nucleation and growth under conditions of low surface monomer concentrations.[75] Areas between squares also contain material that appears in dark contrast in SEM images. Similar features appear on substrates brought into contact with stamps wetted with the carrier solvents in the absence of amphiphile (see Appendix B). Deposition of impurities is also common in microcontact printing of alkanethiols on gold. Previous studies suggest that the deposited material is the oligomeric PDMS crosslinker, in which hydrosilyl groups undergo oxidation to form more polar species exhibiting increased solubility in the ink or carrier solvent.[116, 117]

3.2.3 Transfer characteristics of single-chain amphiphiles based on chain length

In using a striped phase to pattern functionality at an interface, shorter chain lengths correspond to smaller stripe pitch values, and thus shorter distances between linear clusters of functional groups on the surface (Figure 3.4a). However, chain length also impacts dynamics in the self-assembly process. In previous demonstrations of microcontact printing to form standing phases (*e.g.* alkanethiols on Au), others have observed that molecular diffusion around the stamp contact area increases for molecular inks with shorter chains.[38, 71, 118] Here, we tested the transfer and assembly of 10,12-diynoic acids with chain lengths from 21 to 29 carbons to form noncovalently adsorbed striped phases to better understand the range of pitches that can reasonably

be established, and the fidelity of patterning (Figure 3.4b–d). In the Figure, areas exhibiting linear defects typical of striped phases (similar to those in Figure 3.2h) have been colored yellow as a guide to the eye. Image segmentation was used to estimate the average distance over which each amphiphile spread outside the stamped area in areas with good stamp contact (Figure 3.4d, see Appendix B for example AFM images used for segmentation). The average band through which molecules diffuse decreases in width from ~600 nm for HCDA to ~50 nm for NCDA. For all four carboxylic acids, the number density of domains was 10–20 per μm^2 within the contact area, which is reasonable given that the monomer concentration in the ink solution was the same for each molecule.

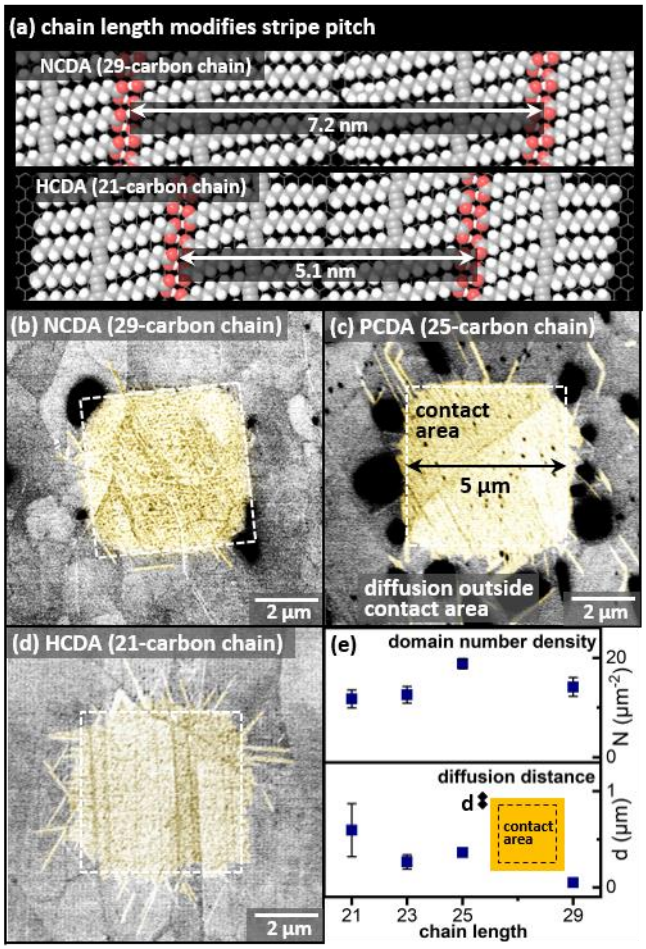

Figure 3.4. (a) Molecular models of diynoic acid striped phases with the longest (29 carbon) and shortest (21 carbon) chains utilized in these experiments. (b–d) SEM images of 10,12-diynoic acids: (b) nonacosadiynoic acid (NCDA, 29-carbon chain), (c) pentacosadiynoic acid (PCDA, 25-carbon chain), (d) henicosadiynoic acid (HCDA, 21-carbon chain). (e) Average domain number density per µm^2, *N*, and average distance molecular layer extends outside stamped area, *d*, for chain lengths from 21–29 carbons.

3.2.4 Transfer of dual-chain amphiphiles

Commercially available diyne phospholipids have two alkyl chains and a zwitterionic headgroup, which would be expected to modulate molecular transfer and spreading on the substrate in comparison with the single-chain carboxylic acids transferred above. Here, we test the transfer behavior of two diyne phospholipids, 23:2 diyne phosphocholine (diyne PC, Figure 3.5) and 23:2 diyne phosphoethanolamine (diyne PE, Figure 3.6). The phospholipid structures are

identical with the exception that the bulky terminal quaternary ammonium in the PC headgroup (Figure 3.5a) limits molecular packing in comparison with PE, which has a smaller terminal primary amine.

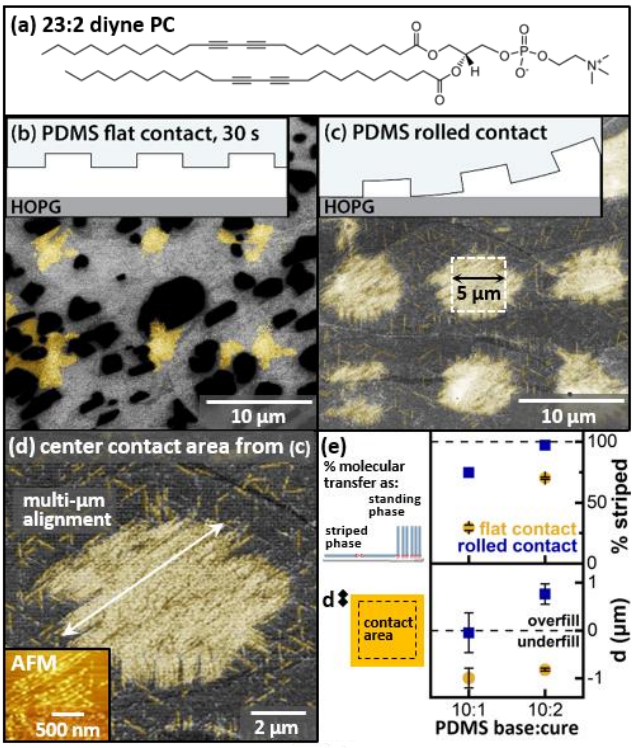

Figure 3.5. (a) Structure of diyne PC. (b–d) SEM images of 0.5 mM diyne PC in EtOH transferred to HOPG using (b) 30 s flat contact and (c, d) rolled contact (stamp prepared at 10 : 2 base : crosslinker ratio). (e) Comparison of % striped phase (*vs.* standing phase) molecular transfer with flat and rolled stamp contact, and fill of contact area, for PDMS stamps prepared with 10 : 1 and 10 : 2 base : crosslinker ratios.

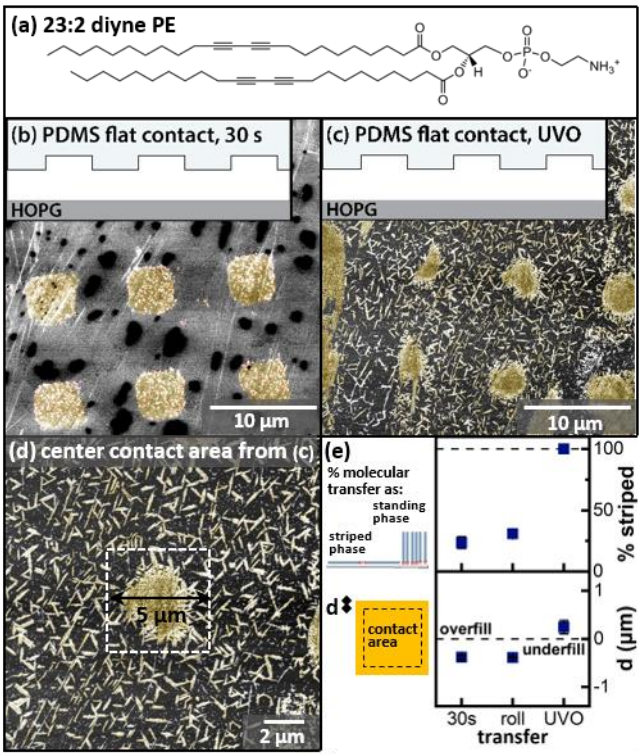

Figure 3.6. (a) Structure of diyne PE. (b–d) SEM images of 0.5 mM diyne PE in EtOH transferred to HOPG using (b) 30 s flat contact and (c, d) flat contact with stamp hydrophilicity increased with UV ozone (stamp prepared at 10 : 2 base : crosslinker ratio). (e) Comparison of % striped phase (*vs.* standing phase) molecular transfer with flat contact, rolled contact, and flat contact with UV ozone, and fill of contact area, for PDMS stamps prepared with 10 : 2 base : crosslinker ratios.

Transfer conditions similar to those optimized for single-chain amphiphiles result in a large fraction of standing phase formation (bright areas in square centers) (Figure 3.5b, highlighted in yellow as a guide to the eye; also see Appendix B). This is reasonable given the large number of alkyl carbons per molecule, promoting interchain interactions leading to standing phase formation. To mechanically destabilize interchain interactions (*e.g.* standing phases) on the stamp, and to initiate domain growth from a limited area (to increase post-transfer molecular alignment), we tested molecular delivery by rolling the stamp along the HOPG surface (Figure 3.5c and d, see Appendix B for more experimental detail regarding the rolling procedure). Testing transfer from stamps prepared with both 10 : 1 and 10 : 2 PDMS elastomer base : crosslinker ratios, we found that rolled contact increased the percentage of molecular transfer that produced striped phases (to near 100% for 10 : 2 stamps with rolled contact, Figure 3.5e). Flat contact typically resulted in underfilling of the stamp contact area, while rolled contact resulted in average coverage zones

extending nearly 1 μm outside the stamp contact area (as visible in Figure 3.5d). In some cases (again, see Figure 3.5d), rolled contact produced molecular alignment across the stamp contact areas (*i.e.*, lamellar axes aligned from upper left to lower right in Figure 3.5d). Using other contact geometries, we have not observed this behavior, so with further optimization, rolled contact may represent a means of achieving long-range molecular alignment in printed striped phases, for applications in which such alignment is desirable.

Diyne PE (Figure 3.6a) has a smaller terminal amine group that enables stronger lateral interactions between headgroups in standing phases, in comparison with the PC headgroup (which is bulky enough to limit packing). Importantly, the primary amine can also act as a functional handle for further coupling reactions, of potential utility in elaborating headgroups for glycobiological applications. Microcontact transfers of diyne PE in the conventional flat contact geometry also produced large areas of molecules assembled in standing phases (Figure 3.6b). For transfer of diyne PE, the highest percentages of striped phase were observed for transfers in which the stamp surface hydrophilicity was increased by treatment with UV ozone plasma (a process which has been used previously to transfer hydrophilic molecules to create standing phase self-assembled monolayers (SAMs)). While multiple factors may contribute to the observed improvement in striped phase assembly during transfer, one possibility is that the hydrophilic stamp enables PE to assemble with polar headgroups oriented toward the stamp surface, with tails oriented favorably to mediate the initial stages of adsorption to HOPG for striped phase assembly. The differences in transfer behavior observed for molecules as structurally similar as diyne PE and diyne PC suggests a need to carefully balance molecule–stamp, molecule–molecule, and molecule–substrate interaction strengths for transfer of complex amphiphiles such as those relevant to glycobiology.

3.2.5 Striped phases from carbohydrate-conjugated lipids

The procedures developed above are also useful for microcontact printing of phospholipids incorporating carbohydrates in the headgroups. Here, we demonstrate that 1,2-distearoyl-*sn*-*glycero*-3-phosphoinositol (18:0 PI, Figure 3.7a), a phospholipid with an O-linked monosaccharide appended to the phosphate, can assemble into striped phases through microcontact printing (Figure 3.7b–d, models; Figure 3.7e–h, SEM). As with other phospholipids, bringing the stamp into flat contact with the HOPG substrate resulted in assembly of standing

phases (see Appendix B), while rolling contact or stamps treated with UV ozone produced striped phases with domain lengths in some cases >2 μm (Figure 3.7f). Characterization of domain structure based on SEM images is more challenging for these amphiphiles, since they lack the polymerizable diyne group, and thus do not exhibit cracking defects under the electron beam. However, AFM images (Figure 3.7i) reveal a lamellar structure consistent with that predicted by molecular models, with average peak domain heights of ~0.8 nm (Figure 3.7j, corresponding to inositol headgroup ridges), and measured lamellar widths of 5.7 nm (Figure 3.7j), similar to the modeled values of 5.3 nm.

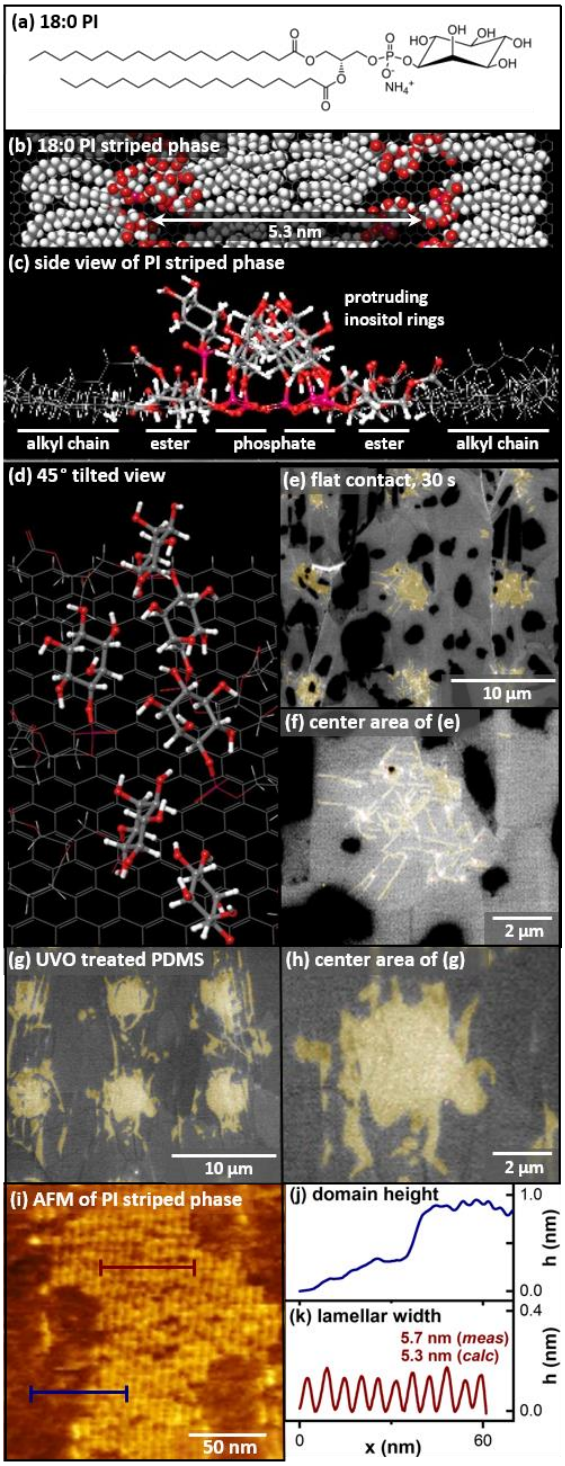

Figure 3.7. (a) Structure of 18:0 phosphoinositol (18:0 PI). (b–d) Minimized molecular models of striped phase of 18:0 PI on HOPG, illustrating: (b) lamellar width, (c) projection of inositol rings, in side view, (d) spacing of inositol rings (45° tilted view). (e–h) SEM images of PI striped phases formed using (e, f) rolling contact and (g, h) UV ozone-treated stamps for microcontact printing. (i) AFM image of PI striped phase, and line scans illustrating (j) domain height and (k) lamellar width.

3.3 Conclusions

Here, we have demonstrated that it is feasible to use microcontact printing to create microscale striped patterns of amphiphiles. Stripes were printed using diynoic acids with chain lengths from 21–29 carbons, diyne phospholipids with phosphocholine and phosphoethanolamine headgroups, and phosphoinositol with 18-carbon saturated chains. The lamellar structures assembled in this way present 1 nm-wide stripes of functional headgroups with pitches from 5–10 nm determined by alkyl chain length. In the cell membrane, amphiphiles with diverse headgroup chemistry, including pendant carbohydrates, are used to mediate interactions with other cells and the extracellular matrix. Our findings point to the possibility that similarly diverse headgroup chemistries could be installed in striped phases, either directly through Langmuir–Schaefer conversion, or through post-assembly modification using common coupling chemistries. Overall, this illustrates a new route for controlled molecular-scale clustering of complex ligands such as carbohydrates at interfaces.

CHAPTER 4. EDGE-ON ADSORPTION OF MULTI-CHAIN FUNCTIONAL ALKANES STABILIZES NONCOVALENT MONOLAYERS ON MoS_2

A version of this chapter has been published in *Chemical Communications*
DOI: 10.1039/C8CC06466K

4.1 Introduction

Surface chemistry of 2D materials is key in controlling not only the substrate electronic structure, but also interactions with the environment. Significant effort has been directed toward controlling the surface chemistry of graphene.[11, 13, 47] Developing routine control over the surface chemistry of other 2D materials such as MoS_2,[119, 120] which have useful electronic properties (*e.g.* native band gaps), would facilitate their application in devices.

Many routes to noncovalent functionalization of 2D materials[11, 13, 47] such as graphene and highly oriented pyrolytic graphite (HOPG) utilize epitaxial matching between the zig-zag alkyl backbone and the hexagonal graphitic lattice (Figure 4.1a and 4.1b), both to strengthen molecule–substrate interactions and to order other functional groups. For example, long chain alkanes (*e.g.* 10,12-pentacosadiynoic acid, PCDA) assemble into striped lamellar phases on HOPG and graphene,[14, 15] with alkyl chains orienting along the $\langle 11\bar{2}0 \rangle$ lattice direction. Lamellar phases of diynes can be photopolymerized to produce conjugated ene–yne polymer backbones, useful both as molecular wires[44] and to stabilize the noncovalent monolayer toward further processing.[18, 19, 22, 47]

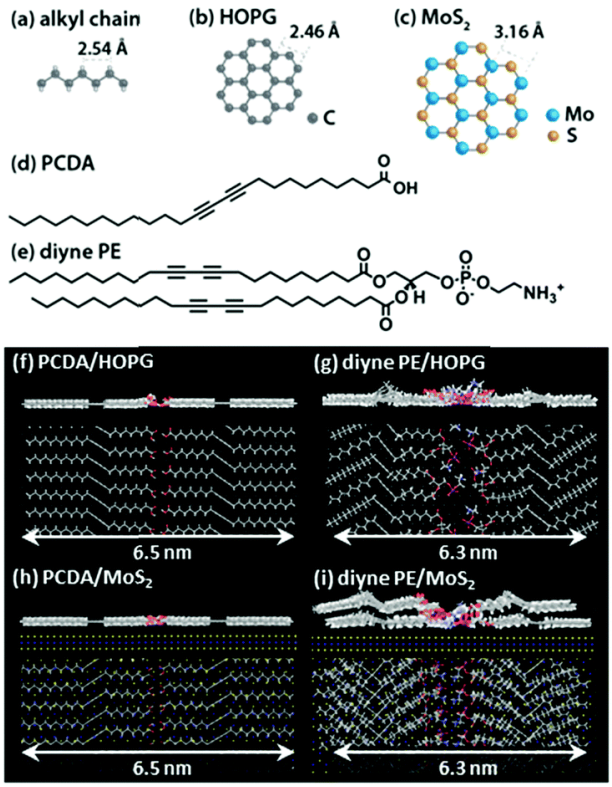

Figure 4.1. (a) Periodicity of the alkyl carbon backbone, and lattice structures of (b) HOPG and (c) MoS_2. Molecular structures of (d) PCDA and (e) diyne PE, and minimized models of lamellar phases of these molecules on (f and g) HOPG and (h and i) MoS_2.

Differences in surface structure reduce stability of such monolayers on MoS_2 in comparison with HOPG; previous calorimetric measurements of adsorption of *n*-dotriacontane from *n*-heptane indicate a 3-fold larger adsorption enthalpy for alkyl chains on HOPG *vs.* MoS_2.[105] Thus, in spite of the increasing interest in controlling MoS_2 surface chemistry, and the fact that lying-down phases on MoS_2 have been visualized by scanning probe microscopy for nearly as long as those on HOPG,[106, 121] relatively few reports demonstrate control of lying-down phases on MoS_2.[17, 24, 120, 122, 123]

Here, we illustrate a structural design principle for increasing ordering and stability of monolayers with weak molecule–substrate interactions, by comparing assembly of two polymerizable amphiphiles on HOPG and MoS_2. PCDA, a single-chain amphiphile (Figure 4.1d), has been broadly used in noncovalent functionalization of HOPG, and also forms lamellar phases on MoS_2. Diyne phosphoethanolamine (diyne PE; Figure 4.1e), a dual-chain amphiphile, has also recently been shown to form lamellar phases on HOPG.[18, 19, 27, 107] In monolayers on HOPG, both

chains typically contact the graphitic lattice (Figure 4.1g). However, in principle such molecules could also adsorb in an edge-on packing in which only one chain interacts with the substrate (Figure 4.1i), an orientation observed for dialkylquinones and alkylated tetrathiafulvalenes at solid–liquid interfaces with HOPG.[124, 125] This geometry would become increasingly favorable on substrates onto which the molecules adsorb weakly, as the molecule–molecule interaction strength becomes a more important driver of monolayer formation. Edge-on packing enables chain–chain interactions in two layers, allowing the formation of two layers of polymer chains (Figure S.C. 1 in Appendix C); both factors potentially increase monolayer stability. Here, we find that diyne PE on MoS_2 forms domain structures consistent with edge-on assembly.

4.2 Results and Discussion

4.2.1 Structure of monolayers on MoS_2

To compare structural and physical properties, monolayers of PCDA and diyne PE were assembled on MoS_2 (Figure 2.2) using the Langmuir–Schaefer transfer method with a custom transfer stage that maintained an elevated substrate temperature.[18] Optimal transfer was observed at substrate temperatures of 50–70 °C, consistent with our previous observations on HOPG,[18] which are used for comparisons here. (A range of assembly conditions was screened for both molecules to compare their assembly properties. Appendix C shows experiments comparing drop-casting, dip-coating, and a range of thermally controlled transfer conditions; overall, diyne PE improved ordering *vs*. PCDA under most conditions tested.) Line scans acquired from AFM images of diyne PE on MoS_2 (Figure 4.2e, blue trace) illustrate two topographic heights associated with the domains. The larger domains visible in Figure 4.2d have heights of ∼0.8 nm, while the smaller domains have average heights of ∼0.4 nm (see Figure S.C.2- S.C.6 in Appendix C). Because 0.8 nm is approximately twice the thickness of diyne PE monolayers on HOPG (red trace) in which both alkyl chains adsorb onto the HOPG surface, we propose that this domain structure arises from edge-on adsorption (Figure 4.1i), and that the 0.4 nm high domains represent face-on adsorption.

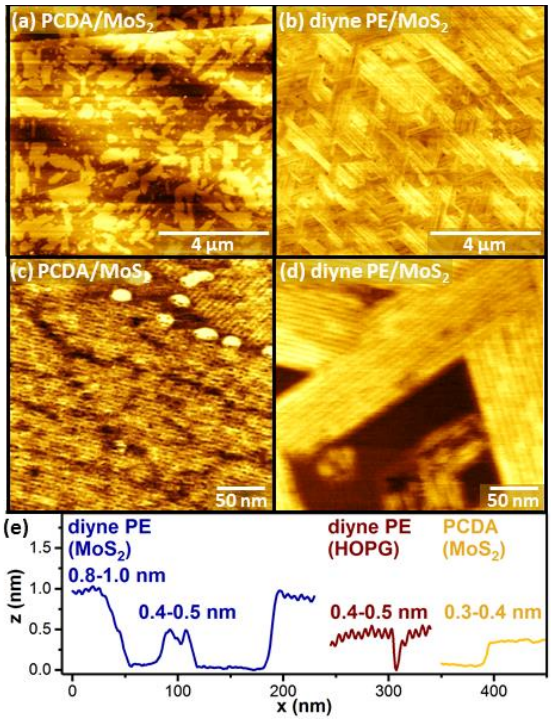

Figure 4.2. AFM images of (a and c) PCDA and (b and d) diyne PE on MoS_2. (e) Line scans extracted over the domains of diyne PE on MoS_2 (blue), HOPG (red), and PCDA on MoS_2 (gold). Figure S.C.2–S.C.5 (Appendix C) show larger versions of the images in (b) and (d) and an image for the diyne PE/HOPG line scan.

4.2.2 Polymerization of monolayers on MoS_2

During UV photopolymerization, we find that monolayers of diyne PE retain lamellar structure longer than monolayers of PCDA; polymerization of both molecules is more rapid on MoS_2 than on HOPG, consistent with earlier studies of PCDA on MoS_2 using STM.[24] AFM images (Figure 4.3) illustrate the progression of PCDA polymerization on MoS_2, for comparison with diyne PE below. Prior to UV irradiation, lamellar domains with edge lengths of ~100 nm are visible (Figure 4.3a); after 10 min (Fig. 3b) and 20 min (Figure 4.3c) of irradiation, the lamellar areas become patchy, largely disappearing at longer irradiation times, although the lamellar domain structures are still visible *via* SEM (Figure 4.3e and f).

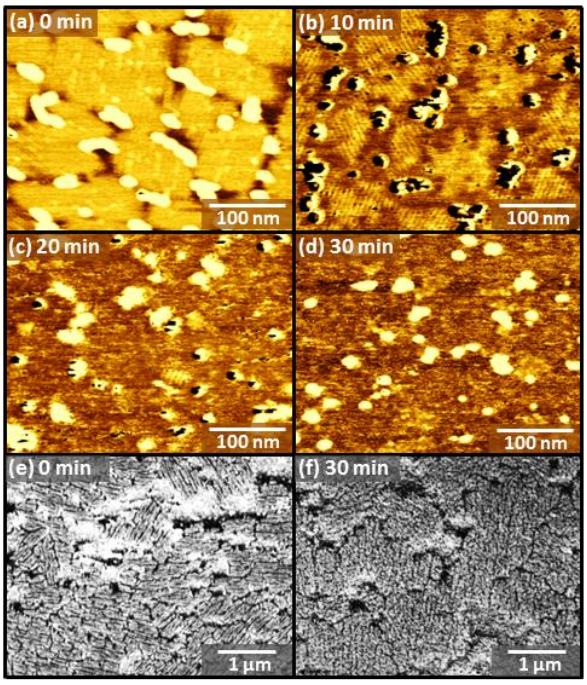

Figure 4.3. AFM images of PCDA on MoS_2: (a) unpolymerized, and polymerized by UV irradiation for (b) 10 min, (c) 20 min, and (d) 30 min. SEM images of PCDA on MoS_2: (e) unpolymerized, and (f) polymerized for 30 min.

The polymerization of diyne PE on MoS_2 also proceeds rapidly, with lamellar roughening within the first 10 min. Unlike PCDA, the lamellar structures remain clearly visible throughout the first 30 min of UV exposure (Figure 4.4a–c), with substantial changes in the monolayer structure between 30 and 60 min (Figure 4.4d) producing features with topographic variations of ~0.6 nm along the domain surfaces, in contrast to 0.1–0.2 nm variations prior to polymerization (Figure 4.4g). Domain edges remain visible *via* SEM after roughening (Figure 4.4f). Similar roughening occurs with longer UV exposure for diyne PE on HOPG (0–6 h, Figure S.C.7, Appendix C).

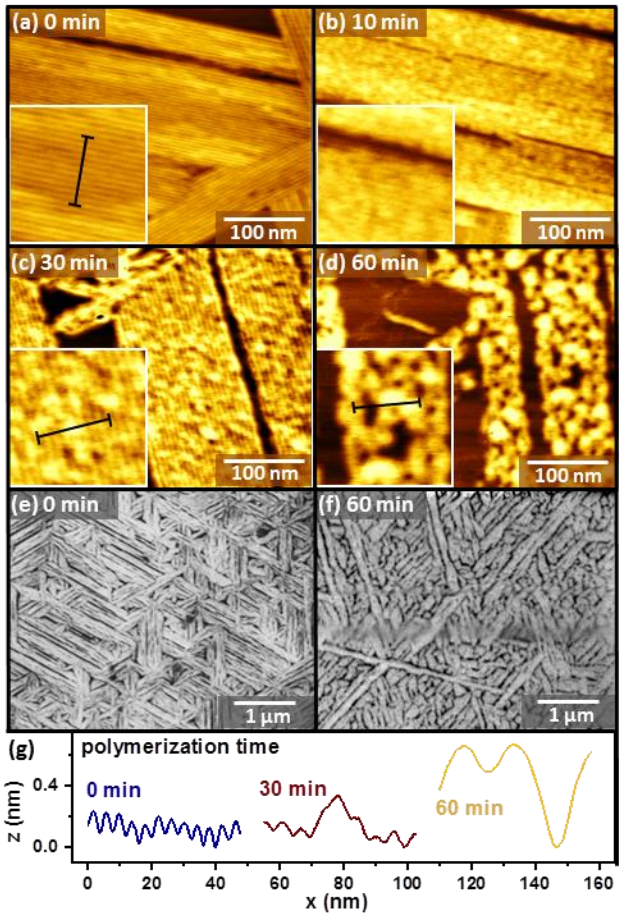

Figure 4.4. AFM images of diyne PE on MoS_2: (a) unpolymerized, and polymerized by UV irradiation for (b) 10 min, (c) 30 min, and (d) 60 min. SEM images of diyne PE on MoS_2: (e) unpolymerized and (f) polymerized for 60 min. (g) AFM line profiles from (a), (c), and (d).

4.2.3 Molecular domain orientations

Edge-on adsorption of diyne PE can occur with the NH_3^+ group being oriented toward the substrate (down) or the environment (up), leading to three possible lamellar median symmetries (down|down, down|up, or up|up). Energy-minimized models (Figure S.C.8 and S.C.9, Appendix C) suggest that NH_3^+-up adsorption is preferred, bringing the glycerol backbone into contact with the substrate. However, the down|up median structure produces lamellae with similar calculated energies, by allowing the lamellar edges to interdigitate (Figure 4.5c).

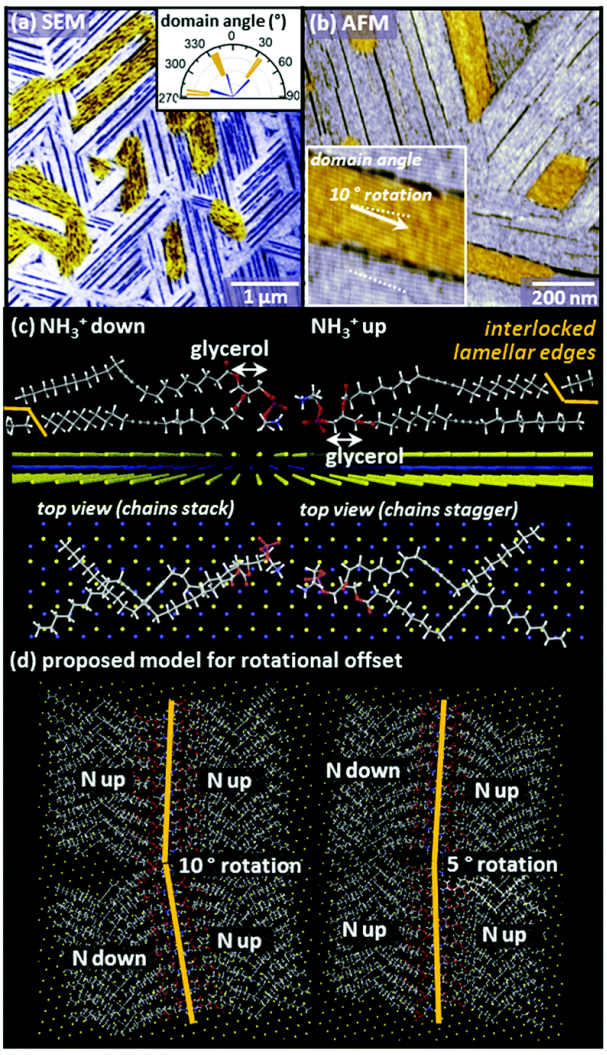

Figure 4.5. Diyne PE on MoS_2: (a) SEM after 20 min UV irradiation and (b) AFM prior to UV irradiation, illustrating two classes of rotational angles (minority domain orientation highlighted in gold). (c) Molecular models of edge-on adsorption of diyne PE with terminal NH_3^+ oriented down (left) and up (right) in proposed majority lamellar structure. (d) Proposed model for rotational offset in lamellar transition from the up|down to the up|up orientation.

In monolayers of diyne PE, we observe two distinct classes of domains with differences in the angular orientation and linear defects (Figure 4.5a and b).[32] A 5–10° rotational offset is observed (wind rose plot, Figure 4.5a) between domains with long linear defects (blue) and those with smaller defects (gold). Large linear vacancies (in blue domains) are visible in the AFM images of both polymerized and unpolymerized monolayers, suggesting that the defects are in assembly. Smaller linear vacancies in gold domains are visible only in SEM images, which is consistent with polymerization-related restructuring observed previously *via* SEM when lamellar narrowing

occurred during polymerization.[32] Domains exhibiting rotational offsets have lamellar widths ~0.2 nm greater than the majority of domains (Figure S.C.6, Appendix C).

A majority (blue) domain structure with an antisymmetric lamellar median (Figure 4.5c) would create interlocked lamellar edges, consistent with lamellae that are narrower by ~0.2 nm. The small overlap at lamellar edges could also reasonably minimize the appearance of cracking during polymerization.

4.2.4 Solvent-stability of diyne PE and PCDA monolayers

Monolayers of diyne PE exhibit an increased stability toward further solution processing, in comparison with polymerized PCDA. Figure 4.6 shows a monolayer of diyne PE polymerized for 15 min (Figure 4.6a) then washed with 5 mL of ethanol (Figure 4.6b). Although the lamellar surface roughens during washing, similar washing of PCDA monolayers (Figure 4.6c and d) produces rounded vacancies and an absence of an obvious lamellar structure, consistent with more substantial monolayer restructuring.

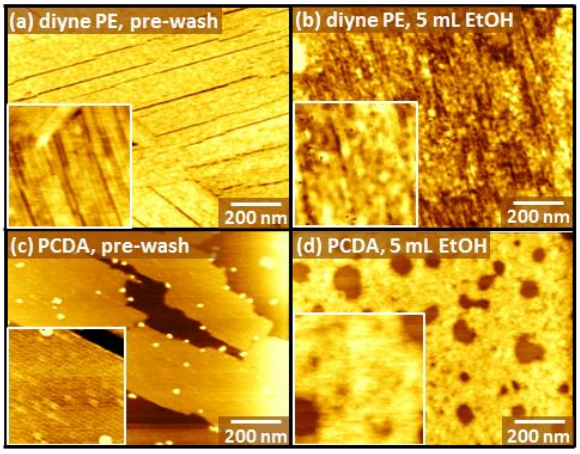

Figure 4.6. AFM images of diyne PE on MoS_2: (a) before and (b) after washing with 5 mL ethanol. PCDA on MoS_2: (c) before and (d) after washing with 5 mL ethanol.

4.3 Conclusions

Here, we examine the role of molecular structure in stabilizing monolayers on MoS_2, by comparing the structure and stability of two different amphiphiles assembled using an optimized LS transfer process at elevated temperature. Overall, we find that diyne PE is capable of forming

ordered molecular domains with edge lengths of several μm on MoS_2, despite the relatively weak alkyl–MoS_2 adsorption enthalpy. Diyne PE domains are substantially larger than those observed for PCDA, and have a thickness of ~0.8 nm consistent with edge-on molecular assembly. Changes in the monolayer structure during polymerization, examined over areas of several μm,[2] illustrate that polymerization of diyne PE occurs ~4-fold faster on MoS_2 than on HOPG. Domains of diyne PE exhibit enhanced stability in comparison with PCDA, during polymerization and in subsequent solvent washing assays. These findings point more generally to the possibility of using edge-on adsorption as a strategy for stabilizing monolayers on layered materials such as MoS_2 onto which alkyl chains adsorb relatively weakly.

CHAPTER 5. A SUB-NM-THICK MULTIFUNCTIONAL POLYMER SKIN FOR SOFT MATERIALS

5.1 Introduction

The ability to control surface chemistry of soft materials to create high-resolution functional patterns would represent a significant advance. Surface chemistry can be used to control local binding to other materials, molecular recognition processes, and wetting.

Molecular monolayers are often used to control the surface chemistry of materials. For instance, functional alkanethiol monolayers on coinage metals (Au, Ag, etc) have been broadly used to change the surface chemistry of the metal surface to control its interactions with the environment.[37] Patterned transfer of alkanethiols to the metal surface using techniques including microcontact printing[8] enables patterning of surface chemistry at μm and 100-nm scales. Silane chemistry can similarly be used to control local functional patterning of SiO_2 and soft materials including poly(dimethylsiloxane) (PDMS).[126, 127]

Noncovalently functionalized 2D materials (*e.g.* graphite, graphene, MoS_2) are notable in regards to interfacial templating, because structural motifs in the monolayer structure enable creation of high-resolution functional patterns with scales well below 10 nm.[11, 13, 27, 41, 128] Molecules in noncovalently adsorbed monolayers on 2D materials such as graphite typically rely in part on large van der Waals contact areas with the substrate (*e.g.* long alkyl chains, polycyclic aromatic hydrocarbons) to stabilize the monolayer.[11, 13] Due to the large area occupied by each molecule on the surface, such monolayers can present structured binding sites including 1-nm wide functional stripes (*e.g.* COOH, NH_2) with ~5-nm pitch, or 1–10 nm pores in which the substrate is exposed; such motifs allow for the adsorption of nanoscopic objects (*e.g.* C_{60}, metallic nanocrystals).[129-133]

The noncovalent molecule–substrate contact confers less stability than the more robust bonds *(e.g.* thiol–Au) that stabilize standing phase monolayers. However, assembly of molecules that incorporate a polymerizable moiety enables molecules within the monolayer to be tethered together, increasing stability. Figure 5.1 illustrates noncovalent lamellar monolayers of diynoic acids and diyne phospholipids, which assemble on highly oriented pyrolytic graphite (HOPG) and other 2D materials. Photopolymerization of the diyne creates a conjugated ene-yne polymer

backbone. The primary interest in this surface chemistry has been in utilization of the ene-yne as molecular wire; however, its presence can also be used to increase monolayer robustness.[18, 19]

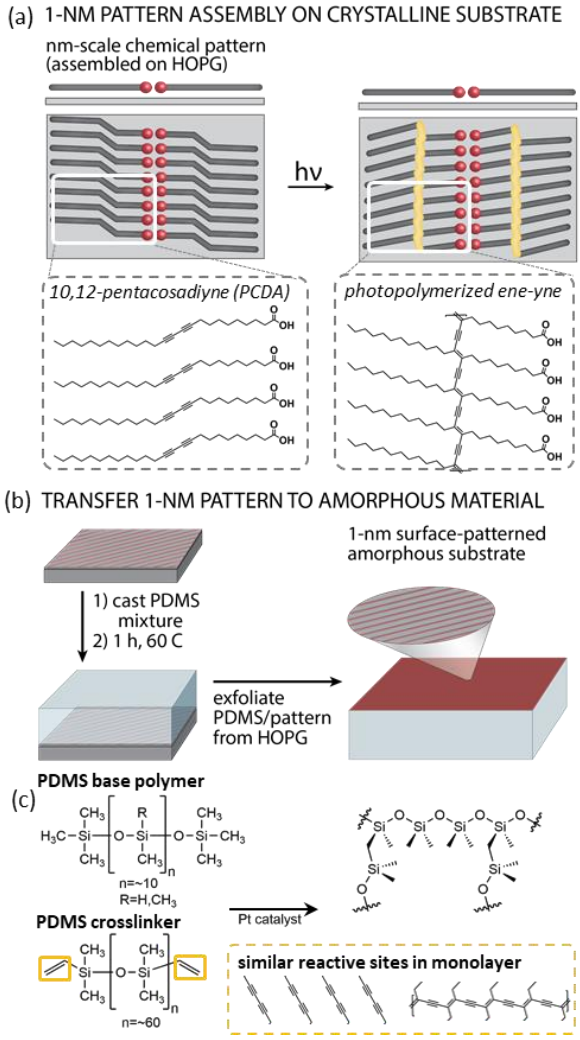

Figure 5.1. (a) Illustration of diyne amphiphile assembly on HOPG and photopolymerization, forming 1-nm-wide functional patterns. (b) Illustration of pattern transfer to the amorphous material. (c) Illustration of hydrosilylation reaction used to exfoliate striped diyne monolayer onto amorphous PDMS elastomer.

Here, we demonstrate that high-resolution functional patterns present in monolayer of this type can be transferred to the surface of a soft, amorphous material. This is achieved by casting PDMS on a pre-assembled polymerized monolayer, and curing the elastomer. After curing, the monolayer remains bound to the surface of the PDMS, creating local patterns in its surface chemistry that modulate its local wetting and interactions with light.

5.2 Results and Discussion

5.2.1 Preparation and transfer of striped monolayers on HOPG

Striped monolayers of 10,12-pentacosadiynoic acid (PCDA) and 1,2-bis(10,12-tricosadiynoyl)-*sn*-glycero-3-phosphoethanolamine (diyne PE, dPE) were prepared via Langmuir-Schaefer (LS) conversion based on procedures reported previously by our group[19, 22, 134] and others.[14, 17, 59] Monolayers were polymerized via UV irradiation; poly dimethylsiloxane (PDMS) was then cast on the monolayers.

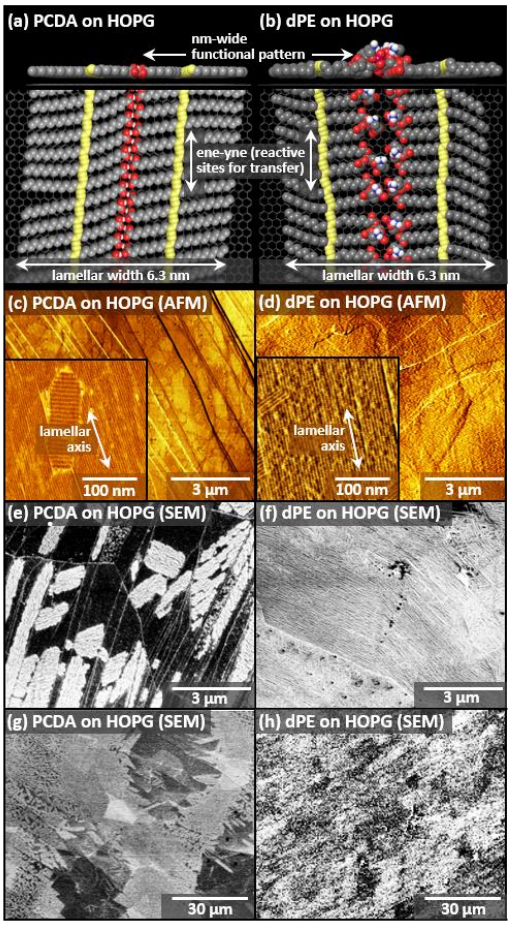

Figure 5.2. (a,b) Molecular models of photopolymerized monolayers of (a) PCDA and (b) diyne PE on HOPG, illustrating lamellar structure and periodicity. (c,d) AFM images of (c) PCDA and (d) diyne PE on HOPG, illustrating domain structure (main image) and lamellar structure (inset). (e–h) SEM images illustrating domain structure of (e) PCDA and (f) diyne PE at scales similar to AFM images in (c,d), and (g,h) at scales similar to those in fluorescence micrographs in later figures.

Monolayers were characterized by AFM and SEM prior to PDMS transfer to examine nanoscopic lamellar structure and microscale domain structure. Molecular models illustrating polymerized PCDA and diyne PE monolayers are shown in Figure 5.2a and Figure 5.2b. In each monolayer, the lamellar axis extends along the direction of the ene-yne polymer backbone (highlighted in gold), with a lamellar width of ~6.3 nm. Paired headgroups (COOH for PCDA and phosphoethanolamine for diyne PE) along the center of each stripe create a 1-nm-wide functional pattern. In AFM images (Figure 5.2c,d), molecular domains are visible at the microscale, along with long linear features representing step edges in the HOPG surface. The inset in each AFM image highlights the local lamellar axis. SEM images (Figure 5.2e,f) acquired at a similar scale to the main AFM images, also reveal molecular domains, visible as brighter regions (regions of stronger electron scattering) against a darker background representing unfunctionalized areas of the HOPG substrate. Larger SEM images (Figure 5.2g,h) illustrate domain structure at a scale similar to that observed in fluorescence images shown in figures below. For most experiments presented here, PCDA monolayers were assembled under conditions our group has previously found to produce large oval vacancies,[32] which provide a convenient internal standard to distinguish optical and other properties of functionalized and unfunctionalized areas of the PDMS.

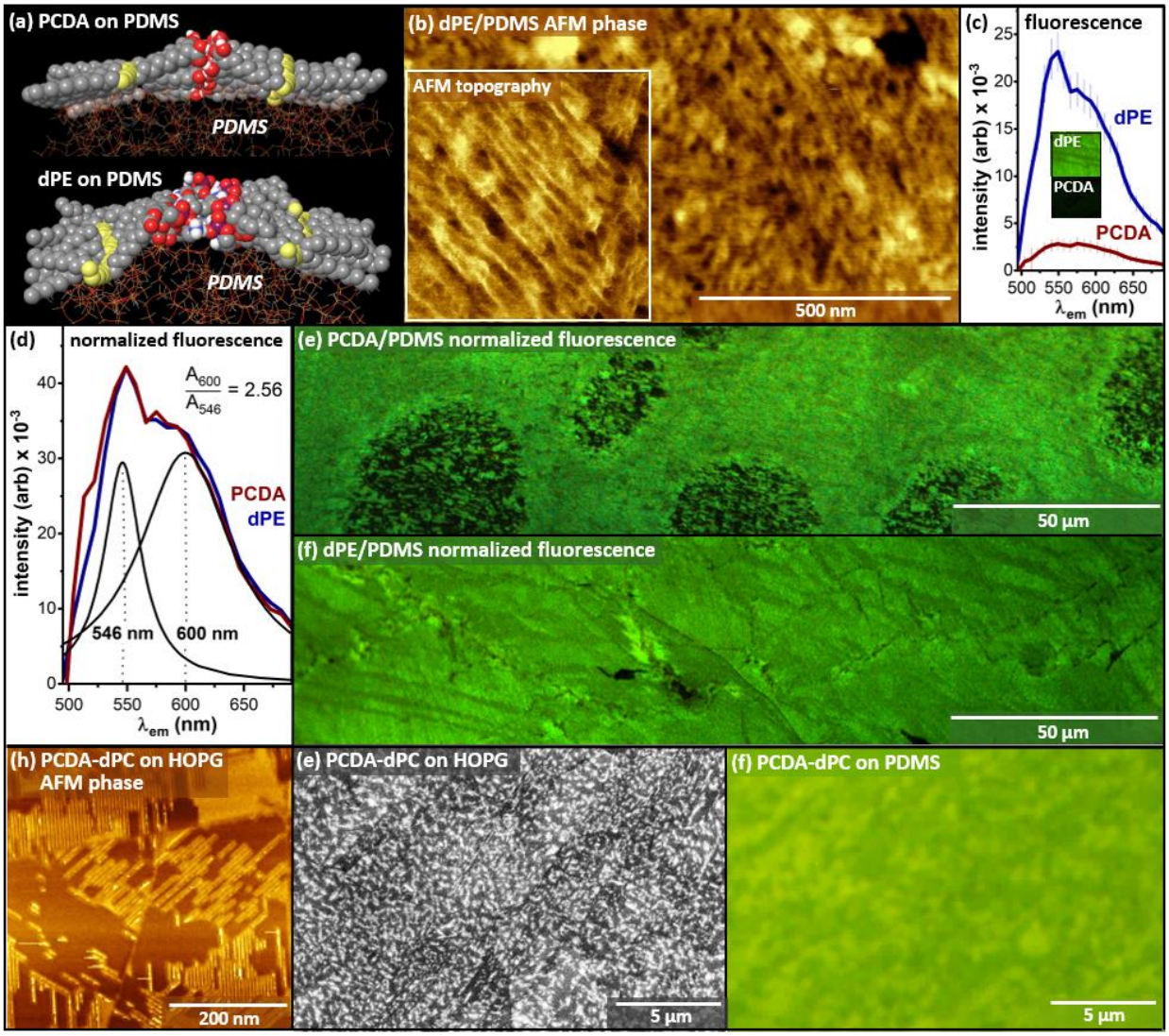

Figure 5.3. (a) Molecular model illustrating polymerized PCDA and diyne PE after transfer to PDMS. (b) AFM image illustrating lamellar structure in diyne PE transferred to PDMS. (c) Fluorescence spectra of PCDA (red trace) and diyne PE (blue trace) on PDMS, illustrating difference in intensity. (d) Normalized fluorescence spectra for PCDA and diyne PE, illustrating similarity of peak shapes. (e,f) Fluorescence micrographs of (e) PCDA/PDMS and (f) diyne PE/PDMS, illustrating domain morphologies similar to those in SEM images in Figure 5.2(g,h), prior to exfoliation from HOPG. (g) AFM phase and (h) SEM images showing mixed monolayer of PCDA and diyne PC on HOPG. (i) Fluorescence micrograph of PCDA-dPC monolayer exfoliated onto PDMS, illustrating variations in fluorescence.

5.2.2 Comparisons of molecular film structure after transfer to PDMS

Covalent monolayer transfer to PDMS would involve changes in local hybridization at points along the ene-yne polymer backbone. Molecular modeling (Figure 5.3a) illustrates

monolayers of PCDA and diyne PE on PDMS, with associated backbone puckering leading to roughening of the monolayer in comparison with the flatter structures on HOPG shown in Figure 5.2a,b. After transfer to PDMS, microscopic monolayer structure is visible in both AFM images (Figure 5.3b) and fluorescence (Figure 5.3c–f). AFM images are surface-sensitive; thus, post-transfer surface features (Figure 5.3b) with morphologies observed in molecular films on HOPG indicate that the molecular layer remains accessible on the surface, an important criterion for further use. Higher-resolution AFM images (Figure 5.3b, inset) reveal nanoscopic vacancies and lamellar orientation. Although the surface appears roughened in comparison with the molecular layer on HOPG (consistent with the molecular models in Figure 5.3a), stripe patterns remain visible on the surface.

Optical properties of the ene-yne backbone provide a useful means of characterizing film structure on PDMS. Visible absorption and emission of the conjugated ene-yne have been extensively studied in standing-phase Langmuir films and bulk crystals of PCDA and similar molecules.[81, 135, 136] Fluorescence microscopy of PCDA or diyne PE on HOPG does not result in observable molecular domain features, consistent with quenching of the ene-yne by the HOPG substrate, and/or formation of the non-fluorescent blue form of the ene-yne polymer. However, PCDA and diyne PE films exfoliated onto PDMS exhibit fluorescence emission (Figure 5.3c), with diyne PE monolayer fluorescence intensity approximately 10x that of PCDA (insets show representative image regions captured under equivalent parameters). Normalizing fluorescence spectra from films of the two molecules (Figure 5.3d) reveals similar emission maxima (λ_1 = 546 nm, λ_2 = 600 nm) and peak shapes, with similar peak area ratios (A_{600}/A_{546} = 2.56). Images of PCDA (Figure 5.3e) and diyne PE (Figure 5.3f) captured and processed under conditions that lead to similar intensities reveal microscopic features similar to those observed in Figure 5.2g and h. Thus, fluorescence microscopy after transfer enables the locations of transferred molecules to be characterized without contacting the surface.

Previous experiments have identified that polydiacetylenes (PDAs) in bulk or in Langmuir multilayers initially polymerize to form a fully-extended PDA backbone with absorbance maxima at 638 nm and 585 nm, which appears blue in transmission. Exposure to heat, UV irradiation, or environmental stimuli that induce sidechain disorder causes torsion of the PDA backbone, reducing effective conjugation length and shifting the absorbance maxima to 535 nm and 500 nm, so the polymer appears red in transmission. Previous experiments have also identified that the blue

form of PDA is nonfluorescent, while the red form has fluorescence emission maxima at 570 nm and 640 nm.[135, 136]

Because fluorescence is associated with the red form of the polymer only, we postulate that the emission intensity is correlated with the amount of red form PDA present in the ROI for each sample.

5.2.3 Transfer of multicomponent films

To maximize functional density in the molecular film, it is important to be able to incorporate different molecular film constituents and distinguish their locations before and after transfer. Mixed monolayers of PCDA and diyne phosphocholine (diyne PC) on HOPG phase segregate, visible in high-resolution AFM phase images (Figure 5.3h) that show clear differences between rows of diyne PC (brigh stripes) and PCDA (dark background). SEM images (Figure 5.3e) exhibit contrast between the two molecules at larger microscopic scales more similar to those observed by fluorescence. Bright (highly scattering) domains in the SEM micrograph correspond to diyne PC. After exfoliation onto PDMS, monolayer regions of with differing fluorescence emission intensities are visible (Figure 5.3f), enabling regions of the two molecules to be distinguished.

This finding points to the capability to identify nanoscopic regions of different headgroup chemistry both before and after transfer, important in using this procedure to functionalize surface so soft, amorphous materials, as well as in aligning multiple transferred layers.

5.2.4 Identifying molecular orientation in transferred molecular films

Identifying the orientation of molecular patterns in the sub-nm-thick films is also possible using polarized fluorescence imaging. The ene-yne polymer backbone can be tens to hundreds of nm in length; previously, others have demonstrated in highly oriented bulk crystals that ene-yne polymers exhibit a polarized free exciton ^1B_u transition, with $\alpha_{\parallel}/\alpha_{\perp} = 600$.[137]

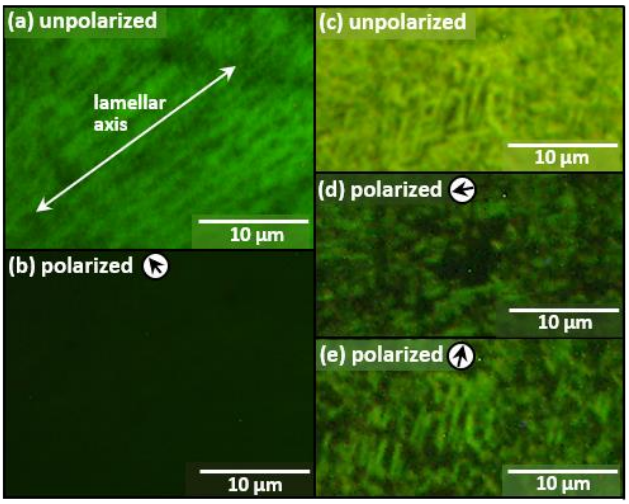

Figure 5.4. (a) Unpolarized and (b) polarized fluorescence micrographs of diyne PE on PDMS. (c) Unpolarized and (d,e) polarized fluorescence micrographs of diyne PE on PDMS, illustrating selective fluorescene emission from domains oriented along the polarization axis in (d,e).

Here, we illustrate that this property can be utilized to identify the orientation of stripes of molecules transferred to PDMS. To maximize visibility, we utilized molecular layers assembled on MoS_2, which previously we have reported produces sets of long, narrow domains with lengths of several µm.[138] Here, when transferred to PDMS, these domain structures create linear features in fluorescence images, with well-defined molecular orientation over scales easy to visualize in fluorescence. Figure 5.6a shows an unpolarized fluorescence image of a molecular film of diyne PE, with the lamellar axis highlighted. When a polarizer is inserted in the emission path, in the orientation shown in Figure 5.6b (arrow in upper right corner of image), emission is not observed. Figure 5.4c–e shows similar behavior in a region with multiple domain orientations. An unpolarized image is shown in Figure 5.4c; polarizing emission along the axis shown by the arrow in Figure 5.4d eliminates detected emission from the series of vertically-oriented molecular domains in the center of the image, while polarization along the axis shown by the arrow in Figure 5.4e restores detected emission from those domains. Chemical manipulation of polymerized molecular films

Previously, it has been demonstrated that exposure of polydiacetylene molecular wires to I_2 reults in doping, increasing conductivity up to 5-fold by creating positive charge carriers, and decreasing HOMO-LUMO energy gaps, resulting in a redshift in fluorescence emission maxima.

Thus, I_2 doping provides a potential path to chemically modulate fluorescence properties of ultrathin molecular films on PDMS to distinguish between patterned areas.

Figure 5.5 illustrates the effect of I2 on the fluorescence of PCDA transferred to PDMS. Here, square patterns of PCDA striped phases deposited on HOPG by microcontact printing, and subsequently transferred to PDMS appear green in fluorescence images (Figure 5.5a). Exposure to I_2 results in a visible shift in fluorescence emission (Figure 5.5b), so that the square pattern appears orange. Comparing fluorescence emission spectra (Figure 5.5c) for doped (orange) and undoped (green) samples reveals a modest redshift of both PDA spectral peaks (from 546 nm to 551 nm and from 600 nm to 607 nm) upon doping, as well as a substantial overall increase in integrated fluorescence intensity. Additionally, Lorentzian fitting of peak areas (fitted peaks for I_2-doped sample shown in black in Figure 5.5c) reveals a substantial increase in the relative intensity of the longer-wavelength emission peak ($A_{\lambda 2}/A_{\lambda 1}$ (undoped) = 2.5, $A_{\lambda 2}/A_{\lambda 1}$ (doped) = 10).

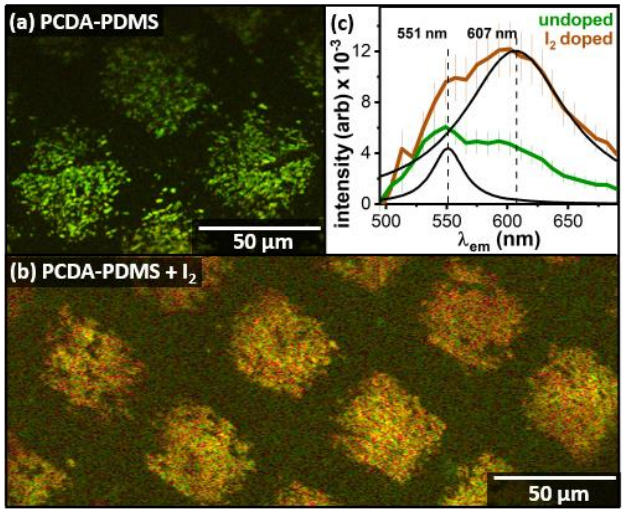

Figure 5.5. (a) Fluorescence image of PCDA monolayer transferred to PDMS. (b) Fluorescence image of PCDA monolayer assembled on HOPG, doped with I_2 (aq), and subsequently transferred to PCDA. (C) Fluorescence spectra of undoped (green) and doped (orange) PCDA films transferred to PDMS, with Lorenzian peak fit for I_2-doped sample shown in black.

Previously others have demonstrated that standing phase molecular layers of polydiacetylenes (e.g. PCDA) can be utilized for sensing of ions, which interact with headgroups, shifting the conformation of the PDA polymer backbone between red and blue forms. Typically,

such measurements are performed on films with thicknesses of several standing phase monolayers (>20 nm total film thickness). The sub-nm-thick lying-down molecular films utilized here are too thin to produce a measurable change in optical absorbance against the PDMS background.

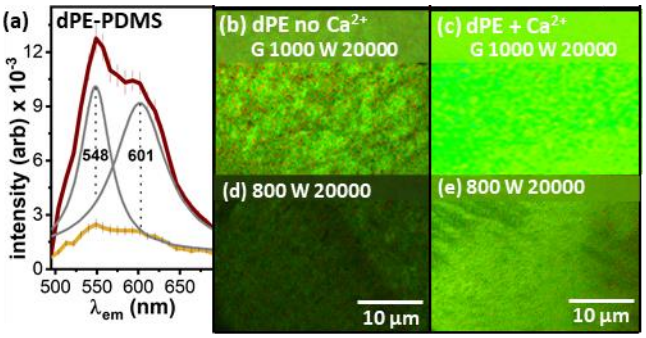

Figure 5.6. (a) Fluorescence spectrum of diyne PE on PDMS with 100 mM Ca^{2+} buffer (red trace) illustrating 4-fold increase in fluorescence intensity vs diyne PE/PDMS without Ca^{2+} (gold trace). Fluorescence micrographs of diyne PE on PDMS (b,d) without and (c,e) with Ca^{2+} buffer.

However, we demonstrate that interactions with buffers containing divalent ions (here, 100 mM Ca^{2+}) can modulate observable fluorescence emission (Figure 5.6a, λ_1 = 548 nm, λ_2 = 601 nm).for transferred monolayers of diyne PE where an approximately 6-fold increase in integrated fluorescence intensity is observed for monolayers in the presence of Ca^{2+} (red trace) in comparison with no Ca^{2+} (gold trace). Images in Figure 5.6b,c illustrate that diyne PE monolayers exhibit stronger fluorescence.

5.2.5 Wetting of molecular film before and after transfer

The primary amine on diyne PE can serve as a functional handle for further coupling reactions, allowing the chemistry of the polymer skin to be modulated as desired based on application. In comparison with noncovalently adsorbed monolayers on HOPG, covalent crosslinking of the ene-yne backbone to the PDMS would be expected to increase stability of the monolayer toward post-functionalization.

To assess headgroup accessibility and reactivity, diyne PE surfaces were prepared on HOPG under LS transfer condition that generate low-density circles surrounded by higher density domains and standing-phase domains (Figure 5.7a, SEM of monolayer on HOPG). This approach provides regions morphologically controlled regions with different contrast within each image.

Following covalent transfer of the diyne PE monolayers to PDMS (Figure 5.7b), substrates were immersed in a reaction mixture containing Rhodamine red (RR) NHS ester and allowed to react for 24 h. Following reaction, the functionalized diyne PE/PDMS substrates were vigorously washed with EtOH for 1 min. To ensure no physiosorbed RR remained on the surface, RR-functionalized diyne PE/PDMS substrates were then sonicated in solvents ranging in polarity from water to hexanes, for multiple hours in each solvent. Figure 5.7C shows the fluorescence micrograph of a diyne PE/PDMS+RR surface after this process was repeated twice, showing no significant change in fluorescence. Figure 5.7d shows the emission spectrum of diyne PE/PDMS (green) excited with a 488 nm laser and the diyne PE/PDMS-RR (orange) excited with a 584 nm laser. Overall, we observe an approximately 4-fold increase in fluorescence intensity at the emission maximum

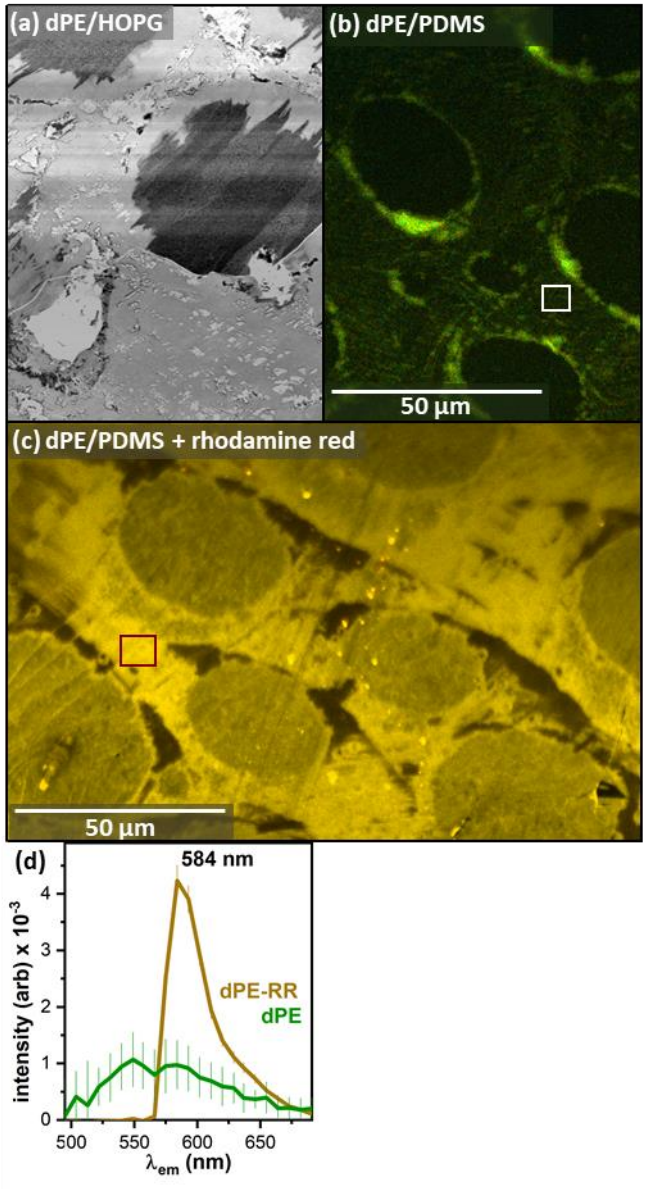

Figure 5.7. (A) SEM image of diyne PE monolayer assembled on HOPG. (b) Fluorescence image of low-density diyne PE monolayer transferred to PDMS. (c) Fluorescence image of diyne PE monolayer transferred to PDMS, after reaction with NHS-ester RR and subsequent vigorous washing. (d) Fluorescence spectra of diyne PE (green) and RR-modified (orange) diyne PE films.

5.3 Conclusions

Here, we show that striped monolayers of polymerized diyne amphiphiles on HOPG can be exfoliated with an *in situ* cured elastomeric material. This process creates polymer films < 1 nm thick that maintains their anisotropy post transfer and can be characterized via fluorescence microscopy. Diyne PE and PCDA have the same emission peaks but Diyne PE is brighter due to

greater lamellae roughening post transfer leading to more red phase character. Transferred films exhibit polarized emission from the ene-yne polymer backbone, revealing molecular orientation. The fluorescence spectrum of the films can be chemically manipulated using I_2 doping to red shift the spectra or by adding divalent cations to increase spectral intensity. The surface can further be modified by using the primary amines as a handle for coupling reaction. The example shown here is the addition of rhodamine red to the primary amine which can be seen in the fluorescence spectrum. Together, these findings point to routes for maximizing functional density in a molecular film, controlling interactions with the environment

REFERENCES

1. Ostroverkhova, O., Organic Optoelectronic Materials: Mechanisms and Applications. *Chemical Reviews* **2016,** *116* (22), 13279-13412.

2. Asenov, A.; Kaya, S.; Brown, A. R., Intrinsic parameter fluctuations in decananometer MOSFETs introduced by gate line edge roughness. *Ieee Transactions on Electron Devices* **2003,** *50* (5), 1254-1260.

3. Shin, C., State-of-the-art silicon device miniaturization technology and its challenges. *Ieice Electronics Express* **2014,** *11* (10).

4. Butler, S. Z.; Hollen, S. M.; Cao, L. Y.; Cui, Y.; Gupta, J. A.; Gutierrez, H. R.; Heinz, T. F.; Hong, S. S.; Huang, J. X.; Ismach, A. F.; Johnston-Halperin, E.; Kuno, M.; Plashnitsa, V. V.; Robinson, R. D.; Ruoff, R. S.; Salahuddin, S.; Shan, J.; Shi, L.; Spencer, M. G.; Terrones, M.; Windl, W.; Goldberger, J. E., Progress, Challenges, and Opportunities in Two-Dimensional Materials Beyond Graphene. *Acs Nano* **2013,** *7* (4), 2898-2926.

5. Geim, A. K., Graphene: Status and Prospects. *Science* **2009,** *324* (5934), 1530-1534.

6. Paivanranta, B.; Langner, A.; Kirk, E.; David, C.; Ekinci, Y., Sub-10 nm patterning using EUV interference lithography. *Nanotechnology* **2011,** *22* (37).

7. Li, L.; Liu, X.; Pal, S.; Wang, S. L.; Ober, C. K.; Giannelis, E. P., Extreme ultraviolet resist materials for sub-7 nm patterning. *Chemical Society Reviews* **2017,** *46* (16), 4855-4866.

8. Xia, Y. N.; Whitesides, G. M., Soft lithography. *Annual Review of Materials Science* **1998,** *28*, 153-184.

9. Kane, R. S.; Takayama, S.; Ostuni, E.; Ingber, D. E.; Whitesides, G. M., Patterning proteins and cells using soft lithography. *Biomaterials* **1999,** *20* (23-24), 2363-2376.

10. Piner, R. D.; Zhu, J.; Xu, F.; Hong, S. H.; Mirkin, C. A., "Dip-pen" nanolithography. *Science* **1999,** *283* (5402), 661-663.

11. MacLeod, J. M.; Rosei, F., Molecular Self-Assembly on Graphene. *Small* **2014,** *10* (6), 1038-1049.

12. Giancarlo, L. C.; Flynn, G. W., Scanning tunneling and atomic force microscopy probes of self-assembled, physisorbed monolayers: Peeking at the peaks. *Annual Review of Physical Chemistry* **1998,** *49*, 297-+.

13. Mann, J. A.; Dichtel, W. R., Noncovalent Functionalization of Graphene by Molecular and Polymeric Adsorbates. *J. Phys. Chem. Lett.* **2013,** *4* (16), 2649-2657.

14. Okawa, Y.; Aono, M., Linear chain polymerization initiated by a scanning tunneling microscope tip at designated positions. *Journal of Chemical Physics* **2001,** *115* (5), 2317-2322.

15. Grim, P. C. M.; De Feyter, S.; Gesquiere, A.; Vanoppen, P.; Rucker, M.; Valiyaveettil, S.; Moessner, G.; Mullen, K.; De Schryver, F. C., Submolecularly resolved polymerization of diacetylene molecules on the graphite surface observed with scanning tunneling microscopy. *Angewandte Chemie-International Edition* **1997,** *36* (23), 2601-2603.

16. Akai-Kasaya, M.; Shimizu, K.; Watanabe, Y.; Saito, A.; Aono, M.; Kuwahara, Y., Electronic structure of a polydiacetylene nanowire fabricated on highly ordered pyrolytic graphite. *Physical Review Letters* **2003,** *91* (25).

17. Giridharagopal, R.; Kelly, K. F., Substrate-dependent properties of polydiacetylene nanowires on graphite and MoS_2. *ACS Nano* **2008,** *2* (8), 1571-1580.

18. Hayes, T. R.; Bang, J. J.; Davis, T. C.; Peterson, C. F.; McMillan, D. G.; Claridge, S. A., Multimicrometer Noncovalent Monolayer Domains on Layered Materials through Thermally Controlled Langmuir-Schaefer Conversion for Noncovalent 2D Functionalization. *Acs Applied Materials & Interfaces* **2017,** *9* (41), 36409-36416.

19. Bang, J. J.; Rupp, K. K.; Russell, S. R.; Choong, S. W.; Claridge, S. A., Sitting Phases of Polymerizable Amphiphiles for Controlled Functionalization of Layered Materials. *Journal of the American Chemical Society* **2016,** *138* (13), 4448-4457.

20. Verveniotis, E.; Okawa, Y.; Makarova, M. V.; Koide, Y.; Liu, J. W.; Smid, B.; Watanabe, K.; Taniguchi, T.; Komatsu, K.; Minari, T.; Liu, X. Y.; Joachim, C.; Aono, M., Self-assembling diacetylene molecules on atomically flat insulators. *Physical Chemistry Chemical Physics* **2016,** *18* (46), 31600-31605.

21. Bang, J. J.; Russell, S. R.; Rupp, K. K.; Claridge, S. A., Multimodal scanning probe imaging: nanoscale chemical analysis from biology to renewable energy. *Analytical Methods* **2015,** *7* (17), 7106-7127.

22. Choong, S. W.; Russell, S. R.; Bang, J. J.; Patterson, J. K.; Claridge, S. A., Sitting Phase Monolayers of Polymerizable Phospholipids Create Dimensional, Molecular-Scale Wetting Control for Scalable Solution Based Patterning of Layered Materials. *Acs Applied Materials & Interfaces* **2017,** *9* (22), 19326-19334.

23. Porter, A. G.; Ouyang, T.; Hayes, T. R.; Biechele-Speziale, J.; Russell, S. R.; Claridge, S. A., 1-nm-Wide Hydrated Dipole Arrays Regulate AuNW Assembly on Striped Monolayers in Nonpolar Solvent. *Chem* **2019,** *5* (8), 2264-2275.

24. Mandal, S. K.; Okawa, Y.; Hasegawa, T.; Aono, M., Rate-Determining Factors in the Chain Polymerization of Molecules Initiated by Local Single-Molecule Excitation. *Acs Nano* **2011,** *5* (4), 2779-2786.

25. Sullivan, S. P.; Schmeders, A.; Mbugua, S. K.; Beebe, T. P., Controlled polymerization of substituted diacetylene self-organized monolayers confined in molecule corrals. *Langmuir* **2005,** *21* (4), 1322-1327.

26. Takajo, D.; Okawa, Y.; Hasegawa, T.; Aono, M., Chain polymerization of diacetylene compound multilayer films on the topmost surface initiated by a scanning tunneling microscope tip. *Langmuir* **2007,** *23* (10), 5247-5250.

27. Claridge, S. A., Standing, lying, and sitting: translating building principles of the cell membrane to synthetic 2D material interfaces. *Chemical Communications* **2018,** *54* (50), 6681-6691.

28. Liang, R.; Yan, L.; Loebach, J.; Ge, M.; Uozumi, Y.; Sekanina, K.; Horan, N.; Gildersleeve, J.; Thompson, C.; Smith, A.; Biswas, K.; Still, W. C.; Kahne, D., Parallel synthesis and screening of a solid phase carbohydrate library. *Science* **1996,** *274* (5292), 1520-1522.

29. Oyelaran, O.; Gildersleeve, J. C., Glycan arrays: recent advances and future challenges. *Current Opinion in Chemical Biology* **2009,** *13* (4), 406-413.

30. Davis, T. C.; Bechtold, J. O.; Hayes, T. R.; Villarreal, T. A.; Claridge, S. A., Hierarchically Patterned Striped Phases of Polymerized Lipids: Toward Controlled Carbohydrate Presentation at Interfaces. *Accepted to Faraday Discussions* **2019**.

31. Davis, T. C.; Russell, S. R.; Claridge, S. A., Edge-on adsorption of multi-chain functional alkanes stabilizes noncovalent monolayers on MoS2. *Chemical Communications* **2018,** *54* (83), 11709-11712.

32. Davis, T. C.; Bang, J. J.; Brooks, J. T.; McMillan, D. G.; Claridge, S. A., Hierarchically Patterned Noncovalent Functionalization of 2D Materials by Controlled Langmuir-Schaefer Conversion. *Langmuir* **2018,** *34* (4), 1353-1362.

33. 1-nm-Wide Hydrated Dipole Arrays Regulate AuNW Assembly on Striped Monolayers in Nonpolar Solvent. *Chem* **2019,** *5* (8), 2264 - 2275.

34. Weibel, D. B.; DiLuzio, W. R.; Whitesides, G. M., Microfabrication meets microbiology. *Nature Reviews Microbiology* **2007,** *5* (3), 209-218.

35. Piriya, A. V. S.; Joseph, P.; Daniel, K. S. C. G.; Lakshmanan, S.; Kinoshita, T.; Muthusamy, S., Colorimetric sensors for rapid detection of various analytes. *Materials Science & Engineering C-Materials for Biological Applications* **2017,** *78*, 1231-1245.

36. Roth, L. E.; Valles, E. M.; Villar, M. A., Bulk hydrosilylation reaction of poly(dimethylsiloxane) chains catalyzed by a platinum salt: Effect of the initial concentration of reactive groups on the final extent of reaction. *Journal of Polymer Science Part a-Polymer Chemistry* **2003,** *41* (8), 1099-1106.

37. Love, J. C.; Estroff, L. A.; Kriebel, J. K.; Nuzzo, R. G.; Whitesides, G. M., Self-assembled monolayers of thiolates on metals as a form of nanotechnology. *Chemical Reviews* **2005,** *105* (4), 1103-1169.

38. Claridge, S. A.; Liao, W.-S.; Thomas, J. C.; Zhao, Y.; Cao, H. H.; Cheunkar, S.; Serino, A. C.; Andrews, A. M.; Weiss, P. S., From the bottom up: dimensional control and characterization in molecular monolayers. *Chemical Society Reviews* **2013,** *42* (7), 2725-2745.

39. Liao, W.-S.; Cheunkar, S.; Cao, H. H.; Bednar, H. R.; Weiss, P. S.; Andrews, A. M., Subtractive Patterning via Chemical Lift-Off Lithography. *Science* **2012,** *337* (6101), 1517-1521.

40. Cyr, D. M.; Venkataraman, B.; Flynn, G. W., STM investigations of organic molecules physisorbed at the liquid-solid interface. *Chemistry of Materials* **1996,** *8* (8), 1600-1615.

41. De Feyter, S.; De Schryver, F. C., Self-assembly at the liquid/solid interface: STM reveals. *Journal of Physical Chemistry B* **2005,** *109* (10), 4290-4302.

42. Okawa, Y.; Mandal, S. K.; Hu, C.; Tateyama, Y.; Goedecker, S.; Tsukamoto, S.; Hasegawa, T.; Gimzewski, J. K.; Aono, M., Chemical Wiring and Soldering toward All-Molecule Electronic Circuitry. *Journal of the American Chemical Society* **2011,** *133* (21), 8227-8233.

43. Russell, S. R.; Claridge, S. A., Peptide interfaces with graphene: an emerging intersection of analytical chemistry, theory, and materials. *Analytical and Bioanalytical Chemistry* **2016,** *408* (11), 2649-2658.

44. Okawa, Y.; Akai-Kasaya, M.; Kuwahara, Y.; Mandal, S. K.; Aono, M., Controlled chain polymerisation and chemical soldering for single-molecule electronics. *Nanoscale* **2012,** *4* (10), 3013-3028.

45. Tieke, B.; Graf, H. J.; Wegner, G.; Naegele, B.; Ringsdorf, H.; Banerjie, A.; Day, D.; Lando, J. B., Polymerization Of Monolayer And Multilayer Forming Diacetylenes. *Colloid and Polymer Science* **1977,** *255* (6), 521-531.

46. Li, B.; Tahara, K.; Adisoejoso, J.; Vanderlinden, W.; Mali, K. S.; De Gendt, S.; Tobe, Y.; De Feyter, S., Self-Assembled Air-Stable Supramolecular Porous Networks on Graphene. *Acs Nano* **2013,** *7* (12), 10764-10772.

47. Mali, K. S.; Pearce, N.; De Feyter, S.; Champness, N. R., Frontiers of supramolecular chemistry at solid surfaces. *Chemical Society Reviews* **2017,** *46* (9), 2520-2542.

48. Villarreal, T. A.; Russell, S. R.; Bang, J. J.; Patterson, J. K.; Claridge, S. A., Modulating Wettability of Layered Materials by Controlling Ligand Polar Headgroup Dynamics. *Journal of the American Chemical Society* **2017,** *139* (34), 11973-11979.

49. Langmuir, I.; Schaefer, V. J., Activities of urease and pepsin monolayers. *Journal of the American Chemical Society* **1938,** *60*, 1351-1360.

50. Vollhardt, D.; Fainerman, V. B., Characterisation of phase transition in adsorbed monolayers at the air/water interface. *Advances in Colloid and Interface Science* **2010,** *154* (1-2), 1-19.

51. Kaganer, V. M.; Mohwald, H.; Dutta, P., Structure and phase transitions in Langmuir monolayers. *Reviews of Modern Physics* **1999,** *71* (3), 779-819.

52. Knobler, C. M.; Schwartz, D. K., Langmuir and self-assembled monolayers. *Current Opinion in Colloid & Interface Science* **1999,** *4* (1), 46-51.

53. Schwartz, D. K., Mechanisms and kinetics of self-assembled monolayer formation. *Annual Review of Physical Chemistry* **2001,** *52*, 107-137.

54. Ege, C.; Ratajczak, M. K.; Majewski, J.; Kjaer, K.; Lee, K. Y. C., Evidence for lipid/cholesterol ordering in model lipid membranes. *Biophysical Journal* **2006,** *91* (1), L1-L3.

55. Ding, J. Q.; Takamoto, D. Y.; von Nahmen, A.; Lipp, M. M.; Lee, K. Y. C.; Waring, A. J.; Zasadzinski, J. A., Effects of lung surfactant proteins, SP-B and SP-C, and palmitic acid on monolayer stability. *Biophysical Journal* **2001,** *80* (5), 2262-2272.

56. Blodgett, K. B., Monomolecular films of fatty acids on glass. *Journal of the American Chemical Society* **1934,** *56*, 495-495.

57. Chen, X.; Lenhert, S.; Hirtz, M.; Lu, N.; Fuchs, H.; Chi, L., Langmuir-Blodgett patterning: A bottom-up way to build mesostructures over large areas. *Accounts of Chemical Research* **2007,** *40* (6), 393-401.

58. Frey, S.; Chi, E. Y.; Arratia, C.; Majewski, J.; Kjaer, K.; Lee, K. Y. C., Condensing and fluidizing effects of ganglioside G(M1) on phospholipid films. *Biophysical Journal* **2008,** *94* (8), 3047-3064.

59. Miura, A.; De Feyter, S.; Abdel-Mottaleb, M. M. S.; Gesquiere, A.; Grim, P. C. M.; Moessner, G.; Sieffert, M.; Klapper, M.; Mullen, K.; De Schryver, F. C., Light- and STM-tip-induced formation of one-dimensional and two-dimensional organic nanostructures. *Langmuir* **2003,** *19* (16), 6474-6482.

60. Giridharagopal, R.; Kelly, K. F., STM-Induced desorption of polydiacetylene nanowires and reordering via molecular cascades. *Journal of Physical Chemistry C* **2007,** *111* (17), 6161-6166.

61. Okawa, Y.; Aono, M., Materials science - Nanoscale control of chain polymerization. *Nature* **2001,** *409* (6821), 683-684.

62. Takami, K.; Kuwahara, Y.; Ishii, T.; Akai-Kasaya, M.; Saito, A.; Aono, M., Significant increase in conductivity of polydiacetylene thin film induced by iodine doping. *Surface Science* **2005,** *591* (1-3), L273-L279.

63. Morelis, R. M.; Girardegrot, A. P.; Coulet, P. R., dependence of langmuir-blodgett-film quality on fatty-acid monolayer integrity .1. Nucleation crystal-growth avoidance in the monolayer through the optimized compression procedure. *Langmuir* **1993,** *9* (11), 3101-3106.

64. Girardegrot, A. P.; Morelis, R. M.; Coulet, P. R., dependence of langmuir-blodgett-film quality on fatty-acid monolayer integrity .2. Crucial effect of the removal rate of monolayer during langmuir-blodgett-film deposition. *Langmuir* **1993,** *9* (11), 3107-3110.

65. Aveyard, R.; Binks, B. P.; Fletcher, P. D. I.; Ye, X., Contact Angles And Transfer Ratios Measured During The Langmuir-Blodgett Deposition Of Docosanoic Acid Onto Mica From Cdcl2 Subphases. *Colloids and Surfaces a-Physicochemical and Engineering Aspects* **1995,** *94* (2-3), 279-289.

66. Langmuir, I.; Schaefer, V. J.; Sobotka, H., Multilayers of sterols and the adsorption of digitonin by deposited monolayers. *Journal of the American Chemical Society* **1937,** *59*, 1751-1759.

67. Honig, E. P.; Hengst, J. H. T.; Denengel.D, LANGMUIR-BLODGETT DEPOSITION RATIOS. *Journal of Colloid and Interface Science* **1973,** *45* (1), 92-102.

68. Blodgett, K. B., Films built by depositing successive monomolecular layers on a solid surface. *Journal of the American Chemical Society* **1935,** *57* (1), 1007-1022.

69. Liu, J.; Conboy, J. C., 1,2-diacyl-phosphatidylcholine flip-flop measured directly by sum-frequency vibrational spectroscopy. *Biophysical Journal* **2005,** *89* (4), 2522-2532.

70. Lopez, G. P.; Biebuyck, H. A.; Whitesides, G. M., Scanning Electron-Microscopy Can Form Images Of Patterns In Self-Assembled Monolayers. *Langmuir* **1993,** *9* (6), 1513-1516.

71. Srinivasan, C.; Mullen, T. J.; Hohman, J. N.; Anderson, M. E.; Dameron, A. A.; Andrews, A. M.; Dickey, E. C.; Horn, M. W.; Weiss, P. S., Scanning electron microscopy of nanoscale chemical patterns. *Acs Nano* **2007,** *1* (3), 191-201.

72. Mack, N. H.; Dong, R.; Nuzzo, R. G., Quantitative imaging of protein adsorption on patterned organic thin-film arrays using secondary electron emission. *Journal of the American Chemical Society* **2006,** *128* (24), 7871-7881.

73. Bittermann, A. G.; Jacobi, S.; Chi, L. F.; Fuchs, H.; Reichelt, R., Contrast studies on organic monolayers of different molecular packing in FESEM and their correlation with SFM data. *Langmuir* **2001,** *17* (6), 1872-1877.

74. Moore, B. G.; Knobler, C. M.; Akamatsu, S.; Rondelez, F., Phase-Diagram Of Langmuir Monolayers Of Pentadecanoic Acid - Quantitative Comparison Of Surface Pressure And Fluorescence Microscopy Results. *Journal of Physical Chemistry* **1990,** *94* (11), 4588-4595.

75. Doudevski, I.; Hayes, W. A.; Schwartz, D. K., Submonolayer island nucleation and growth kinetics during self-assembled monolayer formation. *Physical Review Letters* **1998,** *81* (22), 4927-4930.

76. Chi, L. F.; Eng, L. M.; Graf, K.; Fuchs, H., Structure And Stability Of Langmuir-Blodgett-Films Investigated By Scanning Force Microscopy. *Langmuir* **1992,** *8* (9), 2255-2261.

77. Chi, L. F.; Fuchs, H.; Johnston, R. R.; Ringsdorf, H., Investigations Of Phase-Separated Langmuir-Blodgett-Films BY ATOMIC-FORCE MICROSCOPY. *Thin Solid Films* **1994,** *242* (1-2), 151-156.

78. Riegler, h.; spratte, k., Structural-Changes In Lipid Monolayers During The Langmuir-Blodgett Transfer Due To Substrate Monolayer Interactions. *Thin Solid Films* **1992,** *210* (1-2), 9-12.

79. Rana, F. R.; Widayati, S.; Gregory, B. W.; Dluhy, R. A., Metastability In Monolayer Films Transferred Onto Solid Substrates By The Langmuir-Blodgett Method - Ir Evidence For Transfer-Induced Phase-Transitions. *Applied Spectroscopy* **1994,** *48* (10), 1196-1203.

80. Wegner, G., topochemical reactions of monomers with conjugated triple-bonds .4. Polymerization of bis-(para-toluene sulfonate) of 2.4-hexadiin-1.6-diol. *Makromolekulare Chemie* **1971,** *145* (JUL), 85-&.

81. Tieke, B.; Lieser, G.; Wegner, G., POLYMERIZATION OF DIACETYLENES IN MULTILAYERS. *Journal of Polymer Science Part a-Polymer Chemistry* **1979,** *17* (6), 1631-1644.

82. Baughman, R. H., Solid-State Polymerization Of Diacetylenes. *Journal of Applied Physics* **1972,** *43* (11), 4362-&.

83. Wegner, G., topochemical reactions of monomers with conjugated triple bonds .i. Polymerization of 2.4-hexadiyn-1.6-diols deivatives in crystalline state. *Zeitschrift Fur Naturforschung Part B-Chemie Biochemie Biophysik Biologie Und Verwandten Gebiete* **1969,** *B 24* (7), 824-&.

84. Bassler, H., Photopolymerization Of Diacetylenes. *Advances in Polymer Science* **1984,** *63*, 1-48.

85. Robinson, K. M.; Hernandez, C.; Mann, J. A., Insitu X-Ray-Diffraction Of Diacetylene Monolayers. *Thin Solid Films* **1992,** *210* (1-2), 73-75.

86. Doudevski, I.; Hayes, W. A.; Woodward, J. T.; Schwartz, D. K., Atomic force microscope imaging of molecular aggregation during self-assembled monolayer growth. *Colloids and Surfaces a-Physicochemical and Engineering Aspects* **2000,** *174* (1-2), 233-243.

87. Yuan, C. B.; Furlong, J.; Burgos, P.; Johnston, L. J., The size of lipid rafts: An atomic force microscopy study of ganglioside GM1 domains in sphingomyelin/DOPC/cholesterol membranes. *Biophysical Journal* **2002,** *82* (5), 2526-2535.

88. Silvius, J. R., Role of cholesterol in lipid raft formation: lessons from lipid model systems. *Biochimica Et Biophysica Acta-Biomembranes* **2003,** *1610* (2), 174-183.

89. Steinem, C.; Janshoff, A.; Ulrich, W. P.; Sieber, M.; Galla, H. J., Impedance analysis of supported lipid bilayer membranes: A scrutiny of different preparation techniques. *Biochimica Et Biophysica Acta-Biomembranes* **1996,** *1279* (2), 169-180.

90. Necas, D.; Klapetek, P., Gwyddion: an open-source software for SPM data analysis. *Central European Journal of Physics* **2012,** *10* (1), 181-188.

91. Schneider, C. A.; Rasband, W. S.; Eliceiri, K. W., NIH Image to ImageJ: 25 years of image analysis. *Nature Methods* **2012,** *9* (7), 671-675.

92. Aizenberg, J.; Black, A. J.; Whitesides, G. M., Control of crystal nucleation by patterned self-assembled monolayers. *Nature* **1999,** *398* (6727), 495-498.

93. Han, Y. J.; Aizenberg, J., Face-selective nucleation of calcite on self-assembled monolayers of alkanethiols: Effect of the parity of the alkyl chain. *Angewandte Chemie-International Edition* **2003,** *42* (31), 3668-3670.

94. Pokroy, B.; Aizenberg, J., Calcite shape modulation through the lattice mismatch between the self-assembled monolayer template and the nucleated crystal face. *Crystengcomm* **2007,** *9* (12), 1219-1225.

95. Kiessling, L. L.; Pohl, N. L., Strength in numbers: Non-natural polyvalent carbohydrate derivatives. *Chemistry & Biology* **1996,** *3* (2), 71-77.

96. Gestwicki, J. E.; Cairo, C. W.; Strong, L. E.; Oetjen, K. A.; Kiessling, L. L., Influencing receptor-ligand binding mechanisms with multivalent ligand architecture. *Journal of the American Chemical Society* **2002,** *124* (50), 14922-14933.

97. Kiessling, L. L.; Gestwicki, J. E.; Strong, L. E., Synthetic multivalent ligands as probes of signal transduction. *Angewandte Chemie-International Edition* **2006,** *45* (15), 2348-2368.

98. Kumar, A.; Whitesides, G. M., Features Of Gold Having Micrometer To Centimeter Dimensions Can Be Formed Through A Combination Of Stamping With An Elastomeric Stamp And An Alkanethiol Ink Followed By Chemical Etching. *Applied Physics Letters* **1993,** *63* (14), 2002-2004.

99. Kumar, A.; Biebuyck, H. A.; Whitesides, G. M., Patterning Self-Assembled Monolayers - Applications In Materials Science. *Langmuir* **1994,** *10* (5), 1498-1511.

100. Perl, A.; Reinhoudt, D. N.; Huskens, J., Microcontact Printing: Limitations and Achievements. *Advanced Materials* **2009,** *21* (22), 2257-2268.

101. Han, X.; Zheng, Y.; Munro, C. J.; Ji, Y.; Braunschweig, A. B., Carbohydrate nanotechnology: hierarchical assembly using nature's other information carrying biopolymers. *Current Opinion in Biotechnology* **2015,** *34*, 41-47.

102. Park, S.; Gildersleeve, J. C.; Blixt, O.; Shin, I., Carbohydrate microarrays. *Chemical Society Reviews* **2013,** *42* (10), 4310-4326.

103. Kiessling, L. L., Chemistry-driven glycoscience. *Bioorganic & Medicinal Chemistry* **2018,** *26* (19), 5229-5238.

104. Groszek, A. J., Preferential Adsorption Of Normal Hydrocarbons On Cast Iron. *Nature* **1962,** *196* (4854), 531-&.

105. Groszek, A. J., Preferential Adsorption Of Long-Chain Normal Paraffins On Mos2 Ws2 + Graphite From N-Heptane. *Nature* **1964,** *204* (495), 680-&.

106. Rabe, J. P.; Buchholz, S., Commensurability And Mobility In 2-Dimensional Molecular-Patterns On Graphite. *Science* **1991,** *253* (5018), 424-427.

107. Bang, J. J.; Porter, A. G.; Davis, T. C.; Hayes, T. R.; Claridge, S. A., Spatially Controlled Noncovalent Functionalization of 2D Materials Based on Molecular Architecture. *Langmuir* **2018,** *34* (19), 5454-5463.

108. Workman, R. K.; Schmidt, A. M.; Manne, S., Detection of a diffusive two-dimensional gas of amphiphiles by lateral force microscopy. *Langmuir* **2003,** *19* (8), 3248-3253.

109. Workman, R. K.; Manne, S., Molecular transfer and transport in noncovalent microcontact printing. *Langmuir* **2004,** *20* (3), 805-815.

110. Hovis, J. S.; Boxer, S. G., Patterning and composition arrays of supported lipid bilayers by microcontact printing. *Langmuir* **2001,** *17* (11), 3400-3405.

111. Russell, S. R.; Davis, T. C.; Bang, J. J.; Claridge, S. A., Spectroscopic Metrics for Alkyl Chain Ordering in Lying-Down Noncovalent Monolayers of Diynoic Acids on Graphene. *Chemistry of Materials* **2018,** *30* (8), 2506-2514.

112. Wang, Z. X.; Volinsky, A. A.; Gallant, N. D., Crosslinking Effect on Polydimethylsiloxane Elastic Modulus Measured by Custom-Built Compression Instrument. *Journal of Applied Polymer Science* **2014,** *131* (22).

113. Xia, Y. N.; Whitesides, G. M., Use Of Controlled Reactive Spreading Of Liquid Alkanethiol On The Surface Of Gold To Modify The Size Of Features Produced By Microcontact Printing. *Journal of the American Chemical Society* **1995,** *117* (11), 3274-3275.

114. Sharpe, R. B. A.; Burdinski, D.; Huskens, J.; Zandvliet, H. J. W.; Reinhoudt, D. N.; Poelsema, B., Spreading of 16-mercaptohexadecanoic acid in microcontact printing. *Langmuir* **2004,** *20* (20), 8646-8651.

115. Libioulle, L.; Bietsch, A.; Schmid, H.; Michel, B.; Delamarche, E., Contact-inking stamps for microcontact printing of Alkanethiols on gold. *Langmuir* **1999,** *15* (2), 300-304.

116. Graham, D. J.; Price, D. D.; Ratner, B. D., Solution assembled and microcontact printed monolayers of dodecanethiol on gold: A multivariate exploration of chemistry and contamination. *Langmuir* **2002,** *18* (5), 1518-1527.

117. Sharpe, R. B. A.; Burdinski, D.; van der Marel, C.; Jansen, J. A. J.; Huskens, J.; Zandvliet, H. J. W.; Reinhoudt, D. N.; Poelsema, B., Ink dependence of poly(dimethylsiloxane) contamination in microcontact printing. *Langmuir* **2006,** *22* (13), 5945-5951.

118. Delamarche, E.; Schmid, H.; Bietsch, A.; Larsen, N. B.; Rothuizen, H.; Michel, B.; Biebuyck, H., Transport mechanisms of alkanethiols during microcontact printing on gold. *Journal of Physical Chemistry B* **1998,** *102* (18), 3324-3334.

119. Rao, C. N. R.; Nag, A., Inorganic Analogues of Graphene. *European Journal of Inorganic Chemistry* **2010,** (27), 4244-4250.

120. de la Rosa, C. J. L.; Phillipson, R.; Teyssandier, J.; Adisoejoso, J.; Balaji, Y.; Huyghebaert, C.; Radu, I.; Heyns, M.; De Feyter, S.; De Gendt, S., Molecular doping of MoS2 transistors by self-assembled oleylamine networks. *Applied Physics Letters* **2016,** *109* (25), 4.

121. Cincotti, S.; Rabe, J. P., Self-Assembled Alkane Monolayers On Mose2 And Mos2. *Applied Physics Letters* **1993,** *62* (26), 3531-3533.

122. Giancarlo, L. C.; Fang, H. B.; Rubin, S. M.; Bront, A. A.; Flynn, G. W., Influence of the substrate on order and image contrast for physisorbed, self-assembled molecular monolayers: STM studies of functionalized hydrocarbons on graphite and MoS2. *Journal of Physical Chemistry B* **1998,** *102* (50), 10255-10263.

123. Wang, J. H.; Yu, H. D.; Zhou, X.; Liu, X. Z.; Zhang, R. J.; Lu, Z. X.; Zheng, J. Y.; Gu, L.; Liu, K. H.; Wang, D.; Jiao, L. Y., Probing the crystallographic orientation of two-dimensional atomic crystals with supramolecular self-assembly. *Nature Communications* **2017,** *8*, 8.

124. Fu, C.; Orgiu, E.; Perepichka, D. F., Face-on vs. edge-on: tuning the structure of tetrathiafulvalene monolayers with solvent. *Journal of Materials Chemistry C* **2018,** *6* (14), 3787-3791.

125. Fang, Y.; Cibian, M.; Hanan, G. S.; Perepichka, D. F.; De Feyter, S.; Cuccia, L. A.; Ivasenko, O., Alkyl chain length effects on double-deck assembly at a liquid/solid interface. *Nanoscale* **2018,** *10* (31), 14993-15002.

126. Sagiv, J., organized monolayers by adsorption .1. Formation and structure of oleophobic mixed monolayers on solid-surfaces. *J. Am. Chem. Soc.* **1980,** *102* (1).

127. Schreiber, F., Structure and growth of self-assembling monolayers. *Prog. Surf. Sci.* **2000,** *65* (5-8), 151-256.

128. Rabe, J. P.; Buchholz, S., Commensurability and Mobility in 2-Dimensional Molecular Patterns on Graphite. *Science* **1991,** *253* (5018), 424-427.

129. Hoeppener, S.; Chi, L. F.; Fuchs, H., Formation of Au-55 strands on a molecular template at the solid-liquid interface. *Nano Lett.* **2002,** *2* (5), 459-463.

130. Geng, Y. F.; Liu, M. Q.; Xue, J. D.; Xu, P.; Wang, Y. F.; Shu, L. J.; Zeng, Q. D.; Wang, C., A template-confined fabrication of controllable gold nanoparticles based on the two-dimensional nanostructure of macrocycles. *Chem. Commun.* **2015,** *51* (31), 6820-6823.

131. Cui, D.; MacLeod, J. M.; Ebrahimi, M.; Perepichka, D. F.; Rosei, F., Solution and air stable host/guest architectures from a single layer covalent organic framework. *Chem. Commun.* **2015,** *51* (92), 16510-16513.

132. Iritani, K.; Tahara, K.; De Feyter, S.; Tobe, Y., Host-Guest Chemistry in Integrated Porous Space Formed by Molecular Self-Assembly at Liquid-Solid Interfaces. *Langmuir* **2017,** *33* (19), 4601-4618.

133. Tahara, K.; Katayama, K.; Blunt, M. O.; Iritani, K.; De Feyter, S.; Tobe, Y., Functionalized Surface-Confined Pores: Guest Binding Directed by Lateral Noncovalent Interactions at the Solid-Liquid Interface. *ACS Nano* **2014,** *8* (8), 8683-8694.

134. Hayes, T. R.; Bang, J. J.; Davis, T. C.; Peterson, C. F.; McMillan, D. G.; Claridge, S. A., Multimicrometer Noncovalent Monolayer Domains on Layered Materials Through Thermally Controlled Langmuir-Schaefer Conversion for Noncovalent 2D Functionalization. *ACS Appl. Mater. Interf.* **2017,** *9*, 36409–36416.

135. Bubeck, C.; Tieke, B.; Wegner, G., Selfsensitization of the Photopolymerization of Diacetylenes Studied in Multilayers. *Ber. Bunsen-Ges.* **1982,** *86*, 495-498.

136. Olmsted, J.; Strand, M., Fluorescence of Polymerized Diacetylene Bilayer Films. *J. Phys. Chem.* **1983,** *87*, 4790-4792.

137. Lécuiller, R.; Berréhar, J.; Lapersonne-Meyer, C.; Schott, M., Dual Resonance Fluorescence of Polydiacetylene Chains Isolated in their Crystalline Monomer Matrix. *Phys. Rev. Lett.* **1998,** *80*, 4068-4071.

138. Davis, T. C.; Russell, S. R.; Claridge, S. A., Edge-on adsorption of multi-chain functional alkanes stabilizes noncovalent monolayers on MoS_2. *Chem. Commun.* **2018,** *54*, 11709-11712.

APPENDIX A: SUPPORTING INFORMATION FOR CHAPTER 2

Hierarchically Patterned Noncovalent Functionalization of 2D Materials by Controlled Langmuir–Schaefer Conversion

SEM images of transferred films of pentacosanoic acid

To examine whether similar principles apply to the Langmuir-Schaefer conversion of non-diyne fatty acids to HOPG, we tested transfer of pentacosanoic acid (PCA) at a subphase temperature of 30 °C and a mean molecular area of 35 $Å^2$/molecule, similar to the conditions utilized to prepare lying-down films with circular vacancies as shown in the Chapter 2. Here, we show SEM images acquired after transfer of PCA to HOPG. In Figure S.A.1a, circular vacancies are visible in the transferred film, shown at higher magnification in Figure S.A.1b. In Figure S.A.1c, an image acquired in the an area surrounding one of the circles reveals the formation of defects in the monolayer, presumably under the electron beam, though these defects are not extended and linear as in the case of the diynoic acids. Bright areas with amorphous edges in Figure S.A.1c may represent nanoscopic areas of standing phase, which could be consistent with the presumably tighter chain packing in Langmuir films of the saturated fatty acid in comparison with unsaturated diynoic acids. Overall, these findings suggest that similar in general.

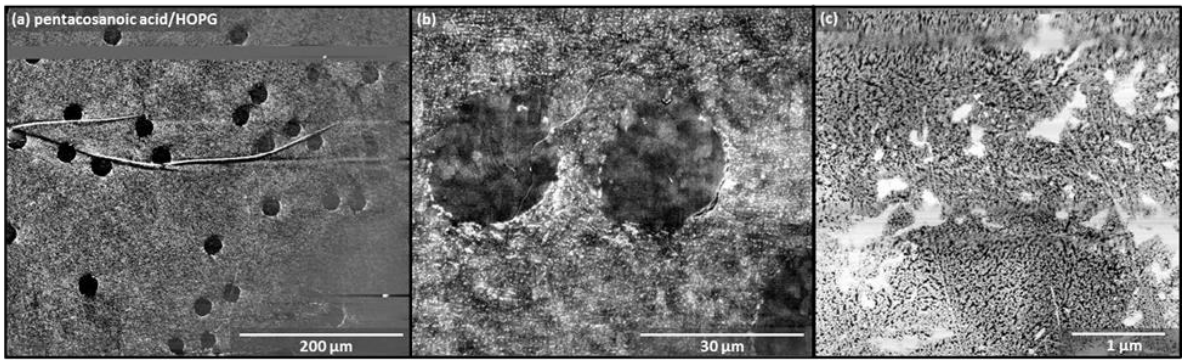

Figure S.A. 1 SEM images of PCA transferred to HOPG from a subphase at 30 °C, and a mean molecular area of 35 $Å^2$/molecule. (a) shows a wide-field image with circular vacancies, two of which are shown at larger magnification in (b). (c) is taken from an area surrounding a circle. considerations are important in the LS conversion of non-polymerizable amphiphiles, and that SEM imaging can be carried out to examine transfer efficiency and morphology, though posttransfer lamellar orientation is less evident due to the lack of polymerization-induced cracking defects.

SEM images of circular patterns of lying-down monolayers transferred from Langmuir films of PCDA at 30 °C

Figure S.A.2 shows SEM images acquired from PCDA films assembled at subphase temperatures of 30 °C, and transferred at (a) 30 $Å^2$/molecule and (b) 40 $Å^2$/molecule, demonstrating the capability to transfer similar molecular structures across a range of mean molecular areas.

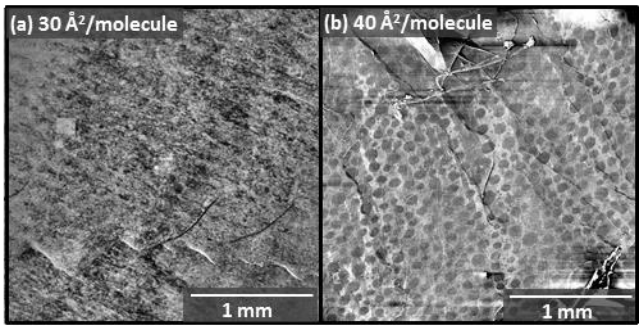

Figure S.A. 2. SEM images of PCDA transferred to HOPG from a subphase at 30 °C, with Langmuir film mean molecular areas of (a) 30 $Å^2$/molecule and (b) 40 $Å^2$/molecule.

Comparison of SEM images of bare HOPG and HOPG functionalized with PCDA

Freshly cleaved HOPG was characterized by SEM to enable contrast comparisons between functionalized and bare HOPG substrates. In Figure S.A.3, images of bare HOPG are shown in the left column (Figure S.A.3a–c), while the right column (Figure S.A.3d–f) shows images of HOPG functionalized with a film of 10,12-PCDA transferred at a mean molecular area of 30 $Å^2$/molecule and subphase temperature of 20 °C. Three comparison points are shown: ~550 μm (Figure S.A.3a,d), ~75 μm (Figure S3.A.b,e), and ~35 μm (Figure S.A.3c,f). On bare HOPG, differences in contrast are evident at step edges and regions in which the graphite is tilted or wrinkled. Boundaries between graphite grains appear as low-contrast (fuzzy) features (Figure S.A.3c), which cannot be sharpened, unlike domain boundaries on PCDA-functionalized HOPG (Figure S.A.3f).

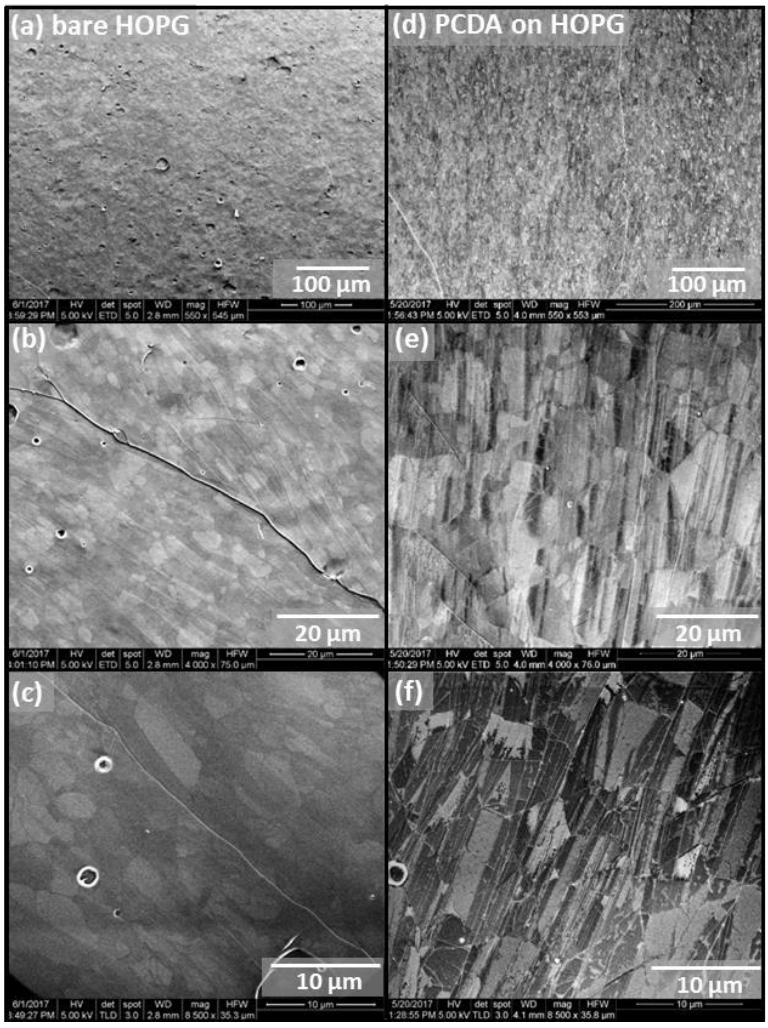

Figure S.A. 3. Comparison of SEM images of bare HOPG (a–c) and HOPG functionalized with PCDA transferred at 20 °C and 30 $Å^2$/molecule (d–f).

AFM images of standing phase and multilayer PCDA transferred to HOPG

To examine topographic heights in standing phase and multilayer areas of molecular films transferred to HOPG at relatively low mean molecular areas, we acquired line scans from AFM topography images. Figure S.A.4 shows two AFM images acquired near the edge of multilayered areas. Line scans over the shortest topographic features visible (insets in images below) reveal topographic heights of ~3 nm, with greater topographic heights for the areas that appear brighter. Full height scales are 17 nm for the image on the left and 14 nm for the image on the right.

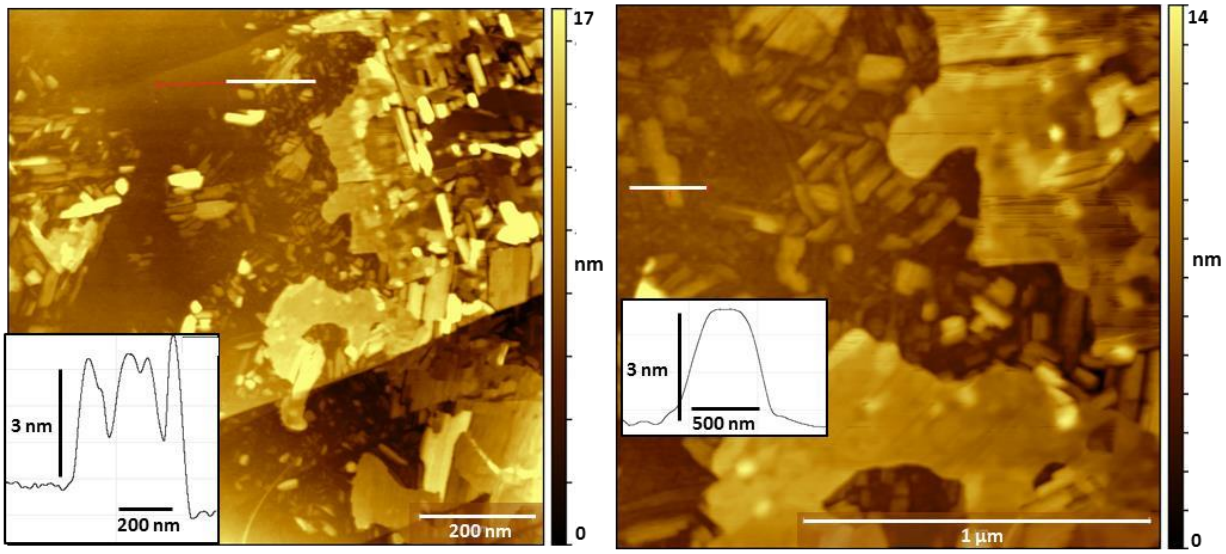

Figure S.A. 4. AFM topography image of multilayer area of PCDA film transferred from PCDA Langmuir films with a subphase temperature of 20 °C and mean molecular area 20 $Å^2$/molecule.

SEM images of transfer near collapse point

When transfer is carried out at elevated surface pressures prior to the collapse point (*i.e.* at conditions similar to those that would typically be used to transfer standing phases to other types of substrates), regions of both standing phase and lying-down phases are transferred (Figure S.A.5).

In pre-collapse BAM images (Figure S.A.5a), platelike features are visible, similar to the intermediate-intensity features visible in post-collapse BAM images (Figure 2.7). Standing phase regions (which are more strongly insulating, and appear white in SEM images below) have curved domain edges visible at larger scales in SEM (Figure S.A.5b) with transfer of lying-down phases with geometric edges in epitaxy with the hexagonal substrate in surrounding regions. Higher-resolution SEM images of the boundary between the two regions (Figure S.A.5c) reveal what appears to be a boundary region with narrow rectangular regions of standing phase.

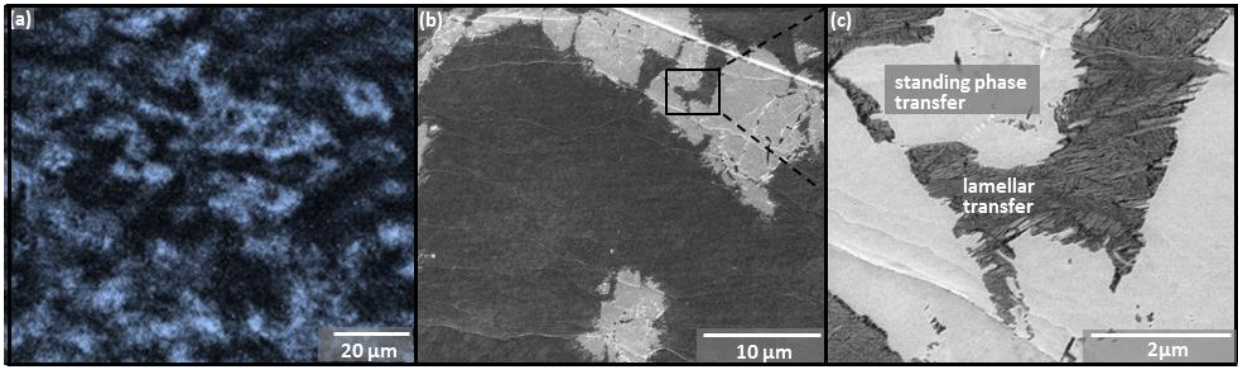

Figure S.A. 5. SEM images of PCDA transfer near collapse point (14 mN/m, 20 °C subphase).

Image segmentation to estimate molecular surface coverage

Images were digitally segmented in order to estimate surface coverage of each class of domain tabulated in Chaper 2. Images were processed using Gwyddion SPM image analysis software and Adobe Photoshop to perform plane flattening and contrast/brightness adjustment to facilitate subsequent segmentation based on pixel intensity. Segmentation was performed in MATLAB (Figure S.A.6), using digital thresholding to define areas occupied by lamellar domains and dendritic or other amorphous domains. The percentages of pixels with values above and below the threshold were tabulated to assess surface coverage. Because amorphous domains restructure under the electron beam to occupy a smaller area of the surface, the total area occupied by the domains prior to thermal rearrangement was estimated based on contours around the restructured area, compared when possible to larger-scale images, in which electron flux is lower and minimal restructuring is observed. Regions of each image occupied by different domain types were then false colored to facilitate visual distinction between classes of surface coverage.

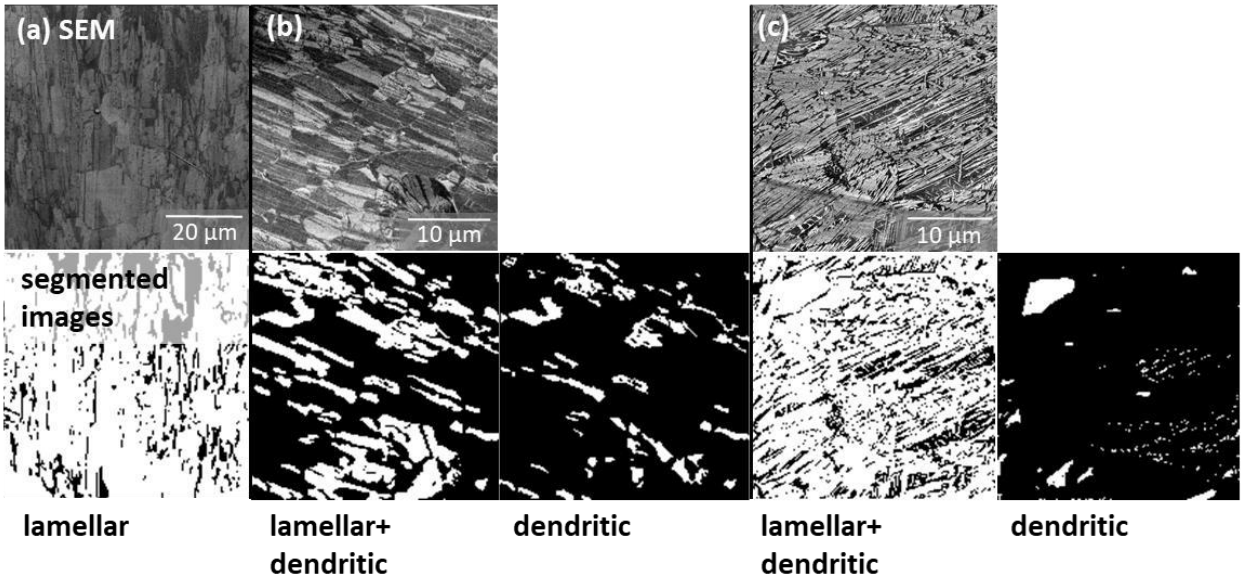

Figure S.A. 6. Example MATLAB image segmentation for molecular domain coverage calculations. (a) SEM image displaying lamellar domains and vacancies (top), and segmented image (bottom). (b) SEM image displaying lamellar and dendritic domains, with segmented image highlighting both lamellar and dendritic domains (bottom left) and dendritic domains only (bottom right). (c) SEM image displaying both lamellar and dendritic domains (top), with segmented image highlighting both lamellar and dendritic domains (bottom left) and dendritic domains only (bottom right).

Molecular domain size measurements

Images were processed using Gwyddion image analysis software to perform plane flattening, contrast/brightness adjustment, and false coloring to facilitate identification of domain boundaries and other surface features. Using Gwyddion, domain lengths and widths were first measured, then subsequently tabulated and multiplied to obtain the area of each domain. This process was repeated for each domain present in the image; domains intersecting the image edge were excluded. Lamellar domain areas were averaged at a minimum of 3 locations across each substrate and average of 2 substrates per set of transfer conditions. Figure S.A.7 shows a pair of AFM images with domain lengths and widths highlighted in red.

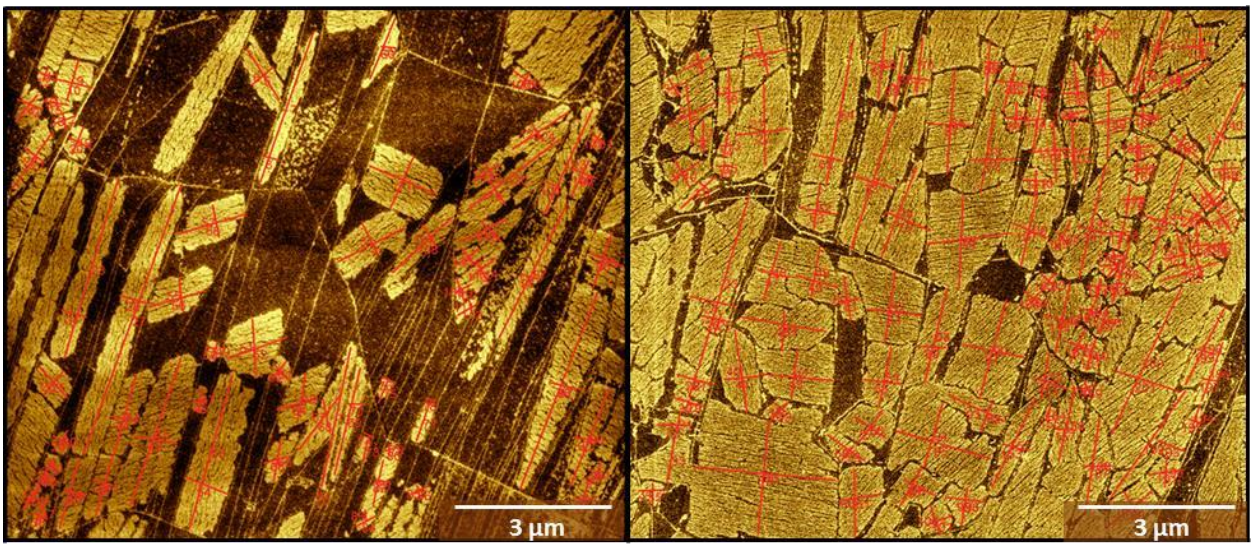

Figure S.A. 7. AFM images showing example length and width measurements (red lines highlighted crossing each domain) utilized in calculations of average molecular domain areas.

Cracking density measurements

Images were processed using Gwyddion image analysis software to perform plane flattening, contrast/brightness adjustment, and false coloring to facilitate identification of polymerization defect cracks and other surface features. Using Gwyddion, line profiles were measured perpendicular to the axis of cracking, with a line width of 17 pixels. Cracking density was calculated by taking the quotient of the number of cracks between the lowest points of two distant cracks and the distance between those cracks. Figure S.A.8 shows an example SEM image containing cracked domains. Pixels extracted for the line scan are highlighted in red in the top center domain in Figure S.A.8a. The line profile of pixel brightness in highlighted pixels is shown in Figure S.A.8b. Bright defect in upper right is an area previously imaged at higher resolution.

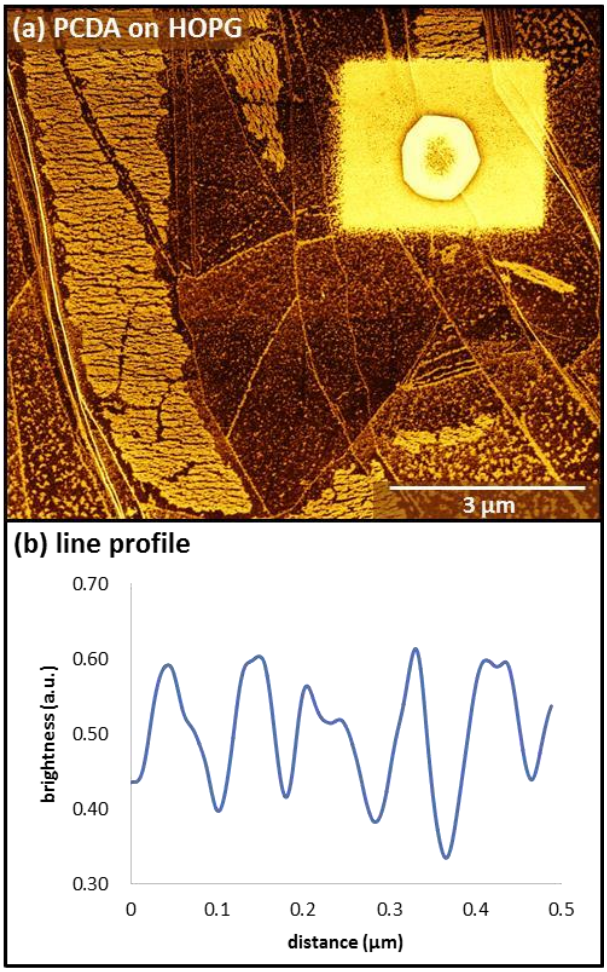

Figure S.A. 8. Example line scan for calculation of cracking density. (a) SEM image of PCDA on HOPG, with cracked domain structures. Red line in domain at top center is set of pixels from which line scan was extracted. (b) Line profile of pixel brightness across line scan highlighted in red in (a).

Shorter LS transfer times

Throughout Chapter 2, we have utilized a 4-minute transfer time, consistent with conditions we have used for previous work. However, it is also possible to perform similar transfers at shorter timepoints. Figure S.A.9 demonstrates a transfer in which the HOPG substrate was maintained in contact with the molecular film on the subphase for 30 seconds. At the end of the 30-s transfer time, the motor on the automated dipper attachment was started to lift the HOPG out of contact with the subphase. Figure S.A.9a shows a large-scale SEM image illustrating the presence of circles; Figure S.A.9b shows lamellar domains and vacancies near the edge of one of the circles.

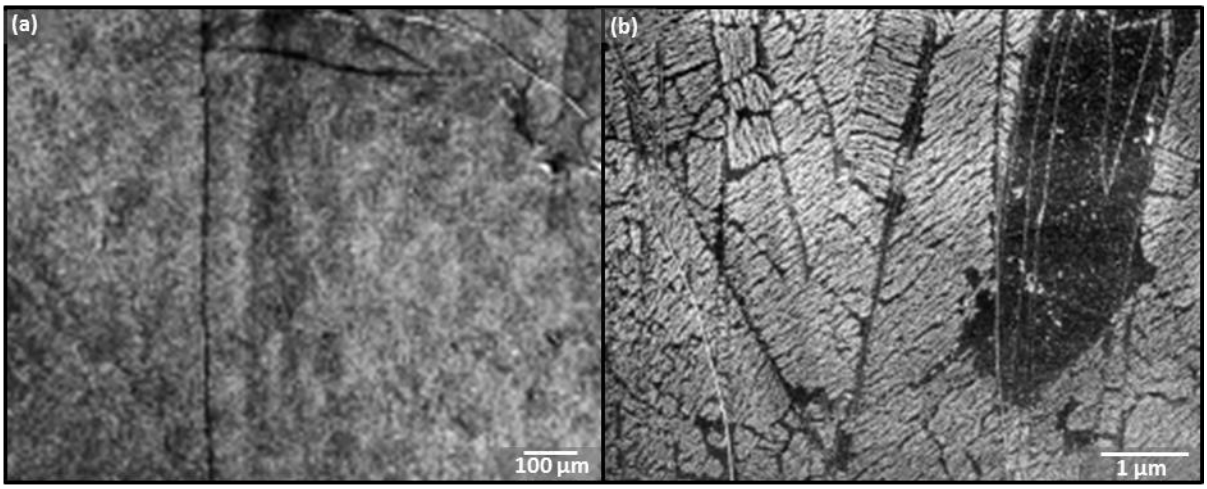

Figure S.A. 9. (a) Large-scale SEM image showing formation of circular patterns of PCDA on HOPG after 30-second transfer time. (b) High-resolution SEM image showing lamellar domains and vacancies near the edge of one of the circles in (a).

APPENDIX B: SUPPORTING INFORMATION FOR CHAPTER 3

Hierarchically Patterned Striped Phases of Polymerized Lipids: Toward Controlled Carbohydrate Presentation at Interfaces

Experimental Methods

Materials.

Chloroform (≥99.5 % purity), undec-10-ynoic acid (95 %), dec-1-yne (98 %), iodine (99.8 %), copper iodide (99.5 %), morpholine (99 %), potassium hydroxide, hydroxylamine hydrochloride (98 %), ethylamine (70 % (*v/v*) solution in water), sulfuric acid (95.0–98.0 %), sodium thiosulfate, and sodium sulfate, were all purchased from Sigma Aldrich (St. Louis, MO) and used as received. Absolute ethanol (100 % purity) was purchased from Decon Laboratories, Inc. (King of Prussia, PA) and used as received. Methanol, diethyl ether (anhydrous), hexanes, THF, and toluene were purchased from Fisher Scientific (Hampton, NH) and used as received. Silica gel was purchased from Macherey-Nagel (Bethlehem, PA) and used as received. 1,2-Bis(10,12-tricosadiynoyl)-*sn*-glycero-3-phosphoethanolamine (diyne PE, >99.0 % purity), 1,2bis(10,12-tricosadiynoyl)-*sn*-glycero-3-phosphocholine (diyne PC, >99.0 % purity), and 1,2-distearoyl-*sn*-glycero-3phosphoinositol (ammonium salt) (PI, >99.0 % purity) were purchased from Avanti Polar Lipids (Alabaster, AL) and used as received. Commercially available fatty acids 10,12-tricosadiynoic acid (TCDA, ≥ 98.0 % purity) and 10,12pentacosadiynoic acid (PCDA, ≥ 97.0% purity) were purchased from Sigma-Aldrich (St. Louis, MO), and 10,12nonacosadiynoic (NCDA, >97.0% purity) was purchased from Tokyo Chemical Industry Co., Ltd. (Montgomeryville, PA). All fatty acids were dissolved in chloroform and filtered through 0.2-μm syringe filters to eliminate oligomers prior to use. For preparation of the poly(dimethylsiloxane) (PDMS) elastomer stamps, SYLGARD 184 silicone elastomer kits containing base and curing (crosslinking) agent were purchased from Dow Chemical Company (Midland, MI). When water was experimentally required, Milli-Q water (≥18.2 MΩ·cm resistivity) was used. Ultrahigh purity nitrogen (UHP N_2, 99.999 % purity) was purchased from Indiana Oxygen Company (Indianapolis, IN). Lipids were deposited on 1 cm × 1 cm highly oriented pyrolytic graphite (HOPG) substrates (MicroMasch, Watsonville, CA), which were freshly cleaved immediately prior to transfer. All initial steps in the transfer process were carried out under UV-filtered light to prevent

polymerization in solution. PELCO conductive liquid silver paint, standard SEM pin stub mounts, and double-coated carbon conductive tape were purchased from Ted Pella, Inc. (Redding, CA). Silicon wafers photolithographically patterned with arrays of 5 μm × 5 μm × 5 μm recessed cubes with a 10 μm pitch were provided by Prof. Wei-Ssu Liao (National Taiwan University).

General procedure for synthesis of 1-iododec-1-yne

Synthesis was carried out using a modification of previously published procedures,[1] described briefly here. A solution of morpholine (44 mmol) in toluene (34.8 mL) was treated with iodine (6.16 mmol), shielded from light and stirred for 1 h at 45 °C. A solution of dec-1-yne (4.4 mmol) in toluene (3.48 mL) was then added and the reaction mixture stirred continuously at 45 °C for 1 h. The reaction mixture was cooled to room temperature and filtered to remove the iodomorpholine salt. The filtrate was poured over a mixture of diethyl ether (50 mL) and a saturated aqueous solution of $Na_2S_2O_3$ (50 mL) and shaken until the organic layer was colorless. The organic layer was separated, washed again with a saturated aqueous solution of $Na_2S_2O_3$ (50 mL), dried over anhydrous Na_2SO_4, filtered, concentrated, and purified via column chromatography, with hexane as an eluent, to afford a 1-iododec-1-yne as a colorless oil (typical yield ~70 %).

Synthesis of 10,12-henicosadiynoic acid (HCDA)

Synthesis was carried out using a modification of published procedure,[1-2] described briefly here. Undec-10-ynoic acid (1.9 mmol) was dissolved in THF (14 mL) and CuI (0.43 mmol) was dissolved in 70% (*v/v*) ethylamine in water (14 mL). The undec-10-ynoic acid solution and the CuI solution were combined with ethanol (14 mL). Subsequently, 1 M KOH in water (6 mL) was added to the reaction mixture along with hydroxylamine hydrochloride (0.33 mmol). The reaction was cooled to 0 ˚C. A solution of 1-iododec-1-yne (5.1 mmol) dissolved in THF (10 mL) was then added dropwise, causing a precipitate to form. The reaction was allowed to warm to room temperature and proceed for a further 24 h. If the solution turned blue, additional aliquots of hydroxylamine hydrochloride were added. The reaction was quenched by the addition of a 10% aqueous solution of sulfuric acid to achieve neutral pH (typical required volume ~4 mL). Crude product was extracted with diethyl ether (3 × 50 mL) and then washed with water (3 × 50 mL) and

brine (3 × 50 mL). The organic layer was dried over anhydrous Na_2SO_4, filtered, and the ether was removed by rotary evaporator. The crude product was purified by recrystallization from hexanes to yield a fatty acid with an internal diyne, as a white solid (typical yield ~30 %).

Preparation of PDMS Stamps

Stamps were prepared by mixing SYLGARD 184 silicone elastomer base and curing (crosslinking) agent at the desired ratio (*e.g.* 10:1 *m/m*, or as described in Chapter 3). After the components were thoroughly mixed (approximately 5 min), the mixture was poured onto a photolithographically etched silicon wafer resting in a petri dish. The mixture was then deaerated in a vacuum desiccator until no bubbles remained. Subsequently, the petri dish was placed in an oven to allow the PDMS to cure for 24 h at 60 °C. After curing, crosslinked PDMS was peeled from the silicon wafer and cut to the desired size using a razor blade. PDMS stamps were cleaned by soaking them in Milli-Q water for 1 h, followed by sonication in a 1:1:1 (*v/v/v*) mixture of ethanol, methanol, and Milli-Q water for 30 min. The sonication step is crucial. Following sonication, stamps were placed in an oven for 1 h at 60 °C to allow residual polar solvent mixture to evaporate. Stamps were then soaked in hexanes for 6 h, replacing the hexanes every 2 h. Finally, the stamps were dried for 24 h at 60 °C and placed, pattern side up, in a covered petri dish prior to use. The cleaning procedure was repeated in preparation for each use of the stamp.

Ultraviolet ozone (UVO) plasma processing to increase PDMS stamp hydrophilicity

PDMS stamps hydrophilicity was increased using a Herrick PDC-3XG Plasma Cleaner with an oxygen flow rate of 150 cc/min and the RF level set to high for 60 min, unless otherwise stated in Chapter 3.

Inking of PDMS Stamp

For inking, a cleaned PDMS stamp was first rinsed briefly with ethanol and blown dry with UHP N_2. The patterned surface of the stamp was immersed in a solution of the chosen amphiphile. Solutions of amphiphiles were prepared first at 2.5 mg/mL in either $CHCl_3$ (for phospholipids) or 3:2 (*v:v*) hexane:IPA (for fatty acids). The solution was then dissolved to the desired concentration (stated in Chapter 3) with ethanol. This procedure was followed in order to maintain amphiphile

solubility, while achieving a relatively low concentration of hexanes and $CHCl_3$ in the inking solution, since these solvents are known to swell PDMS and distort features. After 30 s of immersion in the dilute lipid solution in the carrier solvent mixture, the stamp was removed, blown dry with UHP N_2 and placed pattern side up for 1 h at room temperature to allow additional carrier solvent to evaporate from the stamp.

Transfer of amphiphiles from PDMS to HOPG

After inking and subsequent drying for 1 h, the patterned side of the PDMS stamp was brought into contact with a freshly cleaved HOPG substrate, using one of the methods described below. In the 'flat contact' method, the stamp was lowered gently onto the HOPG surface. The PDMS stamp typically wet the HOPG surface; light tapping pressure with tweezers was applied to restore contact if needed. PDMS–HOPG contact was maintained for 30 s (unless otherwise specified) before the stamp was carefully lifted from the surface. In the 'rolled contact' method, the stamp was mounted on a copper cylinder 2.54 cm in diameter, 6.8 cm in length, and 300 g in mass. Double-sided tape was placed around the diameter of the copper cylinder, and the back side of the stamp was affixed to the tape. In one fluid motion (typically lasting approximately 3 s), the stamp was rolled across the surface of a freshly cleaved HOPG substrate. After both 'flat contact' and 'rolled contact' transfers, the functionalized HOPG was placed under a hand-held UV lamp (254 nm, 8 W) for 1 h with ~2 cm between the lamp and the substrate, to induce diyne photopolymerization, stabilizing the transferred molecular layer.

SEM imaging

Molecular layers on HOPG were imaged using a Teneo VS SEM (FEI Company, Hillsboro, OR). Images were acquired at a working distance of ~5 mm using the segmented in-lens T3 detector. A beam current of 3.2 nA was selected for optimal image resolution, utilizing a 32-µm diameter aperture with an accelerating voltage of 5 kV. All substrates were affixed to standard SEM pin stub specimen mounts with double-sided conductive carbon tape. To further enhance substrate–mount conductivity, a small amount of colloidal silver paint (PELCO, Ted Pella, Inc.) was applied along the perimeter of the substrate, providing electrical contact with the underlying pin stub.

Image analysis

Images were processed using Gwyddion scanning probe microscopy data visualization and analysis software[3] and ImageJ analysis software[4] to perform median line corrections, plane flattening, scar artifact removal, and contrast adjustment. Transfer fidelity and domain area measurements were performed using Adobe Photoshop to identify domain boundaries and calculate transfer coverage.

Energy minimization

Software packages Maestro and Macromodel (Schrödinger, Cambridge MA) were used, respectively, to visualize molecular structures and to perform force field minimizations. Models were minimized using the OPLS_2005 force field, with extended cutoffs for Van der Waals, electrostatic, and hydrogen bonding interactions. The dielectric constant of the simulation was set to 80.1. Minimizations were performed using the Polak-Ribiere conjugate gradient (PRCG) algorithm and gradient method with 50000 runs and a convergence threshold of 0.05.

Comparison of PCDA transfer from PDMS stamps with base:crosslinker ratios of 10:5 to 10:1

Because the local surface roughness of HOPG is lower than that of Au substrates commonly used in microcontact printing of alkanethiols, we examined whether this led to differences in PDMS rigidity required for optimal molecular transfer to HOPG. The elastomer base and curing (crosslinking) agent are typically mixed in a 10:1 (*m/m*) ratio for transfer of alkanethiols to Au; here, we prepared PDMS stamps with ratios from 10:5 to 10:1. High crosslinker ratios (*e.g.* 10:5) produce more rigid stamps with high elastic moduli, possibly useful for improving stamping fidelity of small features, given the limited need of the stamp to deform on the fairly flat HOPG substrate. Simultaneously, high curing agent ratios have been observed in other systems to limit the ability of the stamp to absorb molecular ink. Stamps were cleaned as described in the Experimental Methods, and an ink solution of 1.1 mM PCDA in the carrier solvent mixture was applied. Figure S.B.1 shows SEM images of PCDA transferred to HOPG from the three stamps. Stamps prepared with a base:crosslinker ratio of 10:5 (Figure S.B.1a,b) produce a high degree of molecular deposition both inside and outside the contact area. The intermediate 10:2 ratio (Figure S.B.1c,d) produces desirable transfer characteristics: a high degree of striped phase coverage in

the contact area, with limited transfer outside the contact area. In general, stamps prepared at a ratio of 10:1 (Figure S.B.1e,f) resulted in a somewhat increased range of transfer outside the stamp contact area, and in some cases, increased PDMS deposition (black spots) within the contact area. However, overall, both 10:2 and 10:1 base:crosslinker ratios produce reasonable transfer, and in many cases we tested stamps prepared in both ratios, for comparison with common stamp preparation conditions used in the assembly of standing phases on gold.

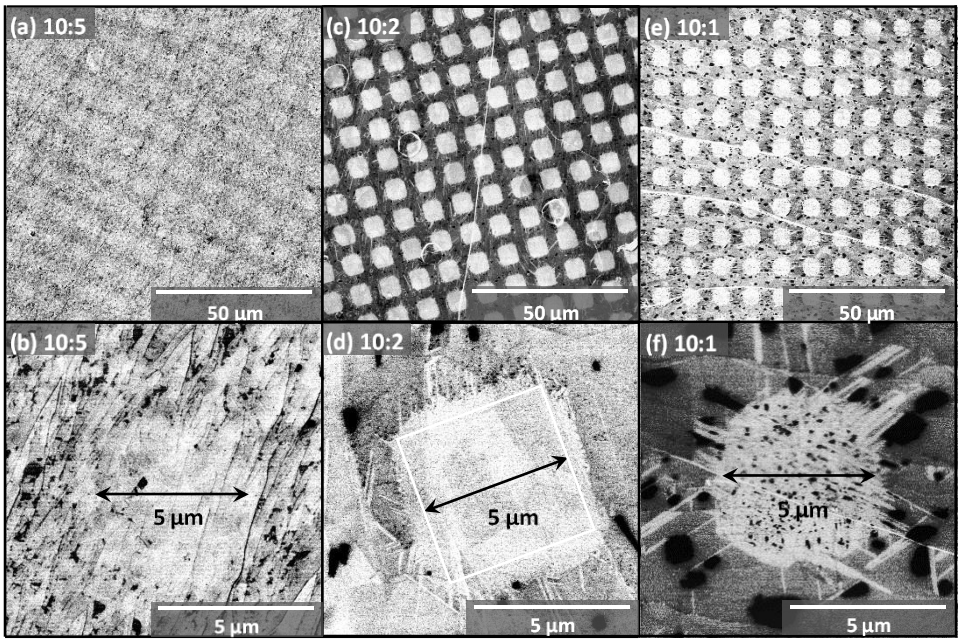

Figure S.B. 1 SEM images of PCDA transferred to HOPG from PDMS stamps prepared at elastomer base:crosslinker ratios of (a,b) 10:5, (c,d) 10:2, and (e,f) 10:1.

Representative SEM images for microcontact transfer of lipids to HOPG at concentrations from 2.1 – 0.045 mM

Previously, ink concentration has been found to be an important factor in producing high density molecular coverage in the stamp contact area, while limiting transfer outside the contact area, with concentrations in the range of 1–10 mM producing optimal transfer for standing phases, depending on the structure of the molecular ink. In lying-down striped phases, molecular footprints are much larger than for similar molecules assembled in a standing orientation (*e.g.*, 154 $Å^2$ for PCDA in a lying-down phase *vs.* ~25 $Å^2$ when assembled as a standing phase), requiring, in the case of PCDA, ~1/6 as many molecules to transfer per unit surface area. Figure S.B.2 illustrates

SEM images of HOPG substrates that have been exposed to PDMS stamps carrying PCDA in carrier solvent at concentrations ranging from 2.1 to 0.045 mM, using the conditions described above. Patterns of squares representing deposited PCDA appear in higher contrast due to enhanced electron scattering relative to the conductive HOPG substrate, in agreement with previous SEM images acquired from PCDA monolayers assembled through LS transfer.[5-6] Higher-resolution SEM imaging of a single contact area at each concentration (Figure 3.3b,d,f,h) illustrates that at 1.1 mM, the entire contact area is functionalized with PCDA, with a narrow band of continuously functionalized surface up to 600 nm outside the contact area, and a low fractional coverage of long narrow molecular domains between contact areas. At 0.045 mM PCDA in the ink solution (Figure S.B.2g,h), the contact area is only partially functionalized, although individual domains are larger (typical length 1–2 μm) than those observed for transfer at 1.1 mM PCDA, which is reasonable given that lower monomer concentrations result in fewer but larger molecular islands in the submonolayer island nucleation and growth model. For this transfer condition, substantial areas of PDMS deposition (black spots) are also observed in the contact area. Even at 2.1 mM PCDA in the transfer solution, some PDMS deposition can be observed; the amount of PDMS impurity deposited can vary from transfer to transfer. Overall, 2.1 mM PCDA produced the greatest extent of PCDA transfer outside the contact area. Based on these findings, we utilized amphiphile ink solutions prepared with 1.1 mM alkyl chain concentrations (*i.e.*, 1.1 mM PCDA; 0.5 mM diyne PC), unless otherwise described in Chapter 3.

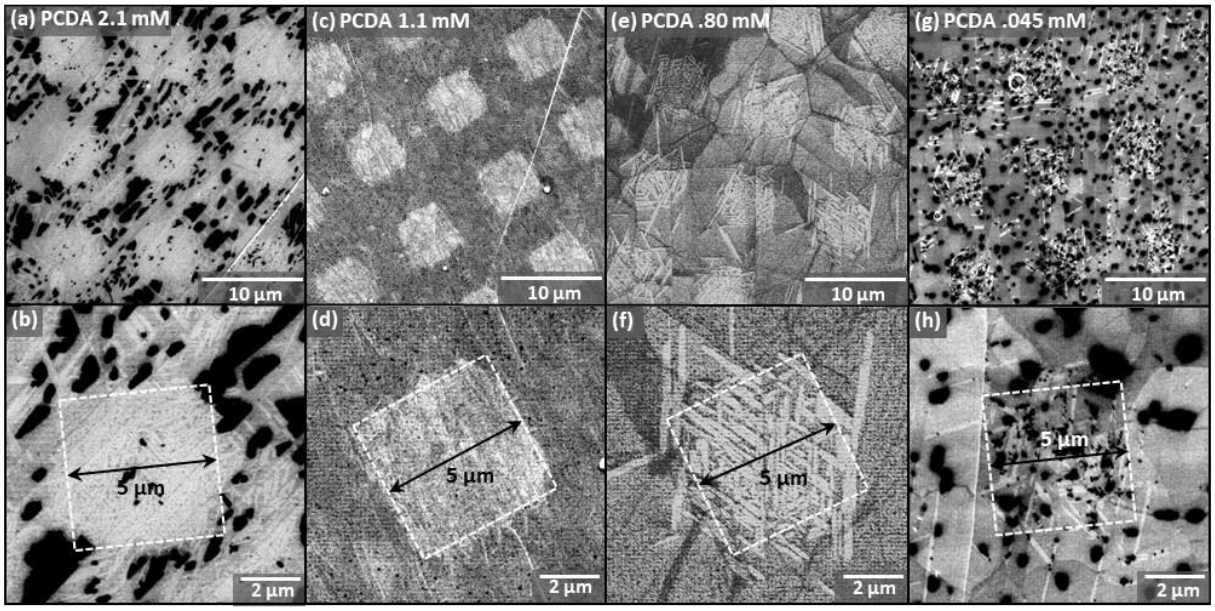

Figure S.B. 2. SEM images of PCDA transferred to HOPG from solutions containing (a,b) 2.1 mM PCDA, (c,d) 1.1 mM PCDA, (e,f) 0.80 mM and (g,h) 0.045 mM PCDA in ethanol.

Comparisons of AFM and SEM images to examine orientation of transferred molecules

Because molecular domains produced by microcontact printing are relatively small (edge lengths *ca.* 100 nm), we utilized AFM imaging in addition to SEM imaging to characterize transfer, in order to examine the density of molecular domains produced under different transfer conditions. Figure S.B.3 compares SEM and AFM micrographs of microcontact printed squares of PCDA produced using 1.1 mM PCDA in ethanol. We have previously observed that striped monolayers of diacetylene amphiphiles can exhibit cracking defects following polymerization, which are emphasized in SEM images (presumably due to further polymerization and restructuring under the electron beam).[5] The presence of these defects makes it possible to infer the directionality of molecular rows within ordered domains. Cracking defects of this type were observed in SEM images of diynoic acids deposited by microcontact printing, pointing to the assembly of ordered lamellar phases; AFM imaging was additionally utilized to quantify the presence of any areas of standing phase molecules based on topographic height (up to 3 nm for standing phases; 0.5–1.0 nm for typical lying down phases, dependent upon molecular orientation).

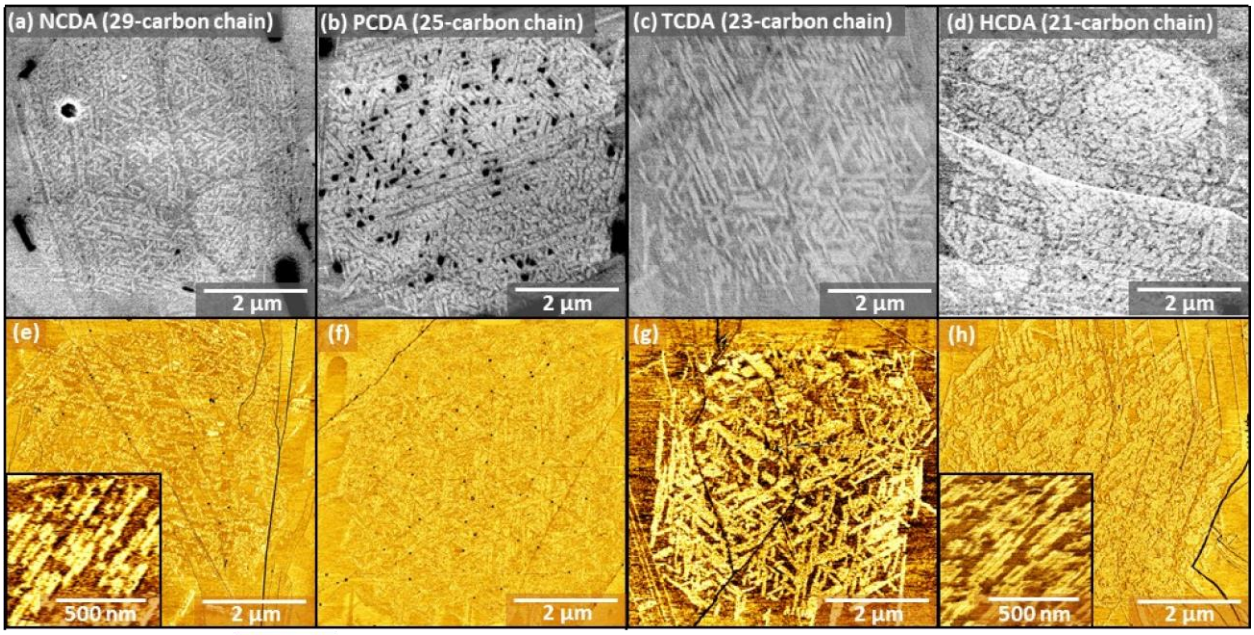

Figure S.B. 3. SEM and AFM images of microcontact printed diynoic acids with chains 29 to 21 carbons in length: (a,e) 10,12nonacosadiynoic acid (NCDA, 29-carbon chain); (b,f) 10,12-pentacosadiynoic acid (PCDA, 25-carbon chain); (c,g) 10,12tricosadiynoic acid (TCDA, 23-carbon chain); (d,h) 10,12-henicosadiynoic acid (HCDA, 21-carbon chain).

Figure S.B. 4 shows example SEM and AFM images of phospholipids deposited on HOPG by microcontact printing, to illustrate the distinction between standing and lying-down phases. Diyne PE was deposited using a flat contact geometry, with a contact time of 30 s; diyne PC was deposited utilizing rolled contact. Both phospholipids were deposited from a 0.55 mM transfer solution. The bright contrast in the SEM images of diyne PE (Figure S.B.4a,b) is characteristic of amphiphiles assembled in a standing phase, and is consistent with height profiles observed in AFM topography images. Diyne PC, deposited utilizing the rolled contact geometry, exhibits primarily ordered striped phases in the stamp contact areas (see Chapter 3 for diyne PC images).

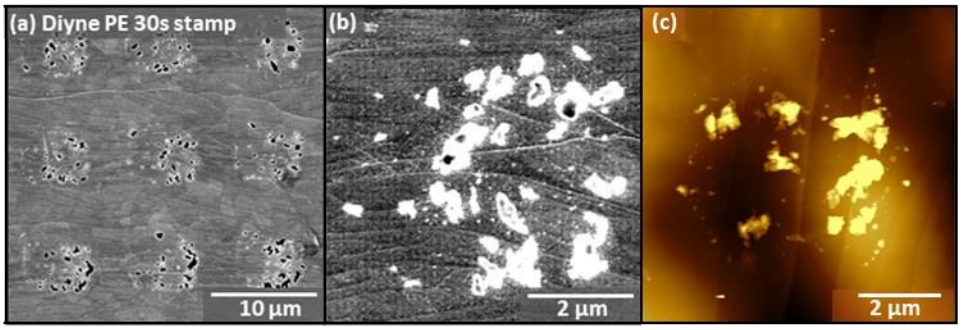

Figure S.B. 4. (a,b) SEM and (c) AFM images of diyne PE transferred to HOPG using a conventional flat stamping geometry, illustrating transfer of standing phase.

Comparison of HOPG surfaces brought into contact with un-inked PDMS stamps prepared at elastomer base:crosslinker ratios of 10:5 to 10:1

For optimizing the delivery of amphiphiles to the substrate, stamps with a range of base:crosslinker ratios (10:5 to 10:1) (*m/m*) were examined. Figure S.B.5 compares the transfer of PDMS impurities. Stamps were exposed to just the solvent components of the ink solution and allowed to dry as described in the Experimental Methods. Areas of dark contrast in SEM images of substrates prepared in this way (such as those in Figure S.B.5) were consistent with those observed following transfer of single-chain and dual-chain amphiphiles. The extent of impurity transfer varied; there was no observed correlation with base:crosslinker ratio. Figure S.B.6 shows AFM phase micrographs of substrates exposed to 1.1 mM PCDA during transfer and illustrates the deposition of PDMS on the HOPG surface.

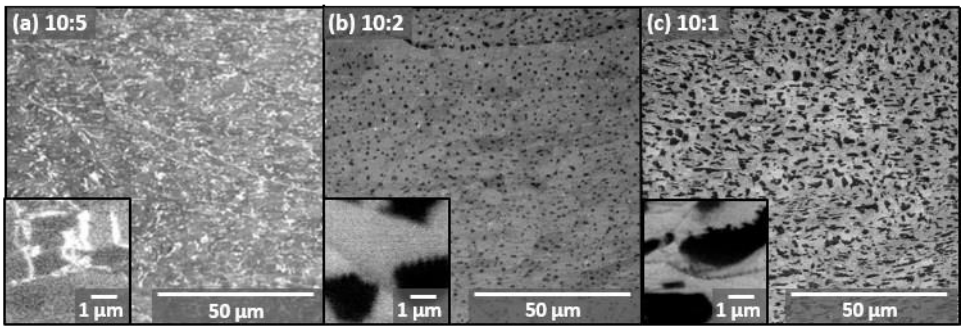

Figure S.B. 5. SEM images of HOPG placed in contact with PDMS stamps prepared at (a) 10:5, (b) 10:2, and (c) 10:1 ratios of elastomer base to curing agent and exposed to solvent only.

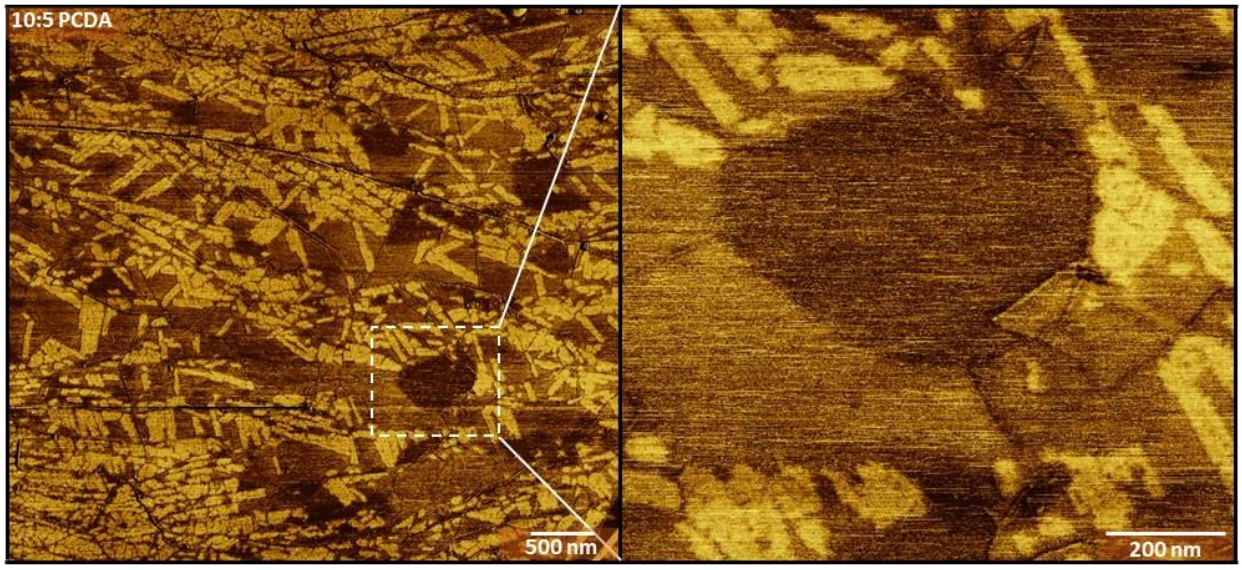

Figure S.B. 6. AFM images of PCDA transferred at 1.1 mM concentration in the ink solution, with a stamp prepared at 10:5 base:crosslinker ratio, resulting in transfer of both striped phase PCDA domains (light regions), and PDMS impurities (dark regions).

Representative images of 10:1 base:crosslinker ratio of 0.5 mM diyne PC

Chapter 3 shows representative images of diyne PC transferred from PDMS stamps prepared at a 10:2 base:crosslinker ratio. Figure S.B.7 shows representative images of diyne PC transferred from stamps prepared at a 10:1 base:crosslinker ratio; similar images were used to calculate domain number densities and diffusion distances.

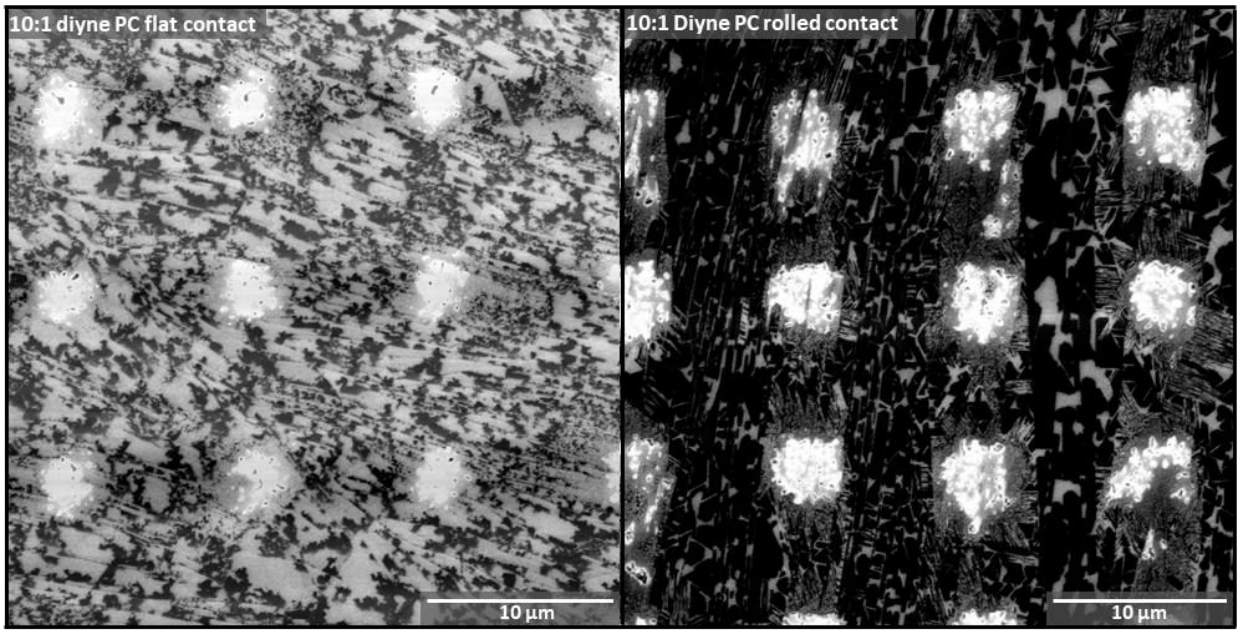

Figure S.B. 7. SEM images of HOPG after rolled and flat contact transfer of diyne PC.

Image segmentation and analysis examples

Figure S.B.8 illustrates how manual image segmentation was performed to compare the assembly of striped phases and standing phases for the tested molecules (*e.g.* PCDA, diyne PE) using transfer conditions described in Chapter 3 and Experimental Methods. The figure illustrates an SEM image of diyne PC transferred to HOPG using a PDMS stamp prepared at a 10:1 base:crosslinker ratio, using rolled transfer. Striped phases can typically be identified based on rectangular domain geometries with linear edges, and/or the presence of long linear defects within the domain that appear during SEM imaging. The percent of the transfer resulting in striped phase domains is calculated by taking the difference of the area of the standing phase (Figure S.B.8c) from the total area occupied by the lipids (Figure S.B.8b). This gives the area of striped phase, which can then be divided by the total lipid-functionalized area to give the percentage of striped phase coverage. The diffusion distance was calculated by taking the total area occupied by the lipid (Figure S.B.8b) and subtracting the theoretical contact area (25 μm^2). This difference is the overfill (or underfill), which can then be used to calculate the diffusion distance.

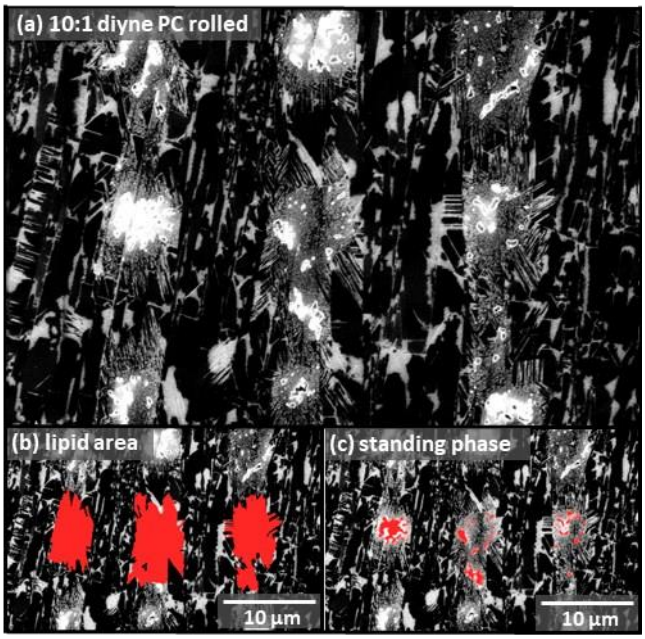

Figure S.B. 8. Sample SEM images showing segmentation (red highlighted areas) utilized for calculations of % striped phase (*vs.* standing phase) molecular transfer.

Molecular domains created through microcontact printing are frequently small relative to size scales that are straightforward to identify utilizing SEM images. Thus, for some image analyses, we utilized AFM images, which typically provide higher resolution at smaller scales. Figure S.B.9 shows example AFM images of NCDA and HCDA transferred to HOPG using PDMS stamps prepared at 10:2 base:crosslinker ratios. Red lines indicate domains tabulated for number density measurements.

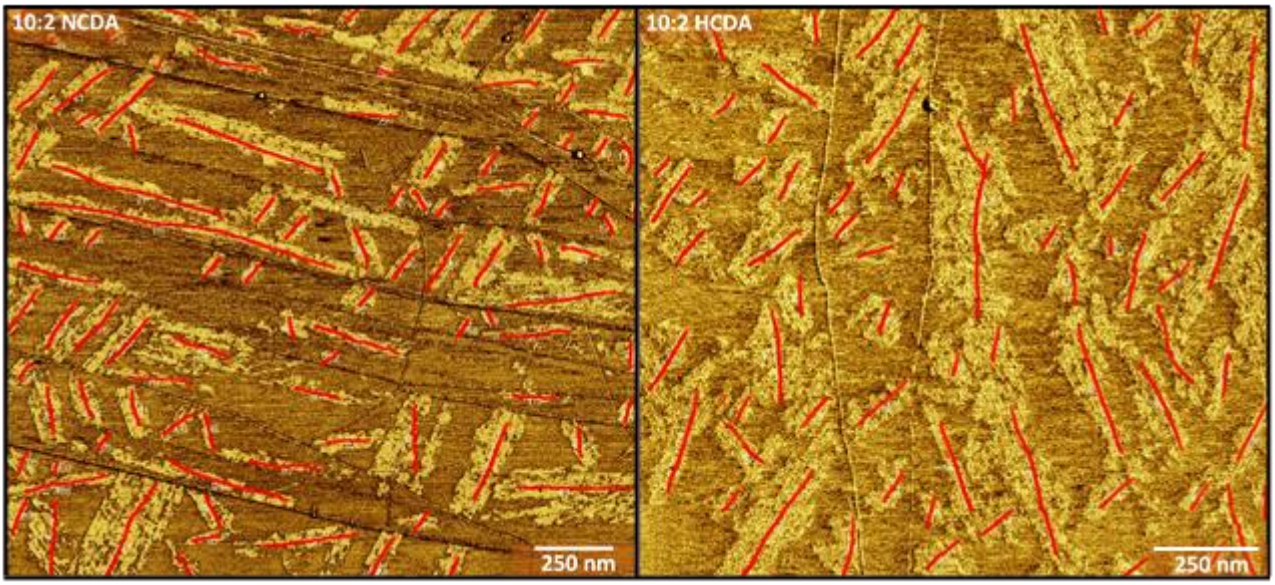

Figure S.B. 9. AFM images showing example domain number density measurements (red lines highlighting each domain) utilized for average domain number density per μm^2 calculations.

Large-scale versions of SEM images shown in Chapter 3

In Chapter 3, several SEM images are shown at small scale to facilitate comparison between molecular transfer conditions. Here, we show SEM images of larger areas of the surface and/or larger image sizes, to increase visibility of features within individual images. Figure S.B.10 shows a mm-scale area of the HOPG surface with areas of transferred PCDA striped phase. The square pattern is faintly visible at this scale, in addition to a large set of HOPG terraces in the lower left quadrant of the image; such features are common on cleaved HOPG. Figure S.B.11 shows an image of a section of the surface from Figure S.B.10, illustrating the degree of fidelity of pattern transfer, and the presence of narrow linear molecular domains (brighter) and amorphous impurities (darker) in the regions between stamp contact areas.

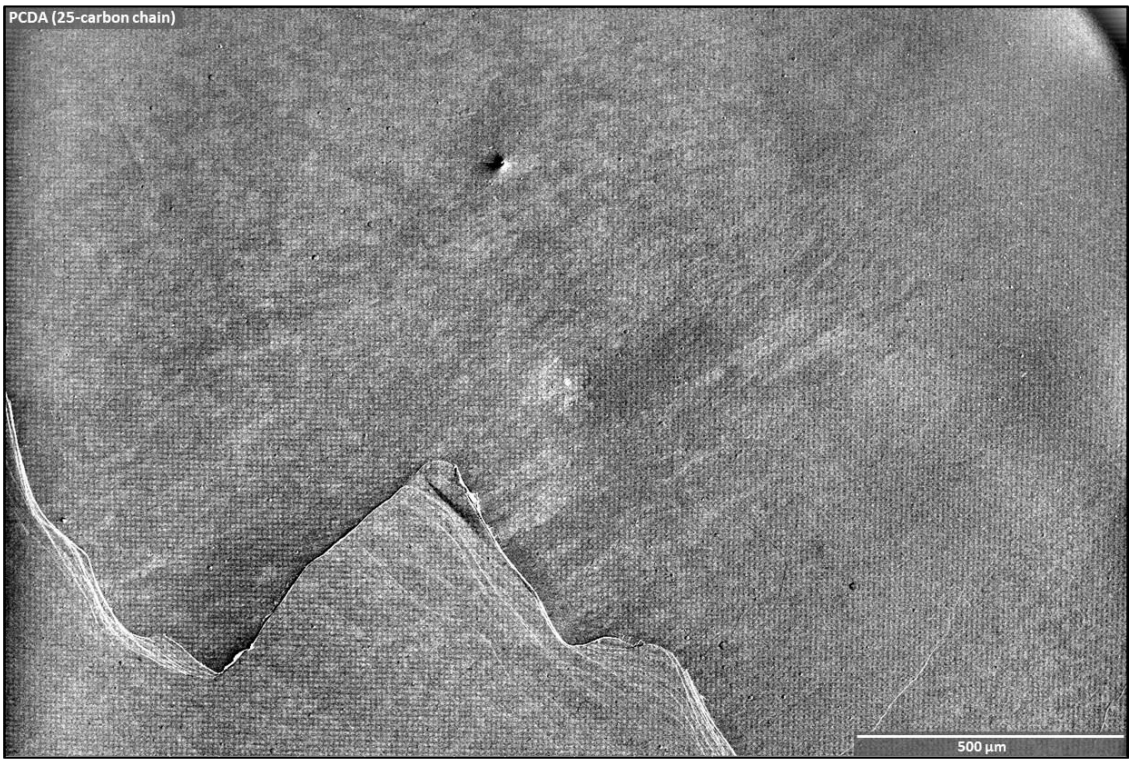

Figure S.B. 10. SEM images of HOPG after stamping with PDMS, illustrating long-range patterning and surface defects common on cleaved HOPG substrates.

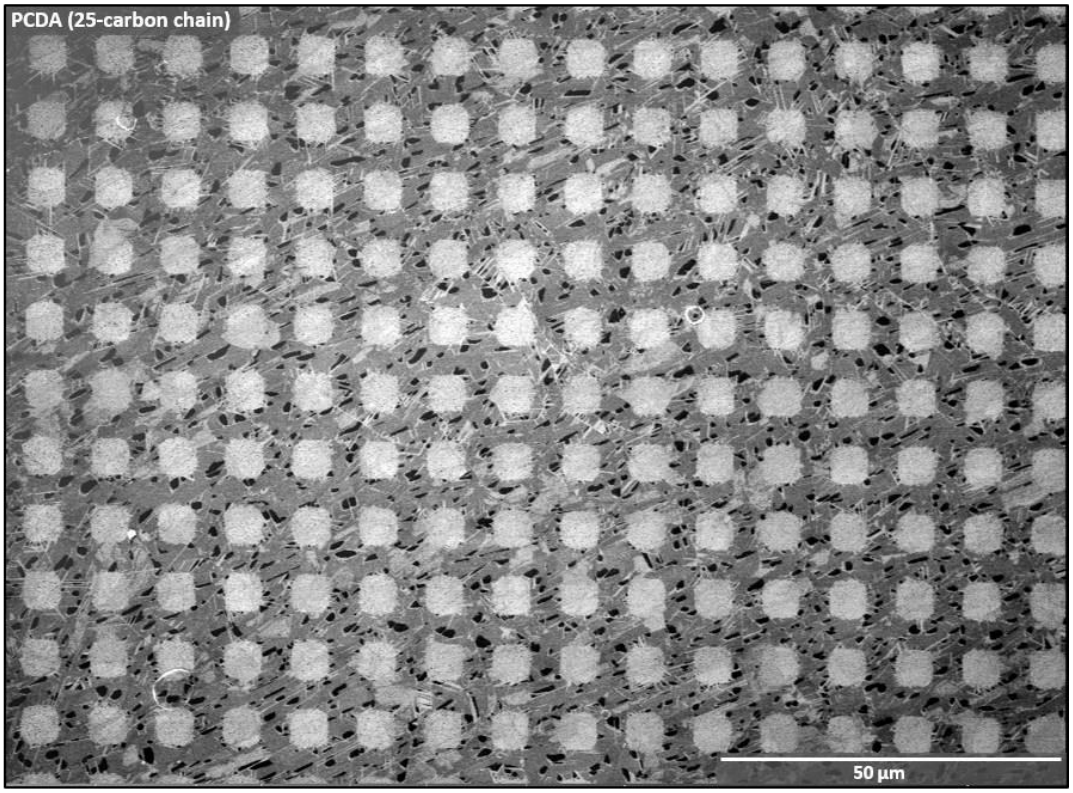

Figure S.B. 11. SEM image of HOPG after stamping with PDMS, illustrating rounded edges of square features in stamp following transfer, and narrow linear molecular domains extending between stamped areas.

Larger versions of images in Chapter 3 illustrating fidelity and quality of transfer

In Chapter 3, individual square areas of deposited NCDA, PCDA, and HCDA are shown in Figure. 3.4. Here, Figure S.B.12– 15 show larger areas around the selected squares for visual comparison. Larger scale images of Diyne PE, Diyne PC, and PI from Figure 3.5-3.7 are shown here in Figure S.B.16-21.

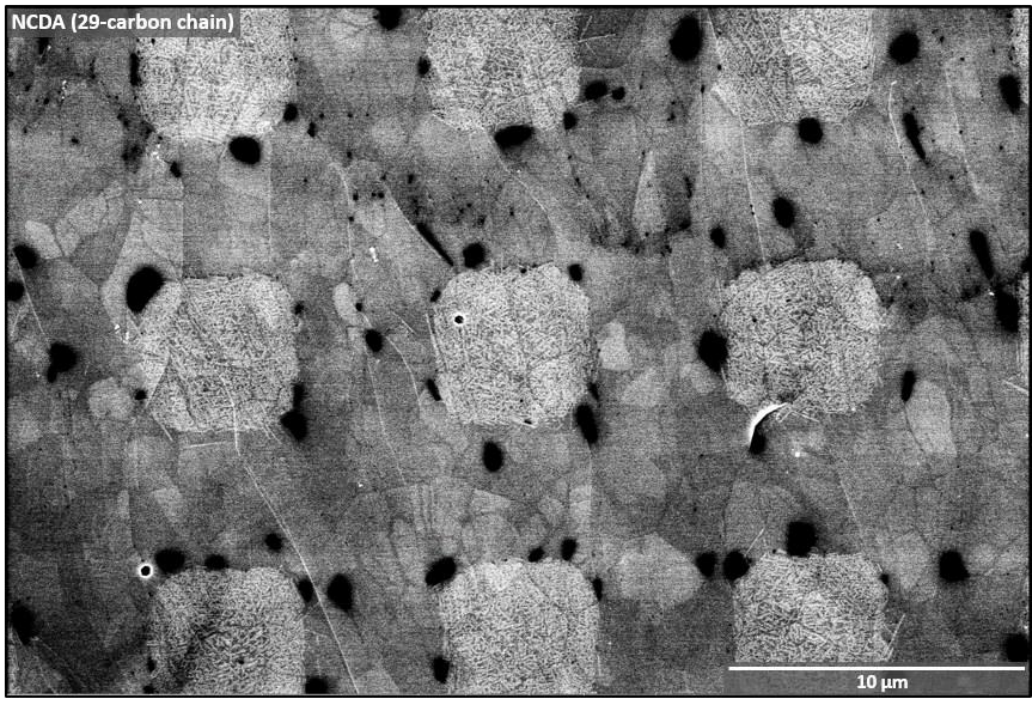

Figure S.B. 12. SEM image of HOPG after stamping with NCDA.

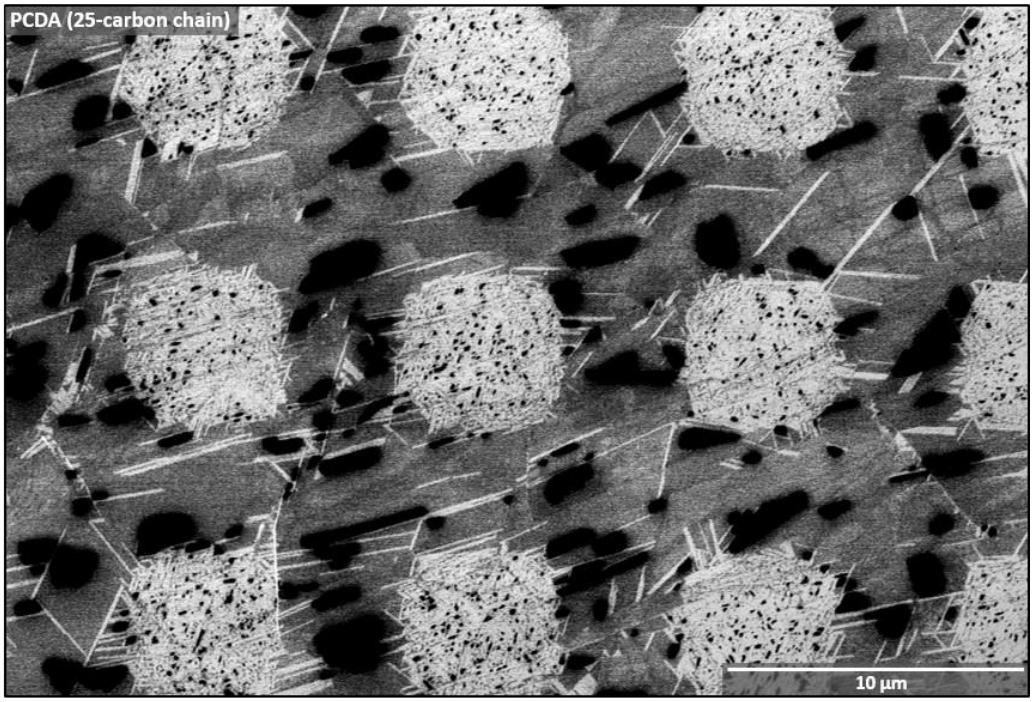

Figure S.B. 13. SEM image of HOPG after stamping with PCDA

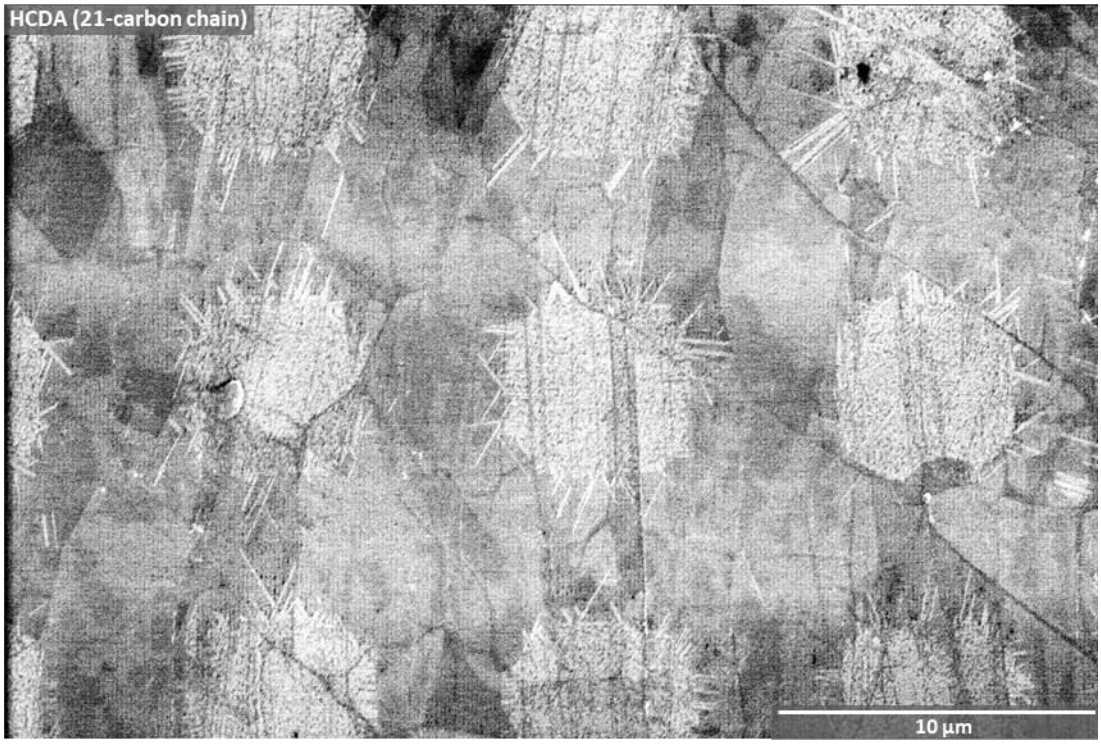

Figure S.B. 14. SEM image of HOPG after flat contact stamping with HCDA.

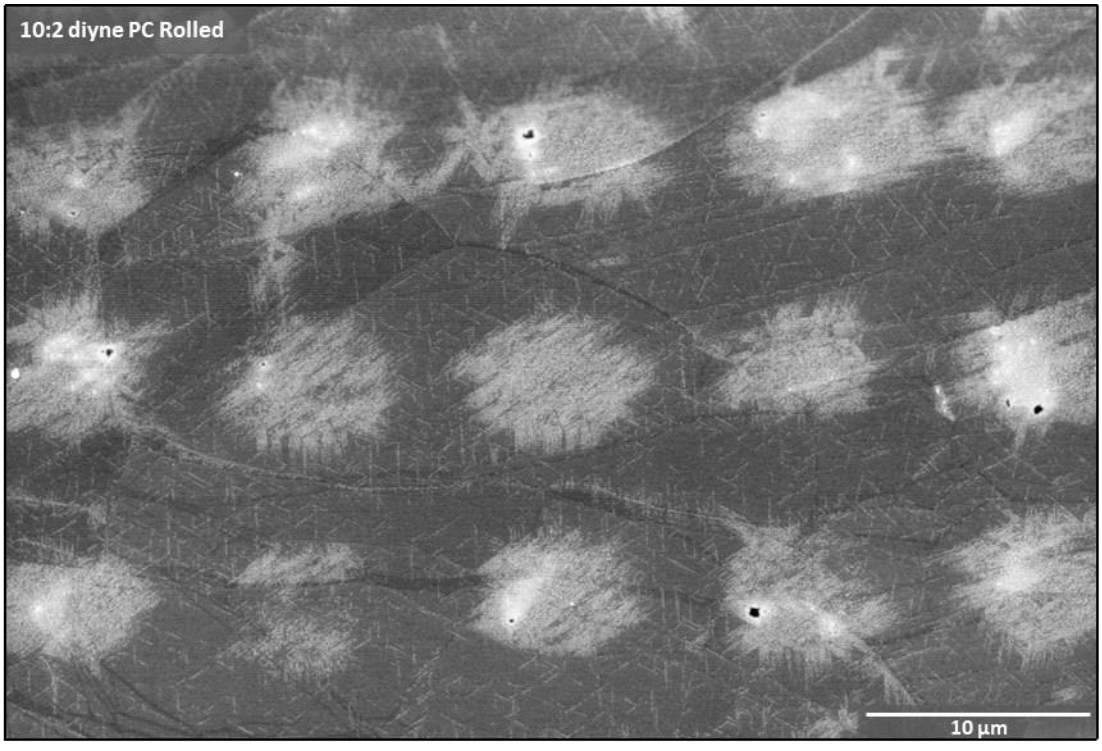

Figure S.B. 15. SEM image of HOPG after rolled contact stamping with Diyne PC.

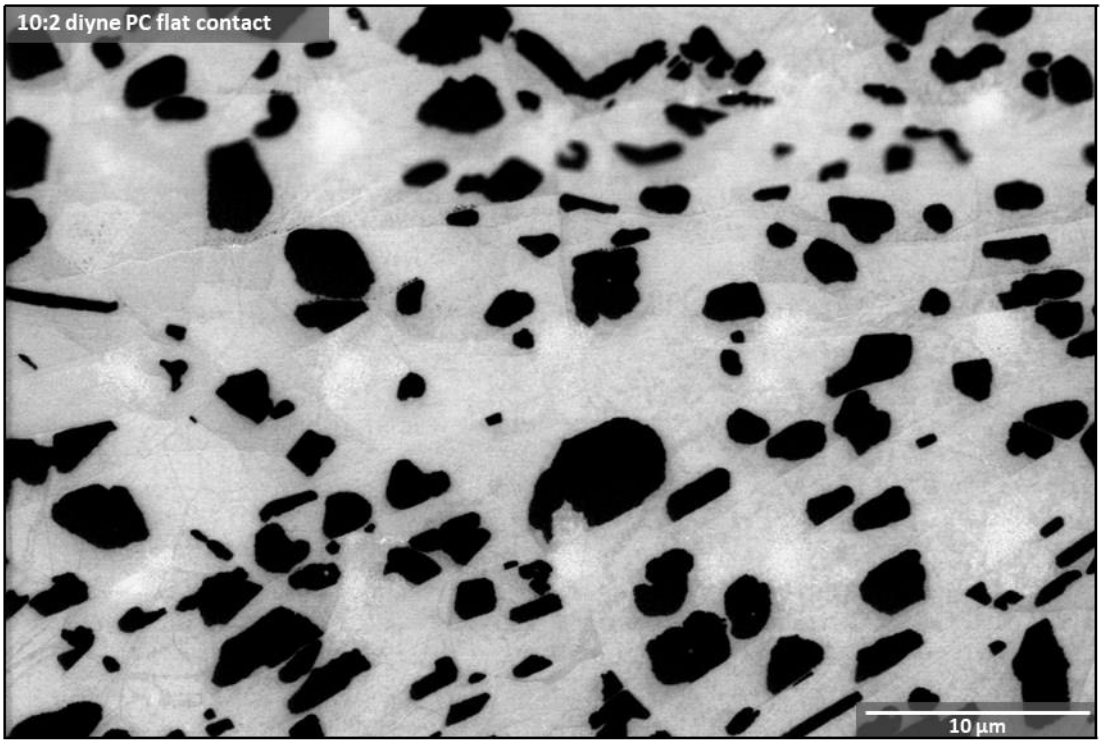

Figure S.B. 16. SEM image of HOPG after flat stamping with Diyne PC.

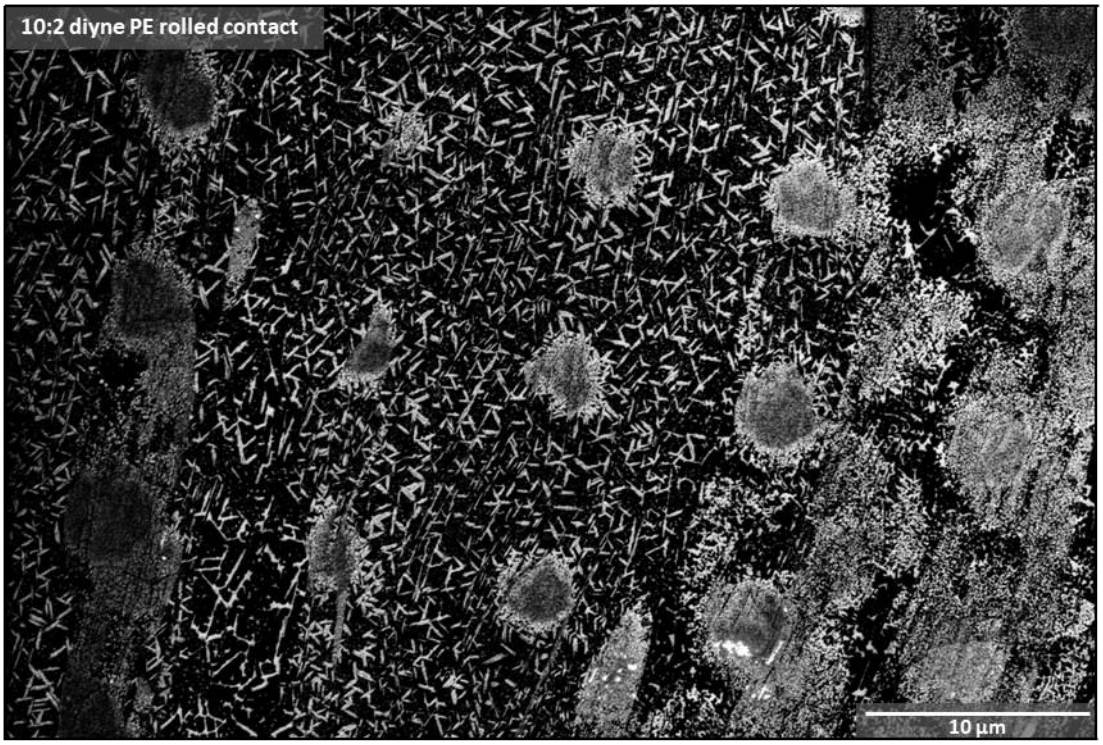

Figure S.B. 17. SEM image of HOPG after rolled contact stamping with Diyne PE.

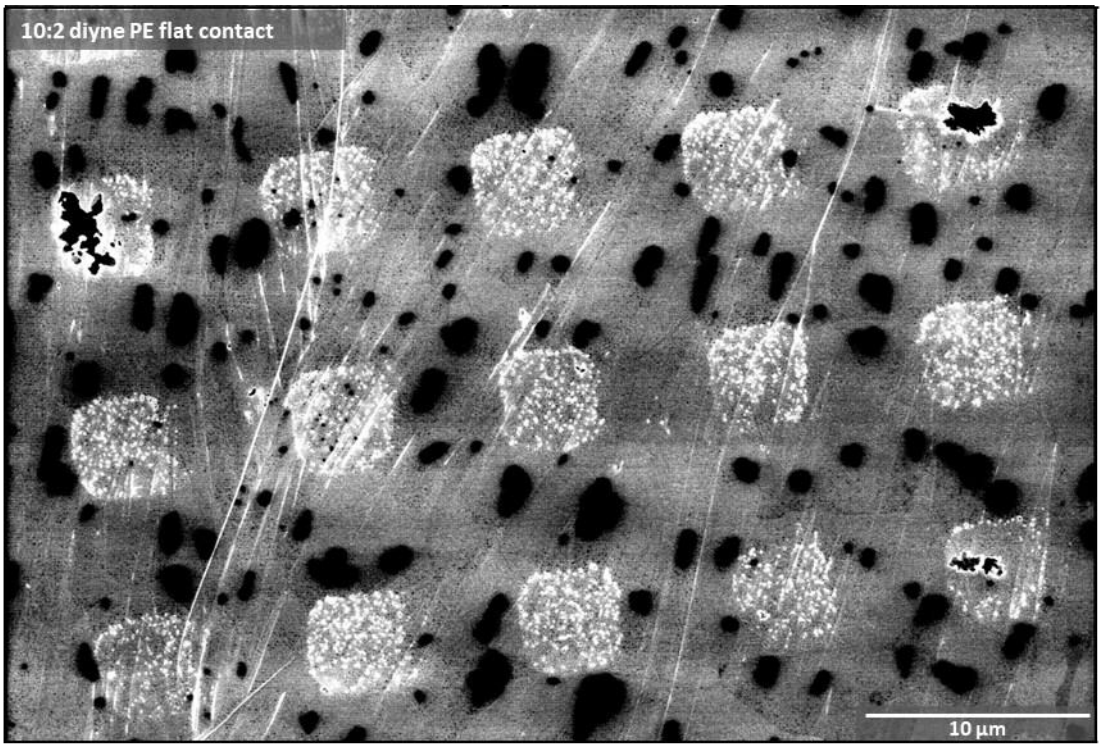

Figure S.B. 18. SEM image of HOPG after flat stamping with Diyne PE.

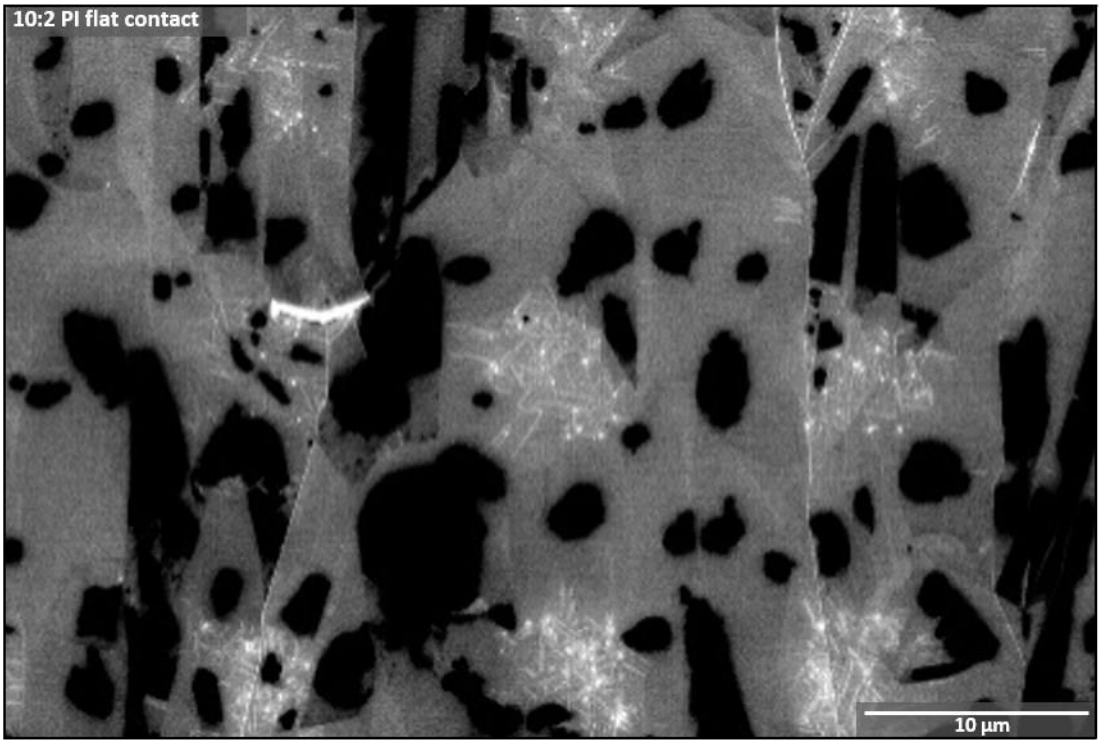

Figure S.B. 19. SEM image of HOPG after flat stamping with PI.

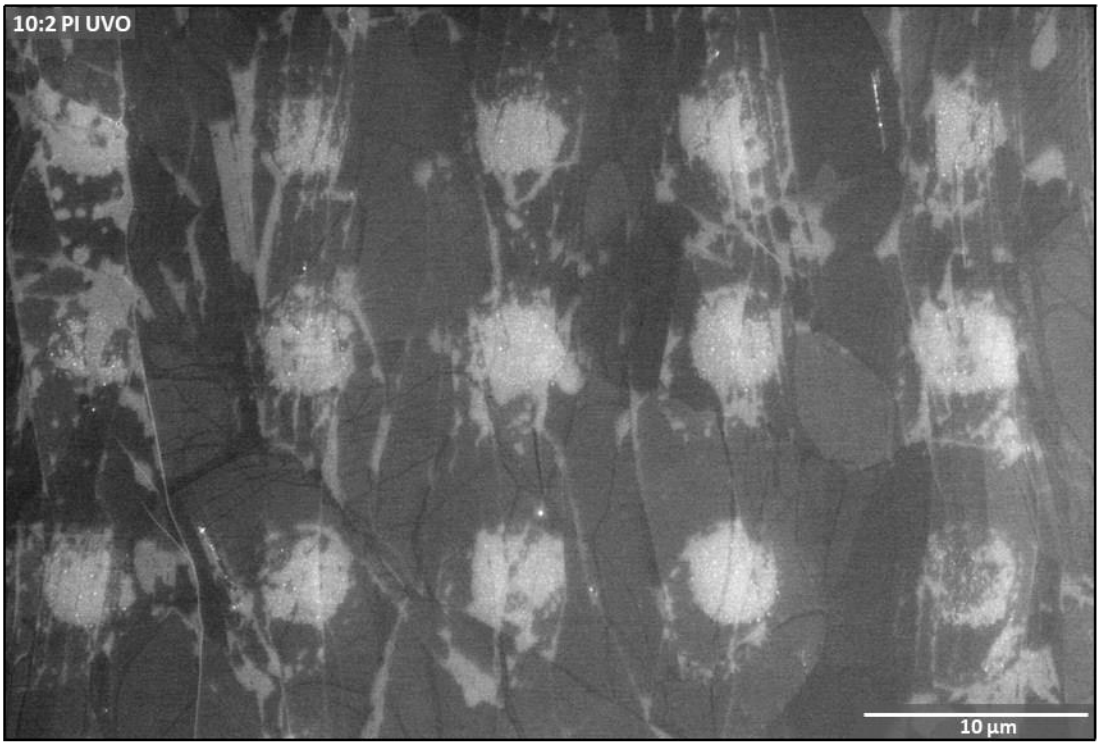

Figure S.B. 20. SEM image of HOPG after flat + UVO contact stamping with PI.

APPENDIX C: SUPPORTING INFORMATION FOR CHAPTER 4

Edge-on adsorption of multi-chain functional alkanes stabilizes noncovalent monolayers on MoS_2

Experimental Methods

Materials

Chloroform (ChromAR grade) was purchased from Macron Fine Chemicals (Center Valley, PA) and used as received. Absolute ethanol (100 % purity) was purchased from Decon Laboratories, Inc. (King of Prussia, PA) and used as received. Manganese(II) chloride tetrahydrate (≥ 98% dry basis) was purchased from Sigma-Aldrich (St. Louis, MO) and used as received. 1,2-Bis(10,12-tricosadiynoyl)-sn-glycero-3-phosphoethanolamine (diyne PE, >99.0% purity) was purchased from Avanti Polar Lipids (Alabaster, AL) and 10,12-Pentacosadiynoic acid (PCDA, ≥ 97.0% purity) was purchased from Sigma-Aldrich (St. Louis, MO); both were used as received. Milli-Q water (≥18.2 MΩ·cm resistivity) was used in all experiments. Ultrahigh purity nitrogen was purchased from Indiana Oxygen Company (Indianapolis, IN; 99.999% purity). Self-assembled monolayers of lipids were deposited on either 1 cm × 1 cm highly oriented pyrolytic graphite (HOPG, MicroMasch, Watsonville, CA) substrates or 1 cm^2 molybdenum disulfide (MoS_2, SPI Supplies, West Chester, PA) substrates; substrates were freshly cleaved immediately prior to sample deposition. All initial steps in the deposition process were carried out under UV-filtered light to prevent polymerization in solution. PELCO conductive liquid silver paint, standard SEM pin stub mounts, and double coated carbon conductive tape were purchased from Ted Pella, Inc. (Redding, CA).

Langmuir-Schaefer (LS) conversion

LS conversion was performed using a MicroTrough XL Langmuir–Blodgett trough (Kibron Inc., Helsinki, Finland). For the deposition of PCDA, 30 μL of a 0.5 mg/ml solution of PCDA in chloroform was deposited on a subphase of deionized water (~18 MΩ·cm). After the small amount of chloroform used for amphiphile transfer was allowed to evaporate (typical equilibration time 15 min), trough barriers were slowly moved inward (4.3 mm/min barrier motion), to increase film uniformity across the trough surface.

At the target average molecular area (*e.g.*, 35 $Å^2$/molecule), the substrate was slowly (5 mm/min) lowered onto the subphase with the cleaved surface facing down, nearly parallel to the liquid interface, using an automated dipper. After 4 min in contact with the liquid interface, the HOPG was gently lifted out of contact with the liquid using the automated dipper at the same speed. The deposition of diyne PE followed the same procedure, utilizing a subphase of 5 mM $MnCl_2$.

Unless stated otherwise, diacetylene-functionalized amphiphile monolayers prepared using the described procedure were photopolymerized prior to imaging in order to improve monolayer stability. Photopolymerization was performed by 10–360 min of irradiation under a 254-nm 8-W UV lamp with approximately 4 cm between the lamp and the sample surface.

Temperature-controlled LS conversion

To enable temperature controlled LS conversion, a temperature-controlled transfer stage that was reported previously[1] was used. Samples were mounted on the stage utilizing standard 12 mm diameter high quality magnetic stainless steel AFM specimen discs (alloy 430, Ted Pella, Inc.) that mount on a magnet recessed in the body of the stage. To maximize temperature uniformity across the substrate surface, conductive carbon tape was used to affix the back of the substrate to the specimen disc surface. The temperature of the substrate was confirmed using a thermocouple prior to dipping.

Solution processing assays

For washing experiments, lipid films were subjected to a vigorous stream of ethanol delivered via syringe; in a typical washing experiment, 5 mL of solvent was used. Immediately following each solvent wash, the sample was blown dry with ultrahigh purity nitrogen. After solvent rinsing and substrate drying, AFM imaging was performed, imaging the same location before and after washing.

SEM imaging

SEM images were obtained on a FEI NOVA NanoSEM Field Emission SEM or a Teneo VS SEM (FEI Company, Hillsboro Oregon). Microscopy from the FEI NOVA NanoSEM was

performed at 5 kV accelerating voltage at a ~3 mm working distance, with an aperture of 30 μm, producing a current of ~0.896 nA. Images were acquired using a through-thelens detector (TLD) with an immersion lens. SEM images obtained on the Teneo VS SEM were acquired at a working distance of ~5 mm using the segmented in-lens T3 detector. A beam current of 3.2 nA was selected for best resolution image acquisition through a 32 μm diameter aperature with an accelerating voltage of 5 kV. All substrates were affixed to standard SEM pin stub specimen mounts with conductive carbon tape. To further enhance substrate–mount conductivity, a small amount of colloidal silver paint was applied along the perimeter of the substrate from the face down to the underlying pin stub.

AFM imaging

All AFM measurements were performed under ambient conditions using a Bruker (Bruker Instruments, Billerica, MA) MultiMode AFM equipped with an E scanner. The cantilever oscillation phase shift was carefully monitored to ensure the tip was engaged in the attractive mode to improve imaging of lamellar structures within domains. The setpoint ratio was typically maintained between 0.4 and 0.7 and was rarely decreased below 0.4 to avoid tip sweeping effects.

Image analysis

Images were processed using Gwyddion scanning probe microscopy data visualization and analysis software[2] and ImageJ analysis software[3] to perform median line corrections, plane flattening, scar artifact removal, and contrast adjustment.

Energy minimization

Software packages Maestro and Macromodel (Schrödinger, Cambridge MA) were used, respectively, to visualize molecular structures and to perform force field minimizations. Models were minimized using the OPLS_2005 force field, with extended cutoffs for Van der Waals, electrostatic, and hydrogen bonding interactions. The dielectric constant of the simulation was set to 80.1. Minimizations were performed using the Polak-Ribiere conjugate gradient (PRCG) algorithm and gradient method with 50000 runs and a convergence threshold of 0.05.

Alignment of diynes in stacked phases for polymerization

In Chapter 4 Figure 4.1, we show a molecular model of diyne PE on MoS_2 in an edgeon adsorption geometry. Here, to facilitate visual inspection, we highlight the positions of the diynes in the two layers of alkyl chains (Figure S.C. 1a); red lines indicate the lower layer of diynes, while gold lines indicate the top layer. Minimized molecular models in Figure S.C 1b-d illustrate top views of models in which only the bottom layer of diynes has been polymerized (Figure S.C 1b), only the top layer (Figure S.C 1c), and both layers (Figure S.C 1d). The left row of molecules is assembled with the phosphate oriented toward the environmental interface; the right row of molecules has the phosphate oriented down toward the MoS_2. This difference in asssembly leads to a substantial difference in the alignment of the diynes in the two layers across the width of the lamellae, although in both cases the layers of diynes orient at approximately right angles to one another, increasing the likelihood that the two layers polymerize separately. Such behavior would be congruent with the polymerization of diyne phospholipids observed previously in standing phases.[4]

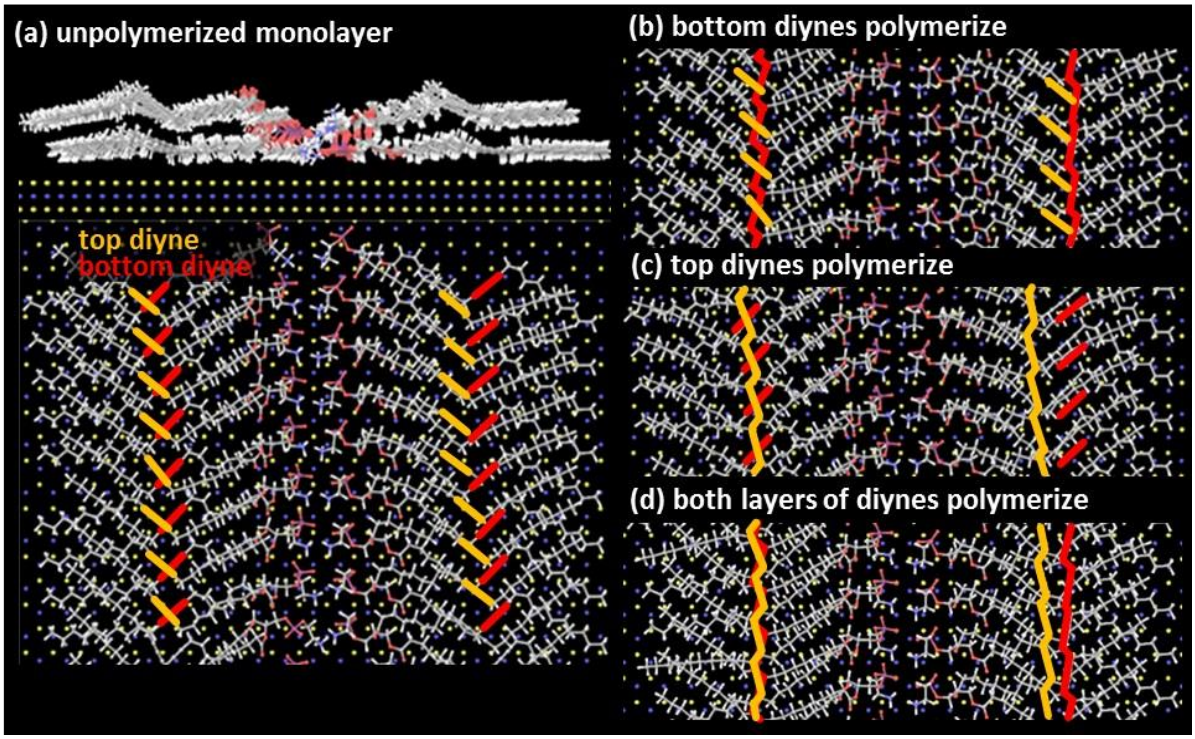

Figure S.C. 1. . Molecular models of diyne PE in edge-on adsorption geometry, with positions of diynes highlighted in red (bottom layer) and gold (top layer). Each model illustrates a different

possible polymerization state of the monolayer: (a) unpolymerized, (b) bottom layer of diynes polymerized, (c) top layer of diynes polymerized, and (d) both layers of diynes polymerized.

Larger versions of images in Chapter 4 illustrating differences in domain height and rotation for diyne PE on MoS2

In Chapter 4, AFM images illustrate two distinct classes of diyne PE domain heights on MoS_2 that are visible at sub-monolayer coverage. Here, we show a larger version of the image for visual comparison (Figure S.C 2), highlighting that areas of both phases are visible in the lowercoverage area in the center. The AFM phase images (Figure S.C 2 inset) shows the lack of lamellar contrast in the lowest topography area, indicating that it represents the MoS_2 substrate. Within the diamondoid vacancy in the monolayer are also regions in which molecules assemble epitaxially on the substrate, with a majority domain height of ~0.4 nm, and local linear protrusions with a total height of 0.6-0.8 nm in comparison with the substrate. It is not possible to completely exclude the possibility that these regions represent a second layer of molecules with face-on orientation. However, the fact that these very small molecular areas are stable toward repeated imaging and do not further consolidate to form a terrace suggests that they are in fact lines of molecules with edge-on adorption geometries. Figure S.C 3 shows a larger area of the same substrate with ~80% edge-on adsorption and 4% face-on adsorption, and 16% vacancies.

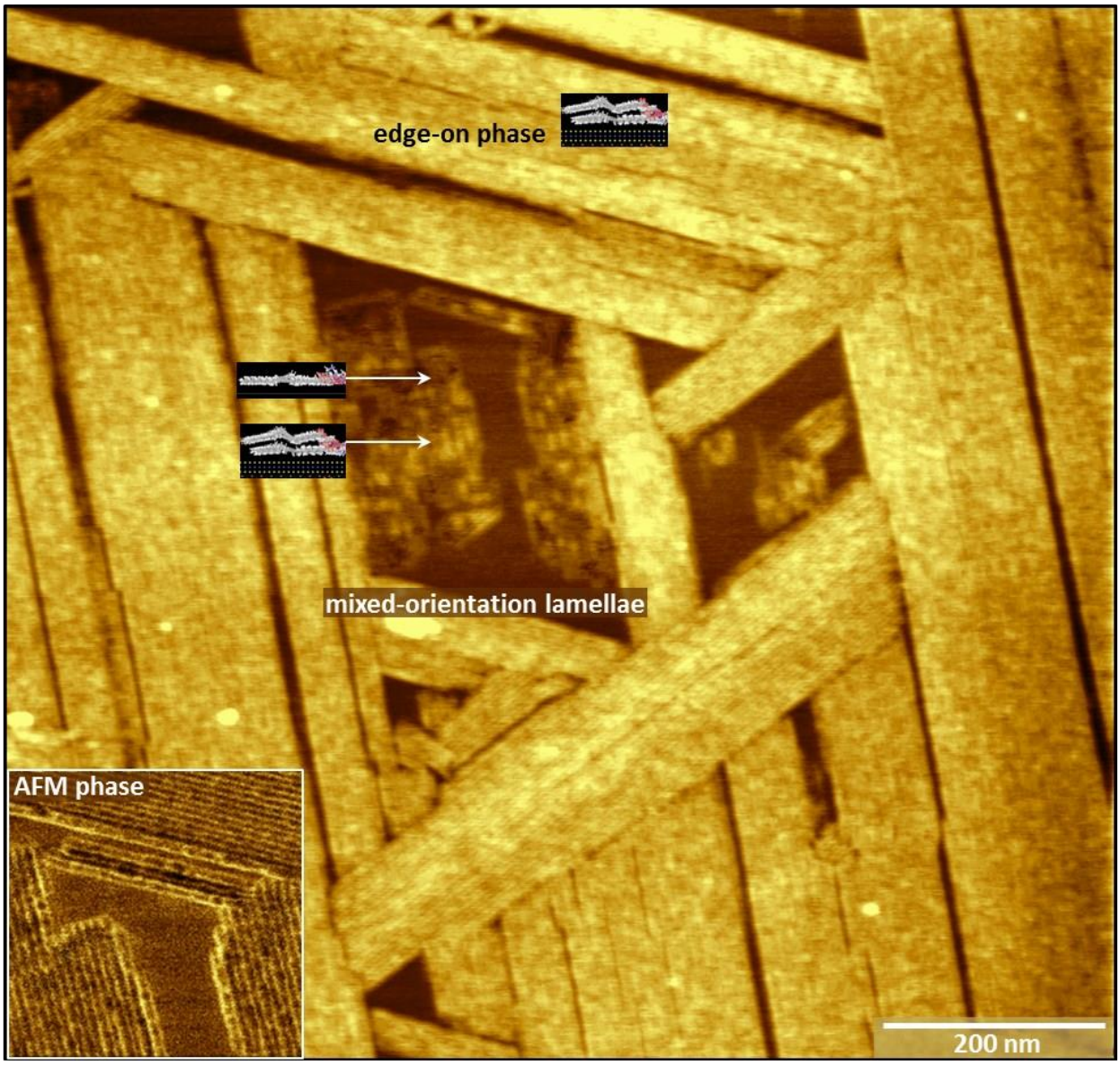

Figure S.C. 2. Representative AFM image of diyne PE at sub-monolayer coverage on MoS_2, illustrating domains exhibiting edge-on and face-on adsorption. AFM phase image (inset) shows lack of lamellar contrast in background, indicating that the background represents the MoS_2 substrate.

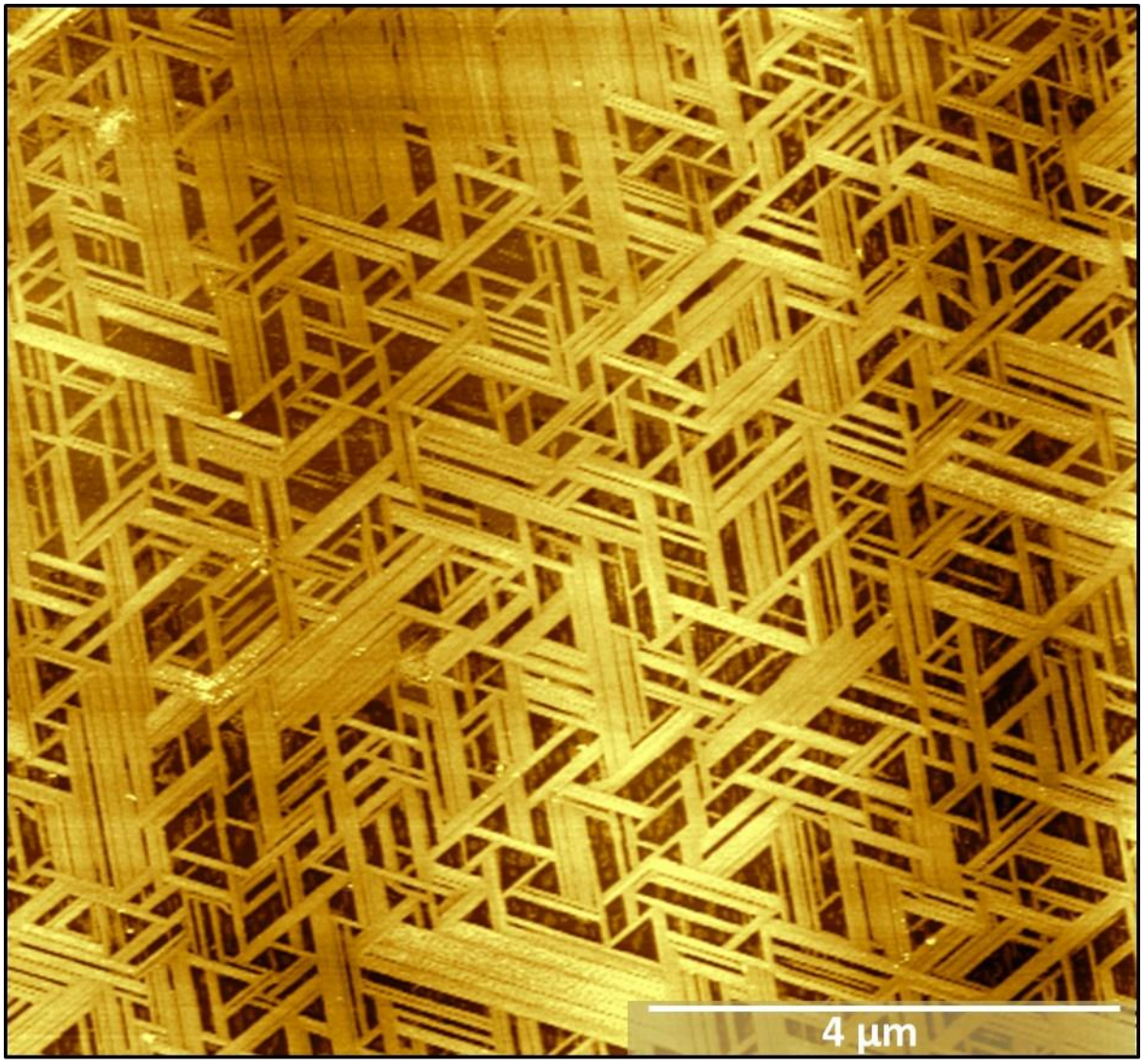

Figure S.C. 3. Large-area AFM image of diyne PE on MoS_2 at sub-monolayer coverage. Small domains of molecules in face-on adsorption geometries are visible in the triangular vacancies.

SEM images (Figure S.C 4) at high coveage also reveal reasonably uniform contrast, consistent with predominantly monolayer coverage. Previously we have found that in areas with significant variations in film thickness, contrast changes are evident in the SEM image, which is evident under some transfer conditions in the thermal screening section presented later in the ESI.

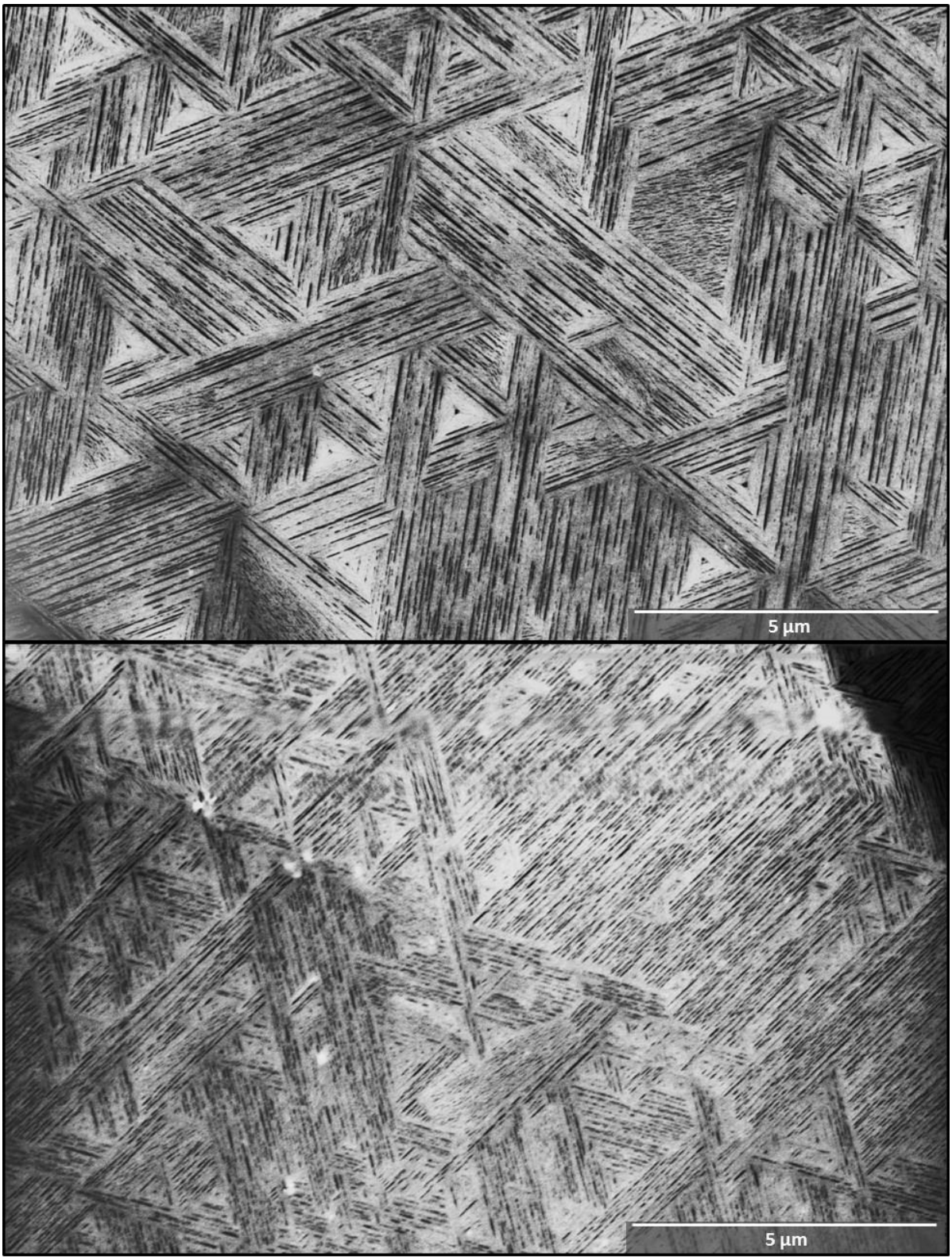

Figure S.C. 4. SEM images of diyne PE on MoS_2 exhibiting long-range ordering.

Figure 4.2e shows a line scan extracted from an image of diyne PE on HOPG; the image from which the line scan is extracted is included below as Figure S.C 5, with the location of the line scan highlighted in white.

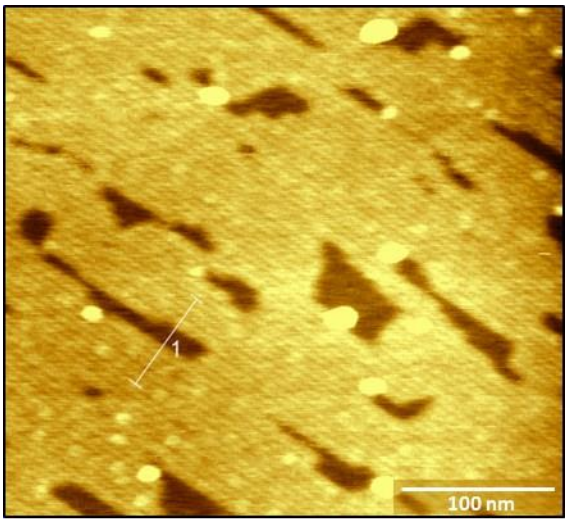

Figure S.C. 5. AFM image of diyne PE on HOPG used for line scan in Figure 4.2e. Extracted line is highlighted in white.

In Chapter 4, Figure 4.5b illustrates that certain domains (color-coded yellow in Figure 4.5b) are rotated ~5° relative to the main domain alignment direction. Here, we show the original image at larger scale (Figure S.C 6), to facilitate comparison, with line scans acquired from adjacent rotated domains (inset), to illustrate the small difference in lamellar periodicity (averaged difference ~0.3 nm). While drift can also contribute to differences in measured distances, four pairs of domains measured at different angles relative to the fast scan axis reflect similar percentage differences in lamellar periodicity. Domain rotation is also visible in the SEM images in Figure S.C 4.

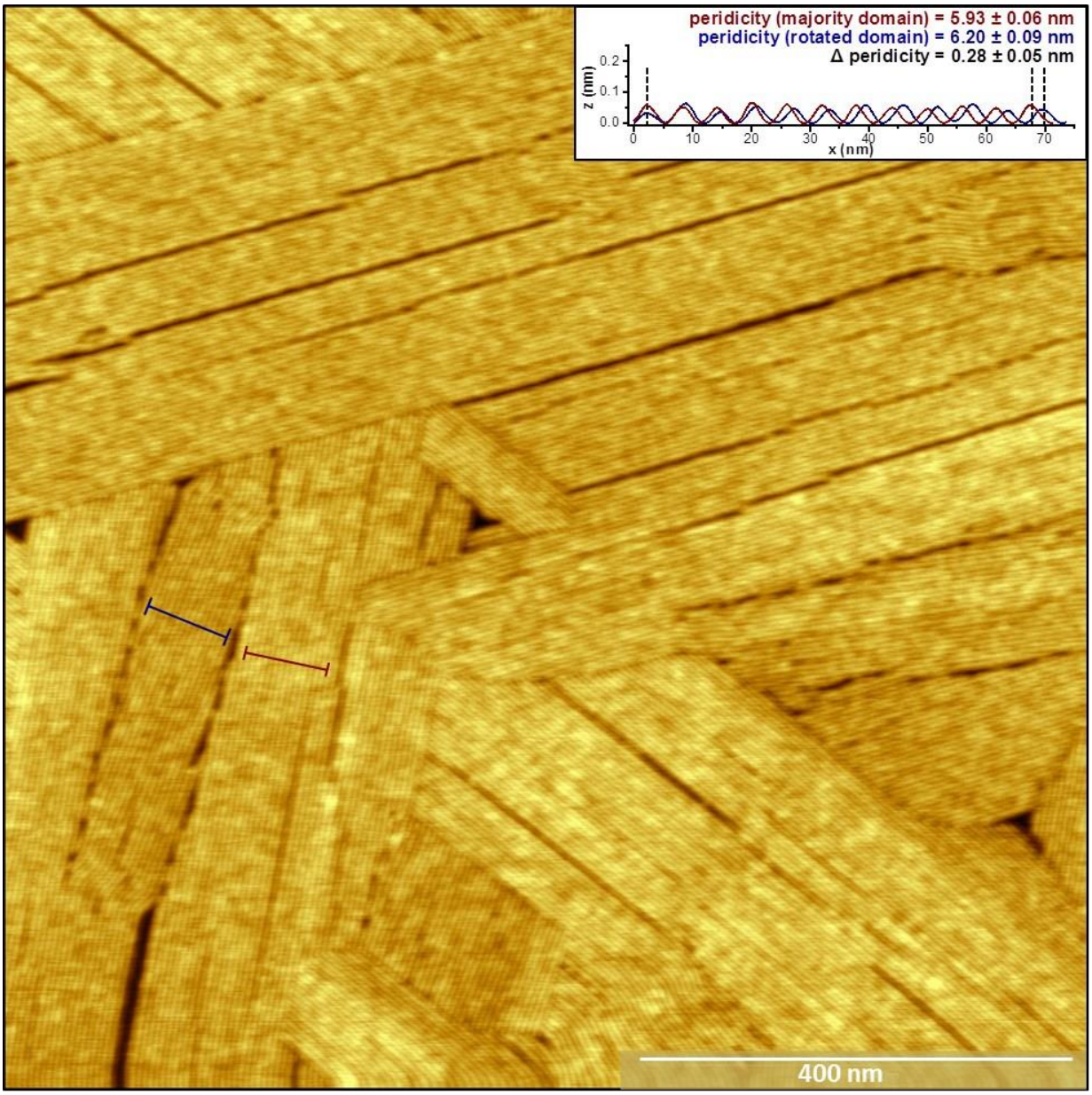

Figure S.C. 6. Representative AFM images of diyne PE with a subset of domains rotated relative to the majority domain alignment direction.

Polymerization of diyne PE on HOPG for periods up to 6 h

To examine whether the changes in diyne PE monolayer structure observed in 1 h of polymerization on MoS_2 were substrate-specific, we examined monolayers on HOPG through longer polymerization times. Figure S.C 7 illustrates diyne PE on HOPG prior to polymerization (Figure S.C 7a,b), and after 1 h (Figure S.C 7c), 2h (Figure S.C 7d), 3 h (Figure S.C 7e), and 6 h

(Figure S.C 7f) of UV irradiation. After 1 h, lamellar roughening begins to occur in the monolayer, while after 3 and 6 h, more substantial restructuring is observed, similar to that observed on MoS_2 after 1 h. The images shown were acquired from similar areas of a single sample in sequence.

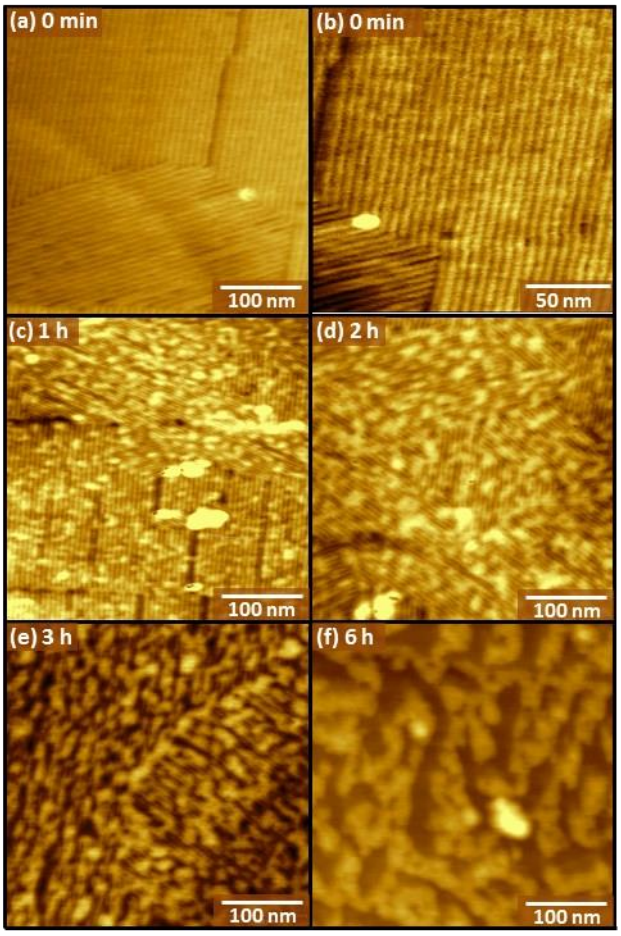

Figure S.C. 7. Representative AFM images of diyne PE transferred to HOPG, and exposed to UV radiation for (a,b) 0 min, (c) 1 h, (d) 2 h, (e) 3 h, or (f) 6 h.

Proposed majority and minority domain structures

In Chapter 4, Figure 4.5 illustrates a proposed majority domain structure for diyne PE on MoS_2, based on differences in linear defects and rotational angles between domains. Here, we propose a structure and for the minority domain structure, based on minimized molecular models of the three possible lamellar median structures (Figure S.C 8).

The two possible edge-on adsorption geometries for diyne PE lead to three possible conformations at the lamellar median. Here, we categorize these based on the orientation of the ammonium groups on each side of the median (up | up, up | down, and down | down). Single-point

energy calculations for each minimized model indicate the magnitudes of the averaged per-molecule adsorption enthalpies follow the trend up | up > up | down > down | down. This is reasonable given that the N up adsorption geometry brings the entire glycerol backbone into contact with the substrate, in addition to the phosphate, ester, and acyl chain, resulting in a greater number of van der Waals contact with the substrate.

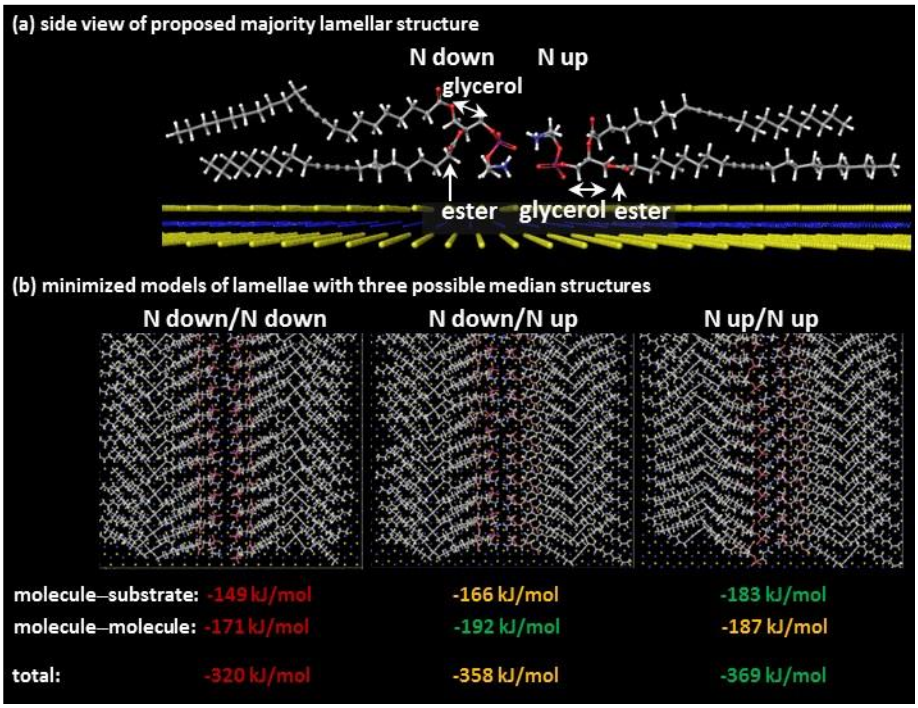

Figure S.C. 8. (a) Side view of minimized molecular model of proposed majority lamellar structure, illustrating difference in molecular contact with the substrate in N-down and N-up adsorption geometries. (b) Minimized molecular models of lamellae with three possible median structures (down | down, down | up, and up | up), with calculated molecule–substrate and molecule–molecule interaction strengths.

Conversely, molecule–molecule interactions are slightly stronger for the up | down adsorption geometry, which provides a greater packing density on the substrate. Both N-up and N-down adsorption geometries place terminal methyl groups at different positions relative to the lamellar median, with the result that domains assembled from either up | up or down | down lamellar structures produce inefficient packing of chain ends between lamellae. In contrast, the up | down configuration allows for interdigitation of chain ends.

Structural features observed in SEM are consistent with a domain structure with interlocked edges (*i.e.* N up | N down) for the majority domains. Previously, we have observed that cracking defects form in domains of diynes on HOPG under the electron beam. Small cracks also appear in AFM images of highly ordered domains after polymerization, though the cracks observed in SEM images are greater in width, pointing to the likelihood of some additional restructuring under the electron beam. In SEM images of diyne PE on MoS_2, the majority domain structure exhibits long narrow defects even prior to polymerization, but does not develop additional defects under the electron beam. In contrast, the minority domains develop small linear cracks similar to the polymerization-induced cracking observed previously on HOPG.

Both AFM and SEM images reveal a 5-10° rotational offset between the lamellar axes of the majority and minority domains. Again, this would be consistent with a shift from down | up to up | up lamellar median, as shown in Figure S.C 9.

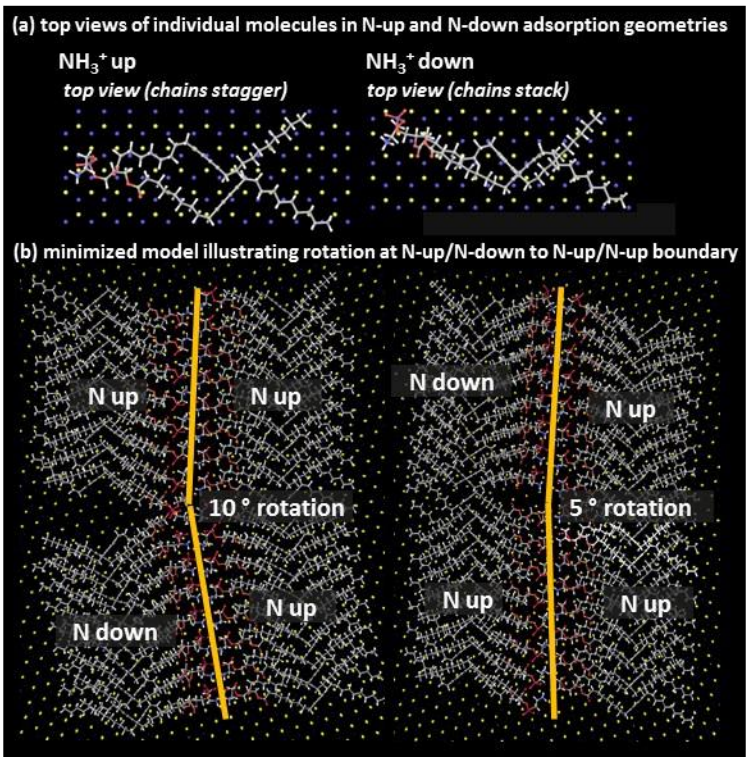

Figure S.C. 9. Top views of N-up and N-down adsorption geometries, illustrating difference in chain stacking. (b) Minimized molecular models illustrating rotation at boundary between Nup/N-down and N-up/N-up assembly.

Representative SEM images for transfer of diyne PE to MoS2 at substrate temperatures 30–90 °C

Transfer of dual chain amphiphiles to MoS_2 across a range of temperatures is compared in Figure S.C 10–S.C. 11. In these experiments, the subphase was held at 30 °C, and the substrate was held at the stated temperature using a custom-built thermally controlled dipper reported previously.[1] Each row in Figure S.C 10–S.C. 11 comprises three representative SEM images (scale bars 100 μm, left, to 1 μm, right) acquired from substrates held at the temperature indicated in the left panel. Images on the left illustrate large-scale features that typically arise from Langmuir film structure; images on the right illustrate lamellar and other domain structures produced at the specified transfer condition. To compare the effect of Langmuir film packing on transfer to MoS_2, transfer was tested at two Langmuir film packing densities: 20 $Å^2$/chain (Figure S.C 10) and 35 $Å^2$/chain (Figure S.C. 11). These points were chosen to also enable comparison with transfers to HOPG performed previously.

At elevated temperatures and packing densities of 20 $Å^2$/chain, lamellar domains are observed for transfers to MoS_2, with large (>1 μm edge length) domains at 50–70 °C (Figure S.C 10b,c). In contrast, lamellar domain assembly on MoS_2 is minimal for transfer from Langmuir films at 35 $Å^2$/chain or greater (Figure S.C 11). Higher defect densities in Langmuir films at these mma values likely increase transfer rates, and may also permit increased transfer of water from the subphase; both factors could impede assembly of stable lamellar domains on MoS_2, which is more hydrophilic than HOPG.

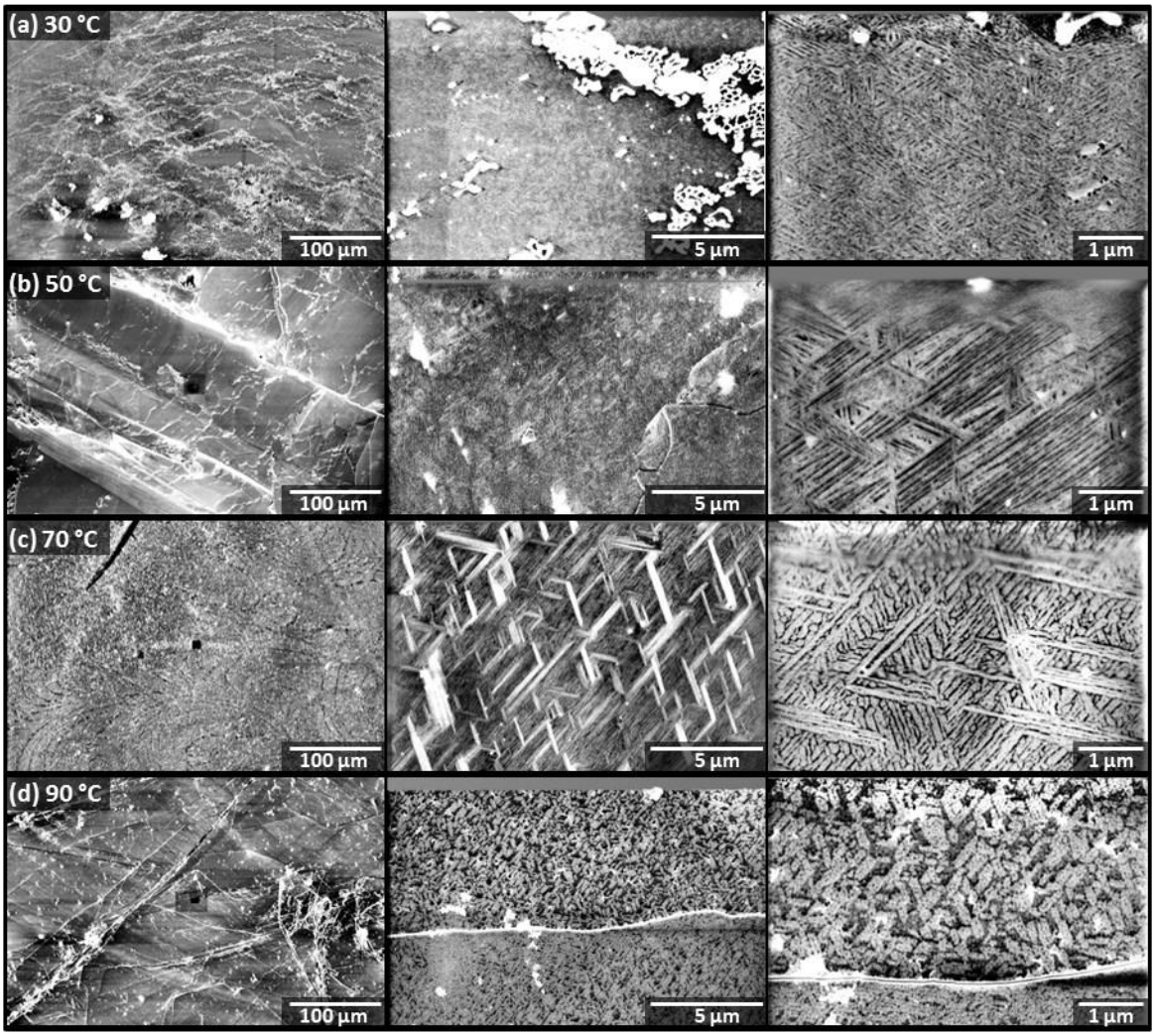

Figure S.C. 10. Representative SEM images of diyne PE transferred to MoS_2 from Langmuir films with a packing density of 20 $Å^2$/chain and a subphase temperature of 30 °C. Substrate was held at a dipper setpoint temperature of (a) 30 °C, (b) 50 °C, (c) 70 °C, or (d) 90 °C. Each row comprises images at three different scales for the substrate temperature stated in the left panel.

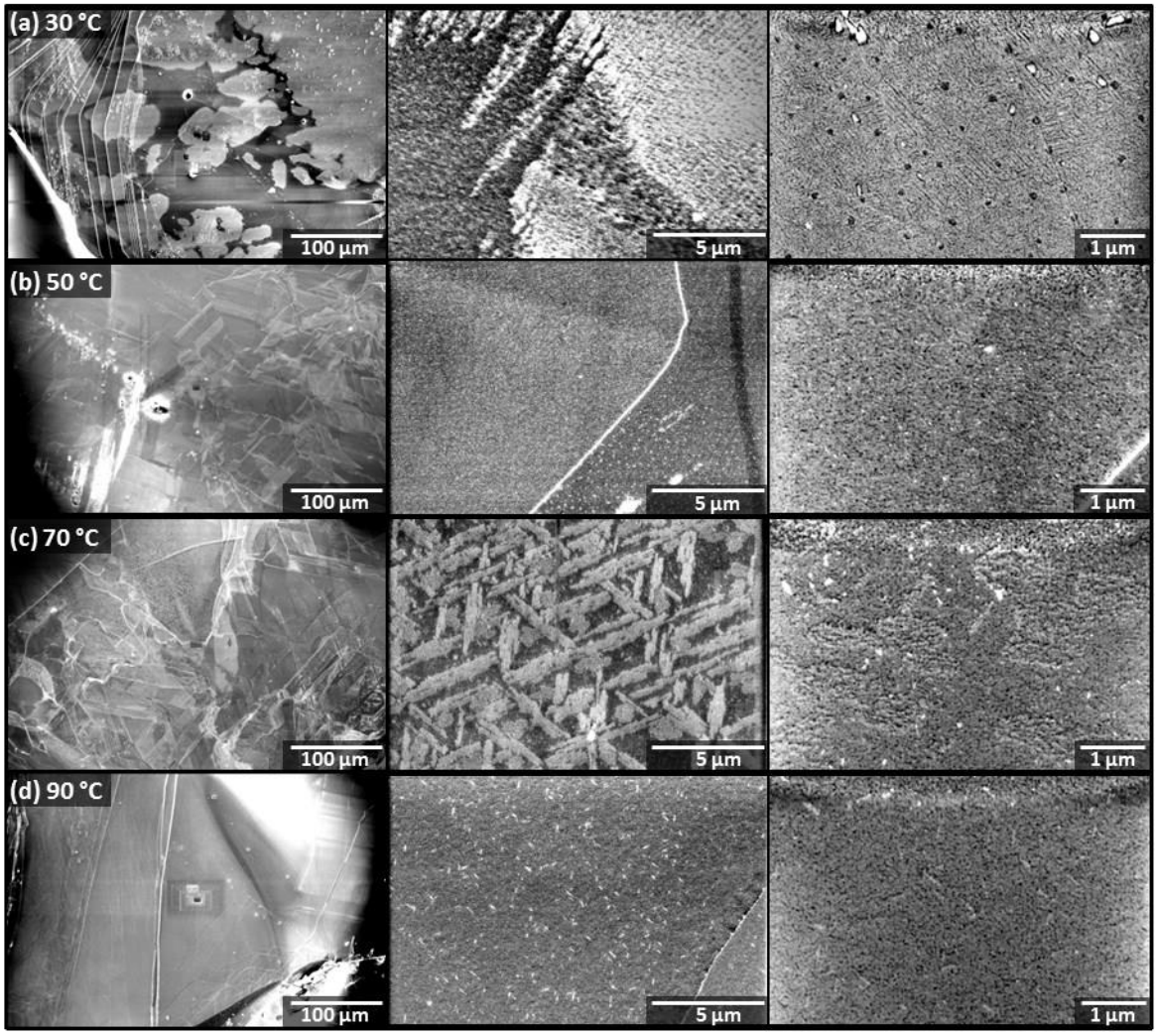

Figure S.C. 11. Representative SEM images of diyne PE transferred to MoS_2 from Langmuir films with a packing density of 35 $Å^2$/chain and a subphase temperature of 30 °C. Substrate was held at a dipper setpoint temperature of (a) 30 °C, (b) 50 °C, (c) 70 °C, or (d) 90 °C. Each row comprises images at three different scales for the substrate temperature stated in the left panel.

Representative SEM images for transfer of PCDA to MoS2 and HOPG at substrate temperatures 30–90 °C

Transfer of single chain amphiphiles to MoS_2 across a range of temperatures is compared in Figures S.C.12-S.C.13. In these experiments, the subphase was held at 30 °C, and the substrate was held at the stated temperature using a custom-built thermally controlled dipper reported previously.[1] Each row in Figures S.C.12-S.C.13 comprises three representative SEM images (scale bars 100 µm, left, to 1 µm, right) acquired from substrates held at the dipper setpoint temperature stated in the left panel. Images on the left illustrate large-scale features that typically arise from

Langmuir film structure; images on the right illustrate lamellar and other domain structures that result from the specified transfer condition. To compare the effect of Langmuir film packing on transfer to MoS_2, transfer was tested at two Langmuir film packing densities: 20 $Å^2$/chain (Figure S.C.12) and 35 $Å^2$/chain (Figure S.C.13). Transfer of PCDA to MoS_2 under a similar range of conditions to those utilized for diyne PE (Figure S.C.10-S.C. 11) produced high surface coverage, but not large lamellar domains similar to those observed for diyne PE.

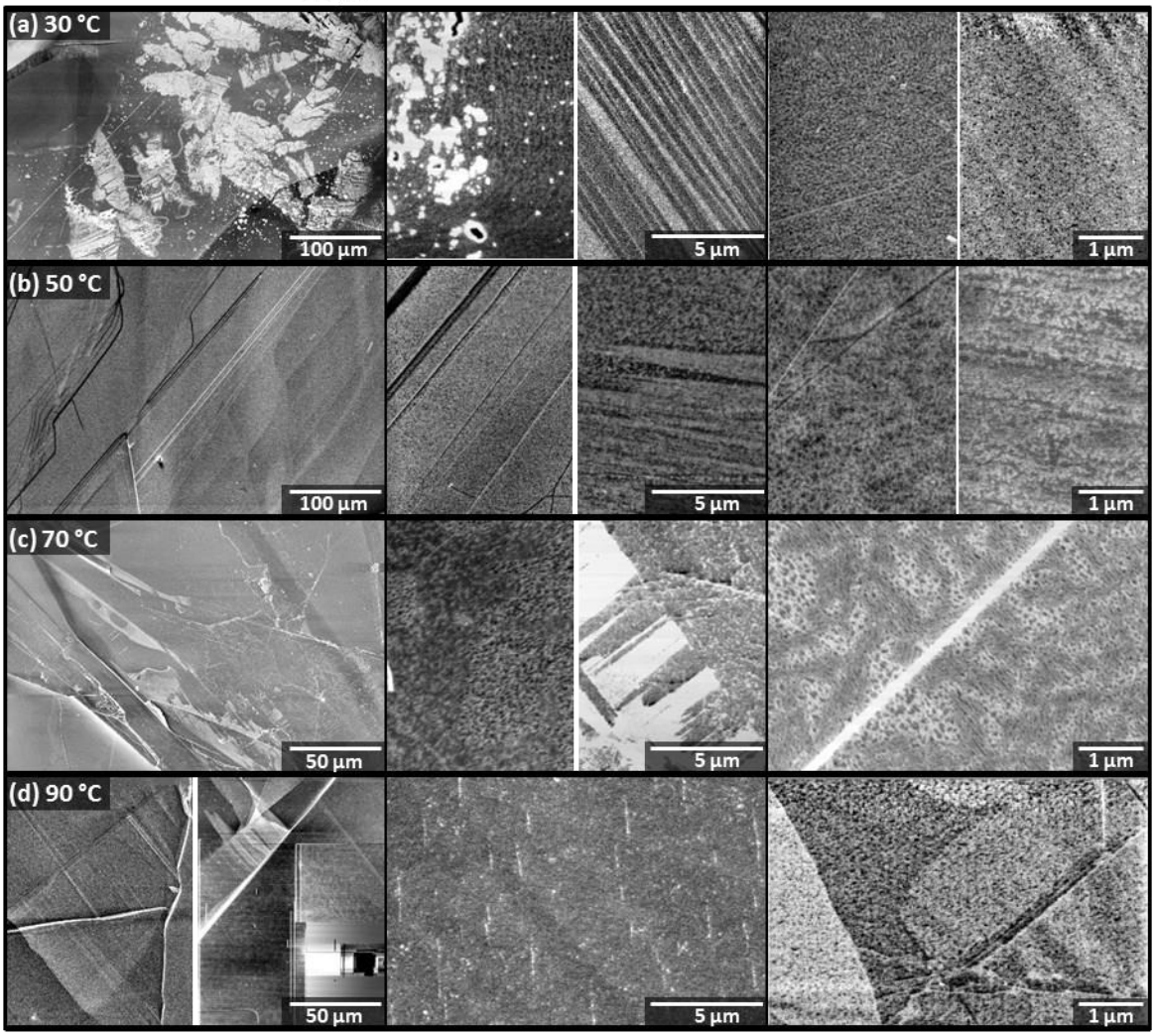

Figure S.C. 12. Representative SEM images of PCDA transferred to MoS_2 from Langmuir films with a packing density of 20 $Å^2$/chain and a subphase temperature of 30 °C. Substrate was held at a dipper setpoint temperature of (a) 30 °C, (b) 50 °C, (c) 70 °C, or (d) 90 °C. Each row comprises images at three different scales for the substrate temperature stated in the left panel.

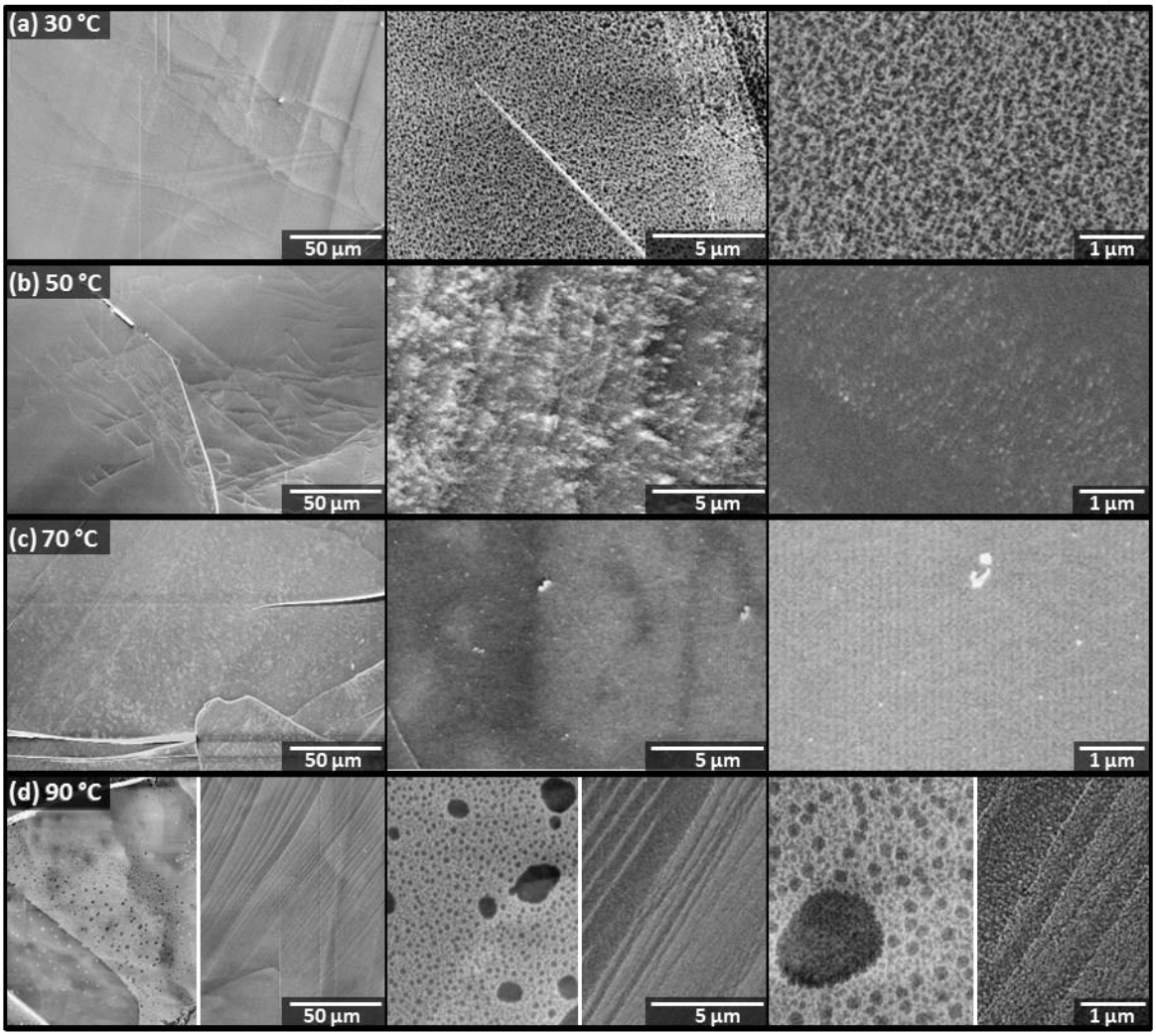

Figure S.C. 13. Representative SEM images of PCDA transferred to MoS_2 from Langmuir films with a packing density of 35 $Å^2$/chain and a subphase temperature of 30 °C. Substrate was held at a dipper setpoint temperature of (a) 30 °C, (b) 50 °C, (c) 70 °C, or (d) 90 °C. Each row comprises images at three different scales for the substrate temperature stated in the left panel.

Representative SEM images for solution deposition of PCDA and diyne PE on HOPG and MoS_2

Deposition of amphiphiles from solutions in organic solvent is an experimentally expedient method for noncovalent functionalization. Here, we compare SEM images acquired from HOPG and MoS_2 substrates functionalized with either PCDA or diyne PE deposited from solution. Molecules were deposited on both substrates from dilute solutions (0.0025 mg/mL in 3:2 (v:v) hexane:isopropanol), onto substrates heated to 90 °C, conditions which we have used previously to achieve µm-scale domains of both amphiphiles on HOPG. Figure S.C.14 shows representative

images of MoS_2 functionalized with PCDA, with scale bars ranging from 100 μm to 2 μm. At micrometer scales, significant aggregates are observed on the surface. When diyne PE is deposited on MoS_2, large areas of both ordered lamellar phases (Figure S.C.15) and standing phases (Figure S.C.16) are typically observed, with relatively low surface coverage in the areas of lamellar assembly (linear features in Figure S.C.15b–d). Figure S.C.17 shows representative images of HOPG and MoS_2 functionalized with PCDA (Figure S.C.17a,b) or diyne PE (Figure S.C.17c,d). When deposited from 0.15 mg/mL in 3:2 (v/v) hexane/isopropanol, surface coverage is overall higher, but significant areas of standing phase are present.

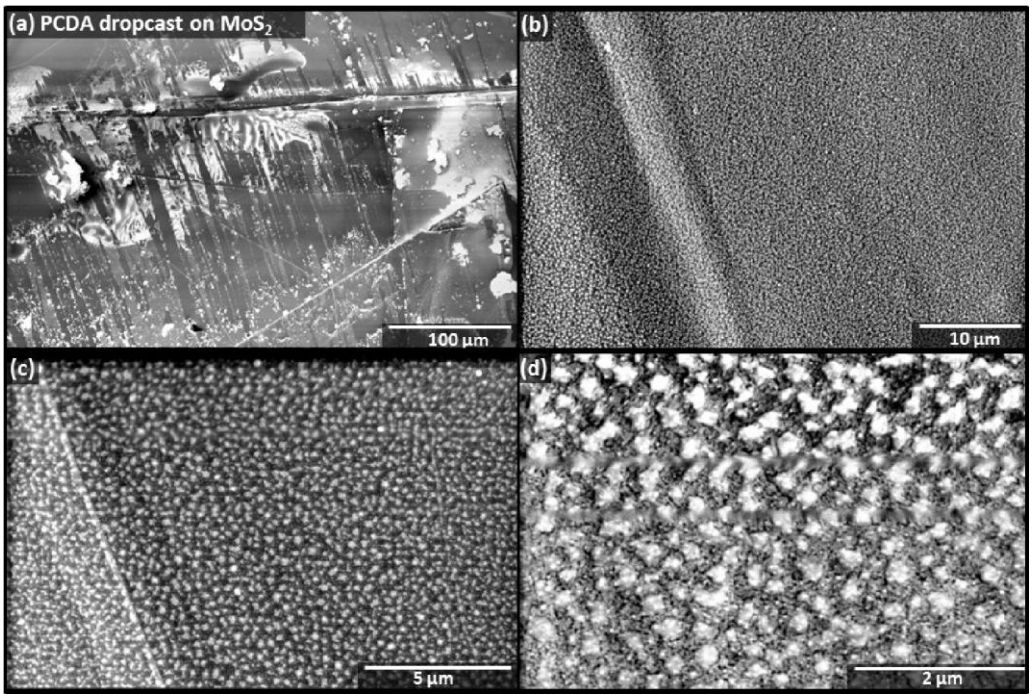

Figure S.C. 14. SEM images of PCDA deposited on MoS_2 from 0.0025 mg/mL PCDA in 3:2 (v/v) hexane/isopropanol.

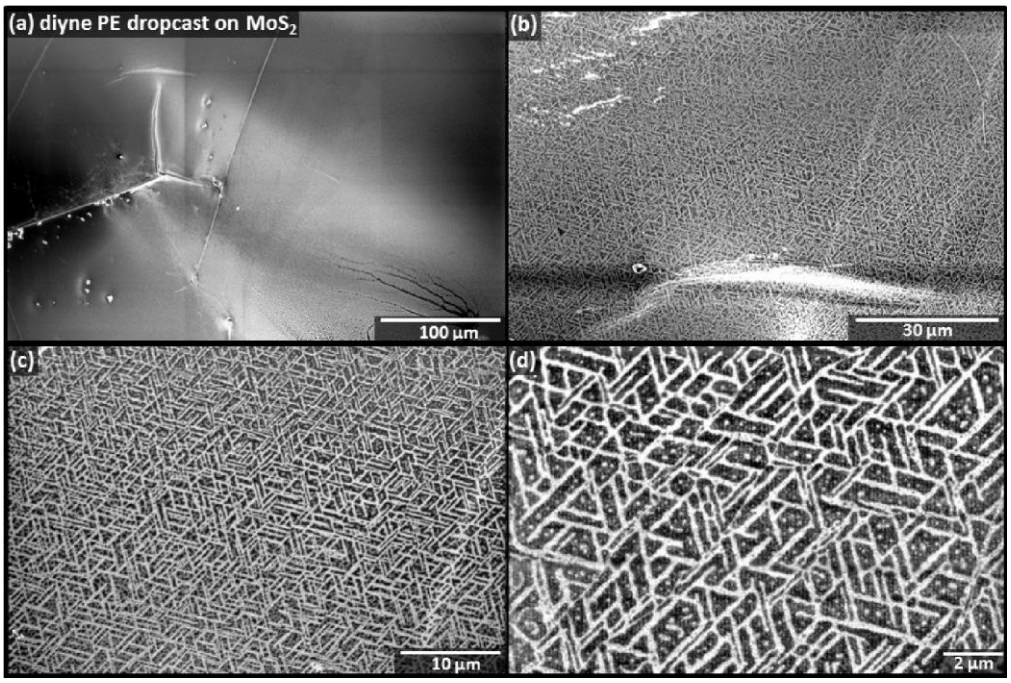

Figure S.C. 15. SEM images of diyne PE deposited on MoS_2 from 0.0025 mg/mL diyne PE in 3:2 (v/v) hexane/isopropanol.

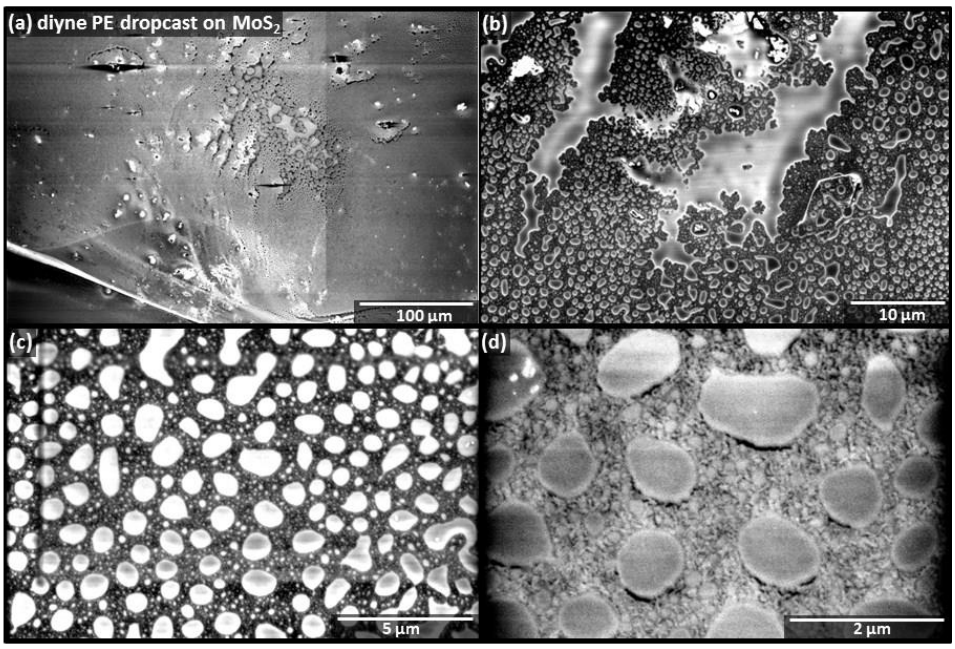

Figure S.C. 16. Representative SEM images of diyne PE deposited on MoS_2 from 0.0025 g/mL diyne PE in 3:2 (v/v) hexane/isopropanol. Substrates typically exhibit areas of both lying down phases (similar to Figure S.C.12), and standing phases (shown here).

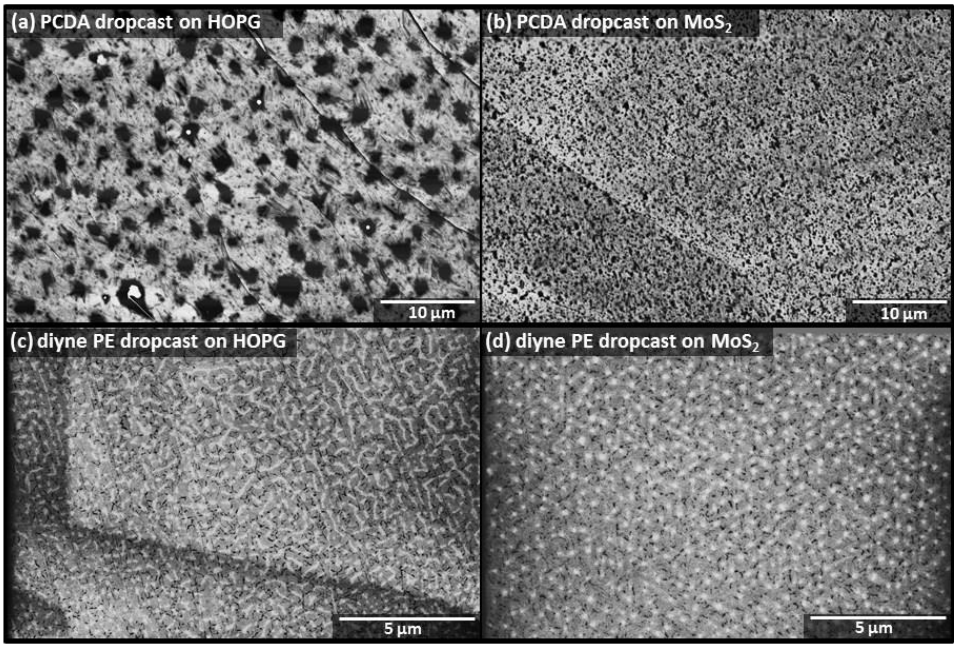

Figure S.C. 17. Representative SEM images of (a,b) PCDA and (c,d) diyne PE deposited on MoS_2 from 0.15 mg/mL solution in 3:2 (v/v) hexane:isopropanol. Areas that appear dark in (a) and (b) are large aggregates of PCDA that do not produce strong scattering.

Additionally, we compared results obtained for slowly removing substrates from a dilute solution of each molecule (dip-coating). Figure S.C.18 compares results of the three film preparation procedures for the two molecules and substrate types tested. While dip-coating produces the most even surface coverage, thermally controlled LS transfer produces large, highly ordered molecular domains while maintaining reasonable uniformity of surface coverage.

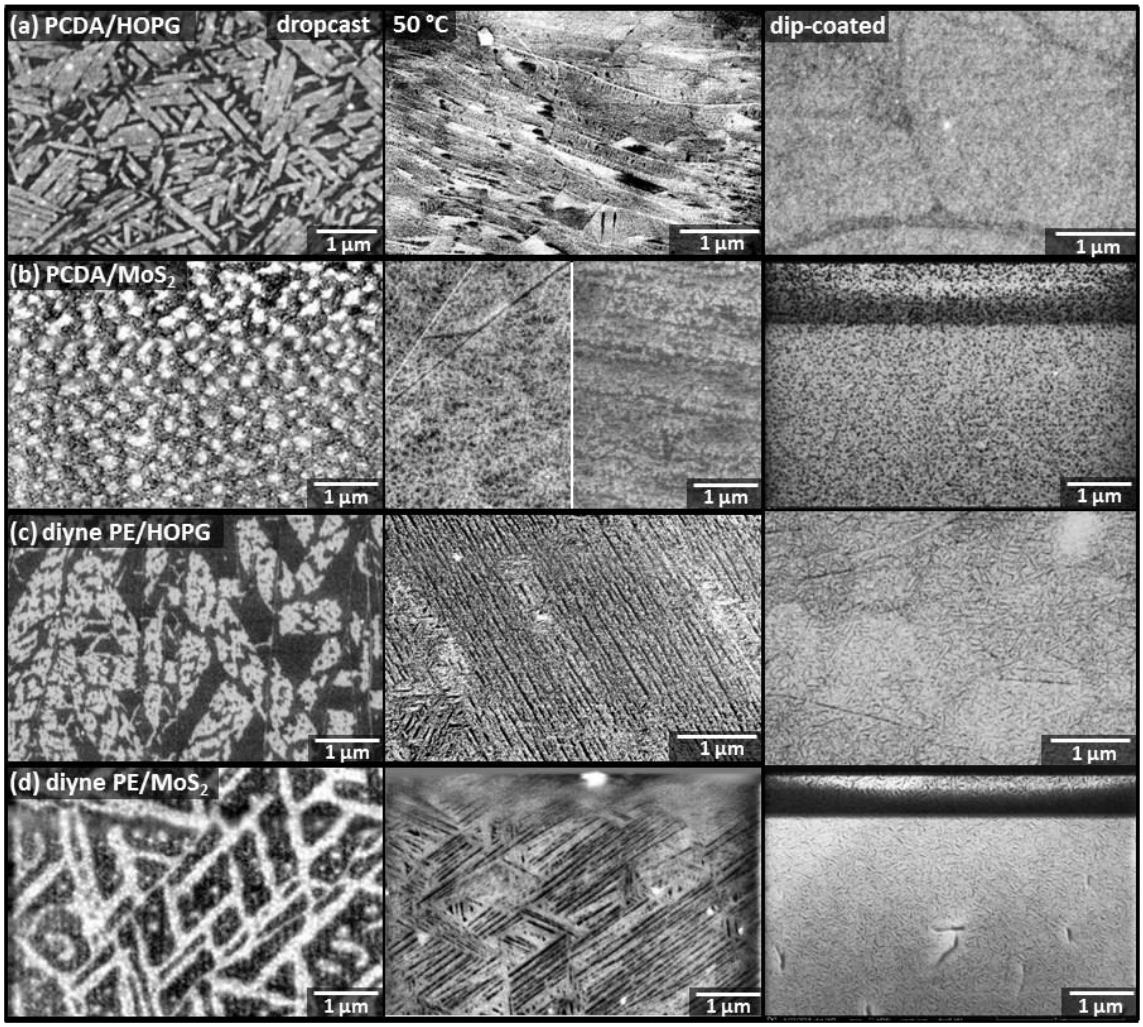

Figure S.C. 18. Representative SEM images of (a) PCDA assembled on HOPG, (b) PCDA assembled on MoS_2, (c) diyne PE assembled on HOPG, and (d) diyne PE assembled on MoS_2, via the stated surface preparation method: (left) dropcasting, (center) thermally controlled LS transfer with a dipper set point temperature of 50 °C, or (right) dip-coating.